New Synthetic Routes, Topologies and Physical Properties of Single-Chain Nanoparticles

Author: Jon Rubio Cervilla

Supervisor: Prof. José A. Pomposo

Donostia - San Sebastián, 2018

Materials Physics Center
Centro de Física de Materiales

eman ta zabal zazu
Universidad del País Vasco
Euskal Herriko Unibertsitatea

Contents

CHAPTER 1

Introduction

1.1. Nanoscience and Soft Matter

Nanoscience is the study of matter at dimensions of a few nanometres [1]. The root "nano" comes from the Greek for "dwarf" and it accounts for 10^{-9}. At this level, the properties of materials differ in fundamental ways from the properties in the bulk state [2]. The remarkable expansion of nanoscience during the last decades has sped up the exploration of these novel properties, giving rise to revolutionary disciplines such as nanomedicine [3], nanoelectronics [4] or nanocatalysis [5]. Therefore, it is not surprising to see the enormous increase in the number of nanoscience-related publications as well as in the funding for new projects over the last years [6].

Currently, research on nanoscience leans on two different approaches: top-down and bottom-up [7]. Top-down approaches seek to create smaller devices by removing parts of a larger one, while bottom-up approaches capitalize on the ability of small materials to self-assemble and form complex systems.

Soft matter is a subfield of condensed matter comprising a variety of systems that are *easily* deformable. In other words, the predominant physical behaviours occur at an energy scale comparable to room temperature thermal energy (≈ 25 meV) [8]. Under this classification, we can find a large array of systems including polymer melts or solutions, micellar solutions, colloids, foams, gels, liquid crystals and a number of biomolecules. Hence, soft matter nanotechnology is a multidisciplinary area of chemistry, physics, biology, medicine and materials science.

1.2. Single-chain nanoparticles

In the light of the rapid expansion of nanoscience, a new discipline has emerged in the field of soft matter science: the single-chain technology, a novel discipline that seeks for the construction of individual soft nano-objects by working at the single polymer chain level [9]. By taking inspiration from the relationship between topology, precise morphology, and unique functionality of natural biomacromolecules, the expected long-term output of single-chain technology is the construction of a variety of ultra-small single-chain soft nano-objects endowed with useful, autonomous and smart functions.

In recent years, one of the most promising outputs of single-chain technology is SCNPs [10]. These nanoparticles are formed by an intrachain folding/collapse process of a single polymer chain (precursor) in a way reminiscent of the folding of proteins to their native, functional state (Figure 1.1).

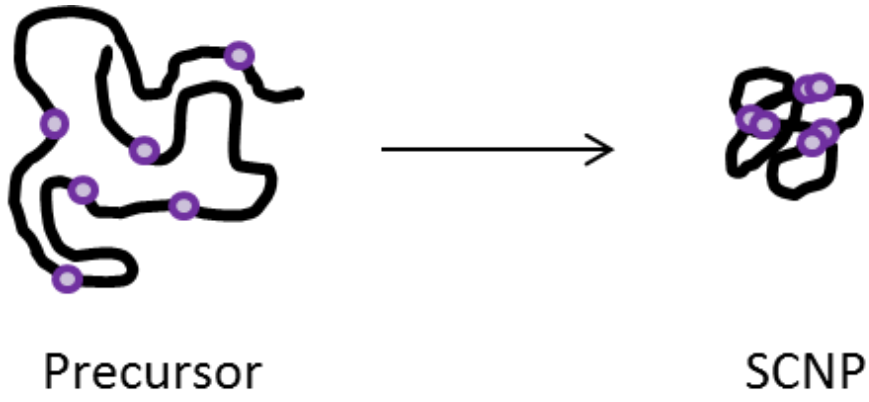

Figure 1.1. Schematic illustration of the folding of a polymeric precursor into a SCNP. Purples circles represent the cross-linking points present along the chain.

Three main techniques are involved in the synthesis of SCNPs: precursor synthesis, precursor functionalization and intrachain folding/collapse. These processes will now be discussed in detail hereunder.

1.2.1. Precursor synthesis

As SCNPs are basically an ensemble of folded macromolecules, it is of outmost importance to select an appropriate polymerization technique to produce well-defined single-chain polymeric precursors of controlled molar mass and narrow size distribution. Among the numerous polymerization techniques that have already been used to prepare SCNP precursors, some of the most important are reversible addition fragmentation chain transfer (RAFT) [11], nitroxide-mediated radical polymerization (NMP) [12], atom transfer radical polymerization (ATRP) [13] and ring-opening polymerization (ROP) [14].

Due to their higher relevance in the experiments carried out in this thesis, we will elaborate on RAFT and ROP mechanisms.

RAFT polymerization

RAFT polymerization is a reversible deactivation radical polymerization and one of the most versatile methods for providing living characteristics to radical polymerization. It makes use of a chain-transfer agent, typically a thiocarbonylthio compound, to keep molecular weight and polydispersity under control during a free-radical polymerization [15].

The mechanism of a RAFT polymerization involves six main steps (see Figure 1.2) the most important one being the main equilibrium, where the fast interchange between

dormant polymer chains and propagating radicals provides equal opportunities for all chains to grow, resulting in a very narrow size distribution.

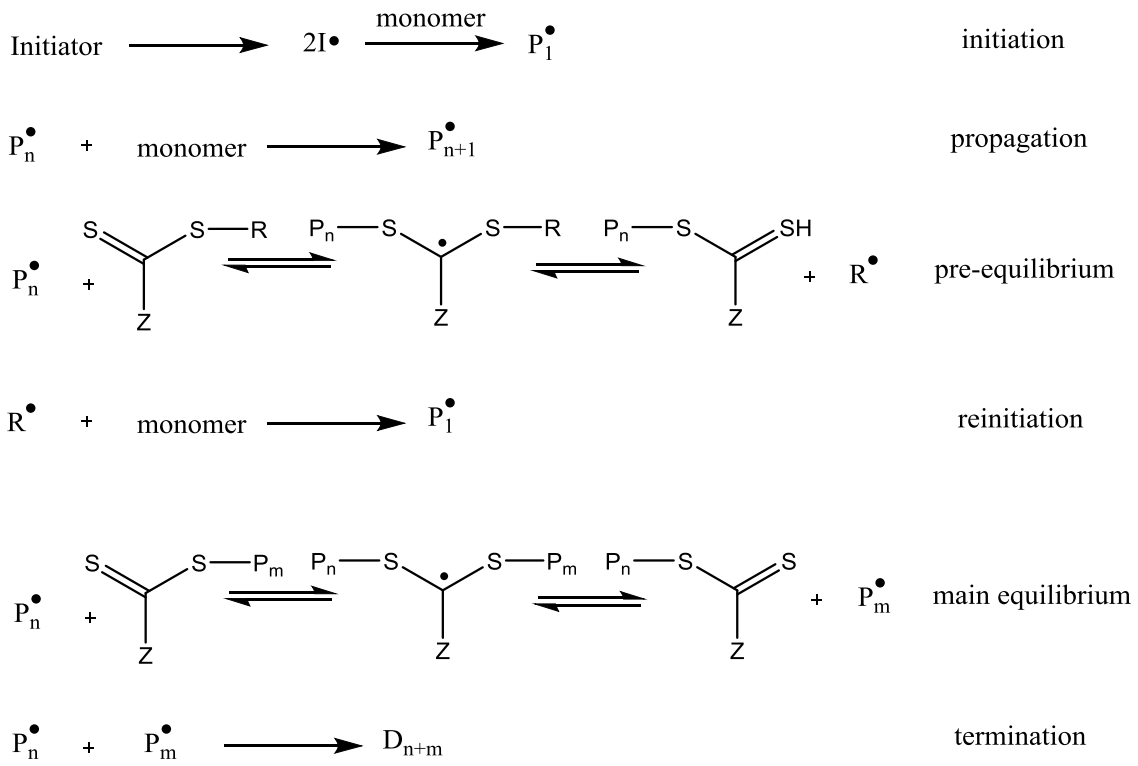

Figure 1.2. Mechanism of RAFT polymerization with a thiocarbonylthio compound as chain-transfer agent.

RAFT polymerization is a widely used technique in the synthesis of SCNP precursors [16] as it provides great control over the reaction, it is compatible with a broad range of monomers, it has a high functional group tolerance and no metals are involved during polymerization.

ROP polymerization

ROP polymerization is a form of chain-growth polymerization, in which cyclic monomers react with active chains by opening their ring system. It enables the

polymerization of a variety of structures, such as cyclic olefins [17], ethers [18], thioethers [19], lactones [20], thiolactones [21] or lactams [22].

Two equally important factors determine the reactivity of a cyclic monomer towards ROP: thermodynamics (the monomer-macromolecule equilibrium must be shifted to the polymer formation) and kinetics (monomer conversion must evolve within reasonable experimental times).

Depending on the nature of both the cyclic monomer and the propagating centre, ROP is commonly divided into different sub-mechanisms, the most important being cationic, anionic and radical ROP. In this thesis, nonetheless, we will focus on a different type of ROP: the zwitterionic ring-opening polymerization (ZROP). ZROP mechanisms require the presence of zwitterionic (i.e. neutral molecules with at least one positive and one negative charge) intermediates. ZROP of cyclic ethers with $B(C_6F_5)_3$ as catalyst (Figure 1.3) has been extensively studied by Barroso-Bujans et al. [23].

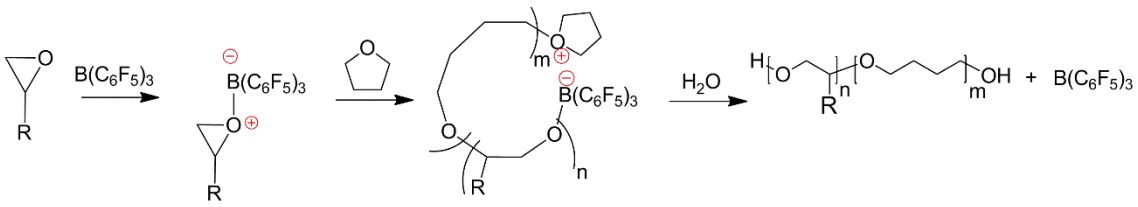

Figure 1.3. Simplified $B(C_6F_5)_3$-catalyzed ZROP mechanism of a generic glycidylic monomer with THF as proposed by Barroso-Bujans et al [23].

1.2.2. Precursor functionalization

Frequently, polymers synthesized with the techniques described above do not present functional groups suitable for the intrachain cross-linking reaction that leads to SCNPs. In this case, an intermediate step, known as polymer functionalization or post-polymerization reaction, is needed.

Azidation (nucleophilic substitution, Figure 1.4) [24], thiol-ene/thiol-yne additions [25], copper-catalyzed azide alkyne cycloaddition (CuAAC) [26], thiol-disulfide exchange [27], Diels-Alder reaction [28] and Michael-type addition [29] are amongst the most efficient and widely used functionalization reactions.

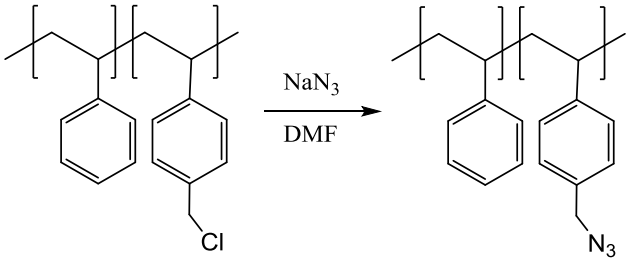

Figure 1.4. Scheme of the azidation reaction of poly(styrene-co-chloromethyl styrene) in DMF.

1.2.3. Intrachain folding/collapse

Folding single polymer chains by means of intramolecular cross-linking reactions constitutes the critical stage of SCNP synthesis, as it strongly influences the structure and properties of the final product. These reactions are normally performed at very low concentrations to avoid intermolecular side reactions that would lead to aggregation. The solvent plays an important role as well, as it determines the conformation of the chain during the folding process [30].

Based on the nature of the cross-linking, precursor folding reactions can be classified into three groups: covalent folding, non-covalent folding and external cross-linker assisted folding.

Covalent folding

Covalent folding of the precursor chain can be induced by reaction of identical groups (intrachain homocoupling) or different groups (intrachain heterocoupling). Copper

catalysed carbon-carbon click chemistry (Glaser-Hay coupling) [31], nitrene mediated cross-linking [32] or benzocyclobutene (BCB) dimerization [33] are examples of intrachain homocoupling. Concerning intrachain heterocoupling, copper catalysed azide-alkyne cycloaddition (CuAAC, Figure 1.5) is one the most widely used reactions in the field [34].

A particularly interesting feature of some dynamic covalent interactions is their reversibility, i.e. their ability to undo and restore the initial moieties. Reversible SCNPs can consequently adapt their structure and properties to external stimuli. For instance, Sánchez-Sánchez et al. reported that enamine formation provides a facile pathway towards pH-responsive SCNPs [35]. These stimuli-responsive structure adaptations make SCNPs good candidates for potential applications such as drug-delivery in nanomedicine[36].

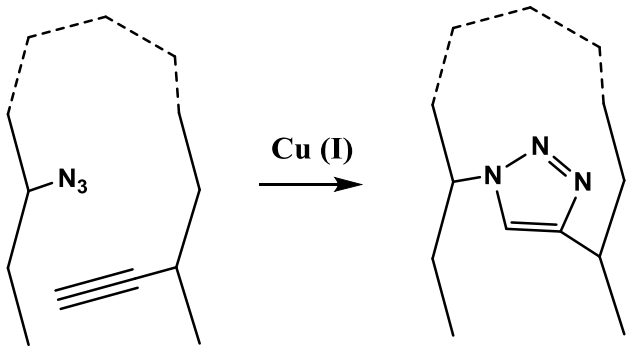

Figure 1.5. Scheme of an intramolecular CuAAC reaction.

Non-covalent folding

Non-covalent or supramolecular interactions have been extensively employed to construct not only SCNPs but also more complex architectures, such as multi-block

supramolecular polymers or multi-arm self-assembled stars [37]. Table 1.1 summarizes some examples of non-covalent interactions used in SCNP synthesis.

Table 1.1. Examples of supramolecular interactions suitable for precursor folding.

Interaction type	Example
Hydrogen bonding	Phenol – pyridine [38]
π-π stacking	Pyrene − diimide
Metal coordination	Terpyridine − Zn(II)
Host-guest interaction	Cyclodextrin − adamantane
Ionic interaction	Sulfonic acid − amine

External cross-linker assisted folding

External cross-linkers are relatively short multifunctional molecules capable of reacting with different groups of the precursor chain. This folding technique is compatible with most of the interactions described above, as it is possible to endow these molecules with the desired functional groups.

1.3. Cyclic polymers

Along with the remarkable development of single-chain technology in the last years, the ability to perform controlled chain compaction has enabled the construction of complex soft nano-objects beyond randomly folded SCNPs [9]. In this Section, main synthetic aspects of the simplest of all folding systems, cyclic polymers, are reviewed.

Preparation of high purity macrocycles is typically performed by two different approaches: the ring-expansion method and the ring-closure method (Figure 1.6) [39].

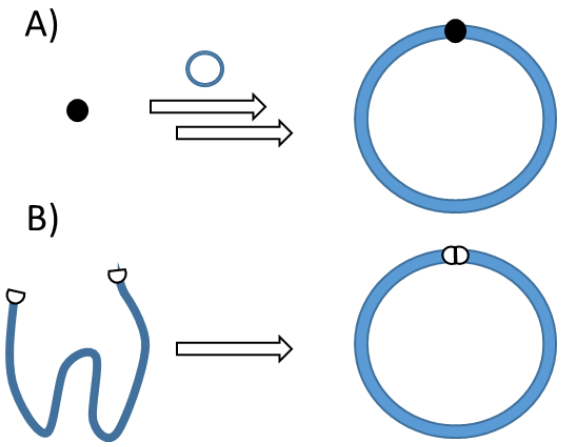

Figure 1.6. Schematic illustration of a ring-expansion polymerization (A) and a ring-closure reaction (B).

Ring-expansion polymerization involves a cyclic initiator that allows chain growth into a propagating macrocycle. Due to the fact that cyclic topology is maintained throughout the process, this technique allows for the synthesis of high molecular weight (> 1000 kg/mol) ring polymers at high concentrations in relatively short reaction times. Lack of control over polydispersity and molecular weight, along with the incompatibility with many functional groups are the major drawbacks for this technique.

On the other hand, ring-closure strategy involves ring formation upon reaction of the chain ends of a previously synthesized polymer. Thus, it is possible to start from a controlled polymerization, obtaining well-defined monodisperse chains, and endow them with a wide range of functional groups afterwards prior to cyclization.

Contrary to ring-expansion techniques, ring-closure is only suitable for low molecular weight polymers (short chains) as the reactive chain ends have to diffuse within a capture volume with a rate constant k_c compatible with experimental times. In addition, it is necessary to avoid intermolecular coupling reactions in order to obtain pure monocyclic samples. The ratio of monocyclic species to aggregated chains is given by

the probability of a chain end to find its complementary on the same chain (P_c) over that of another macromolecule (P_L). Jacobson and Stockmayer [40] introduced these relative probabilities, defined by Equations 1.1 and 1.2.

$$P_c = \left(\frac{3}{2\pi}\right)^{3/2} \frac{\nu_s}{\langle r^2 \rangle^{3/2}} \tag{1.1}$$

$$P_L = \frac{2N}{V}\nu_s = \frac{2N_A c}{m}\nu_s \tag{1.2}$$

Here, ν_s is the capture volume, $\langle r^2 \rangle$ is the mean-square distance between the two chain ends, N is the number of chains in the volume V, M is the molecular weight, N_A is Avogadro's number and c is the concentration of the polymer in mg/mL.

Intuitively, the probability of aggregation increases with the concentration, therefore, ring-closing reactions require high dilution conditions to be effective. Jacobson and Stockmayer [40] predicted that the cyclization probability decreases with the chain length as $n^{-3/2}$, where *n* accounts for the number of atoms in the polymer backbone.

1.4. Applications of SCNPs

SCNPs are prominent candidates to make major contributions to a wide range of fields, from nanomedicine to sensing, catalysis, and other diverse uses. Although this field is relatively new (irreversible SCNPs were synthesized in 2001 for the first time [41], whilst reversible ones were first disclosed as late as in 2008 [42]), the large amount of proof-of-concept experiments performed so far have demonstrated the huge possibilities of SCNPs.

Nanomedicine

Nanomedicine can be defined as the use and application of nanotechnology for diagnosis, monitoring of physical and pathologic processes, for therapy, and for control of biological systems [3]. Nanoparticles, when compared to typical small molecules, show a size large enough to be retained in the body based on a range of physiological changes and morphological and biochemical differences that occur in different tissues due to a variety of diseases and disorders. Typically, nanoparticle size is of outmost importance to consider when accessing a tumour tissue by means of the so-called enhanced permeability and retention (EPR) effect [43]. To date several cytotoxicity studies have been carried out to demonstrate the non-toxic character of a variety of SCNPs [44,45]. Even if more systematic studies are certainly required, these ones pave the way to the use of SCNPs as biocompatible drug delivery systems.

Several proof-of-concept experiments have been performed involving reversible SCNPs as controlled drug delivery nanocarriers of chiral amino acid derivatives, peptides, vitamins and small-molecule drugs [46]. Moreover, SCNPs have been evaluated as image contrast agents for magnetic resonance imaging (MRI) [47], gamma emitters for single photon emission computerized tomography (SPECT) [43], and fluorescent probes for confocal laser scanning microscopy (CLSM) [48]. The results from all these initial studies reveal the significant potential of SCNPs for the broad field of nanomedicine, in general, and for the specific areas of controlled drug delivery systems and image contrast agents, in particular.

Catalysis

SCNPs offer many possibilities for the development of catalytic systems [49], including enzyme-mimic nano-objects: a large surface-to-volume ratio that facilitates the

diffusion of reagents and products to catalytic sites; two limiting morphologies, sparse and globular, with multiple small "local pockets" or a single pocket of larger size, respectively; availability of precursors and solvent-based strategies for tuning nanoparticle size, pocket hydrophobicity, and their internal structure; and availability of reversible (responsive) and irreversible (permanent) SCNPs based on intramolecular dynamic interactions or covalent bonds, respectively.

Main proof-of-concept applications of SCNPs in catalysis include their use as nanoreactors for the synthesis of chemical compounds, polymers and nanomaterials [50].

Sensing

SCNPs also offer interesting possibilities for the development of sensors and biosensors, as revealed by proof-of-concept experiments related to sensing of metal ions [51] and sensing of proteins [52].

1.5. Polymer physics: size and scaling laws

Soft matter systems are complex, both in structure and dynamics. Theories for these materials are highly elaborated and in many cases not quantitative. However, it is helpful to consider how one variable depends on another, keeping other quantities constant. This leads to the so-called "scaling laws", where numerical constants are omitted, but the interrelationship of quantities is established.

As an example, we can consider the dimensions in a polymer chain. From a physicist's point of view, a polymer is a set of units, called monomers, connected linearly as a

chain. If we consider an isolated homopolymer formed by N + 1 monomers at positions $\{r_0, r_1, \ldots, r_N\}$, the end-to-end distance R is given by Equation 1.3:

$$R = r_N - r_0 \tag{1.3}$$

In the ideal case of a flexible polymer, for which the bond vectors are completely independent and can orient in any direction in space, the polymer can be described by a simple random walk in three dimensions (Figure 1.7) [53].

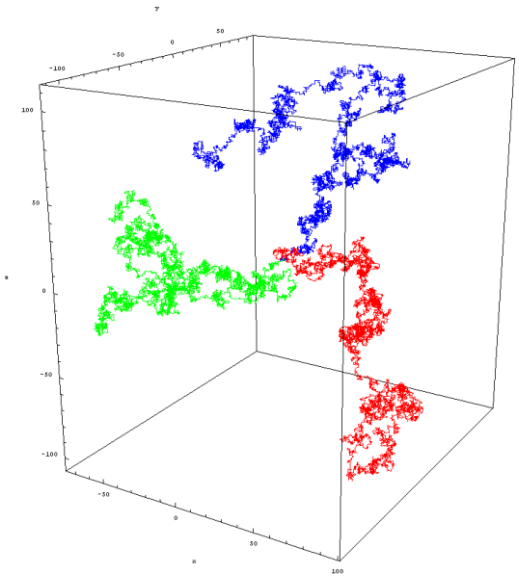

Figure 1.7. Illustration of three different random walks (green, red and blue) in three dimensions.

Here, the mean end-to-end distance is proportional to the number of steps (monomers) and translates in the following scaling-law:

$$\mathrm{R} \sim N^{\nu} \tag{1.4}$$

where ν = 1/2 is the Flory exponent. However, as real polymer cannot intersect themselves (two monomers cannot be in the same place at the same time), we need a more realistic model that takes into account excluded volume considerations: a "self -

avoiding" walk. In this case, the scaling exponent is slightly higher, ν = 3/5. This applies to a macromolecule in solution with a "good solvent".

Although the end–to–end distance provides an estimate of the dimensions of the chain, polymer sizes are typically reported by experimentally accessible magnitudes, such as the radius of gyration (r_g) or the hydrodynamic radius (r_H). The radius of gyration (see Equation 1.5) is defined as the mean squared distance of each point on the object from its centre of gravity.

$$r_g = R\sqrt{\frac{1}{6}} \tag{1.6}$$

On the other hand, the hydrodynamic radius r_H is defined as the size of a hard sphere diffusing at the same rate as the molecule that is being observed.

1.6. Polymer dynamics

Because of their macromolecular character, the structural and dynamic processes of polymers strongly depend on the length and time scales under observation (Figure 1.8) [54].

At lengths comparable to the radius of gyration, the chain character of the macromolecule prevails over the role of pendant side groups present in the polymer backbone. The characteristic dynamical processes present at this level (chain diffusion, Rouse dynamics and reptation) depend on the chain length and can be very long.

At intermolecular length scales (≈ 10 Å), the main dynamical process is the so-called α-relaxation, which characteristic time increases dramatically as the temperature approaches the glass transition temperature T_g.

At small (molecular) length scales (≈ 1 Å), the motions are usally localized and activated. Among these dynamical processes, one can find vibrations, such as the Boson peak [55], and secondary relaxations like the β-relaxation.

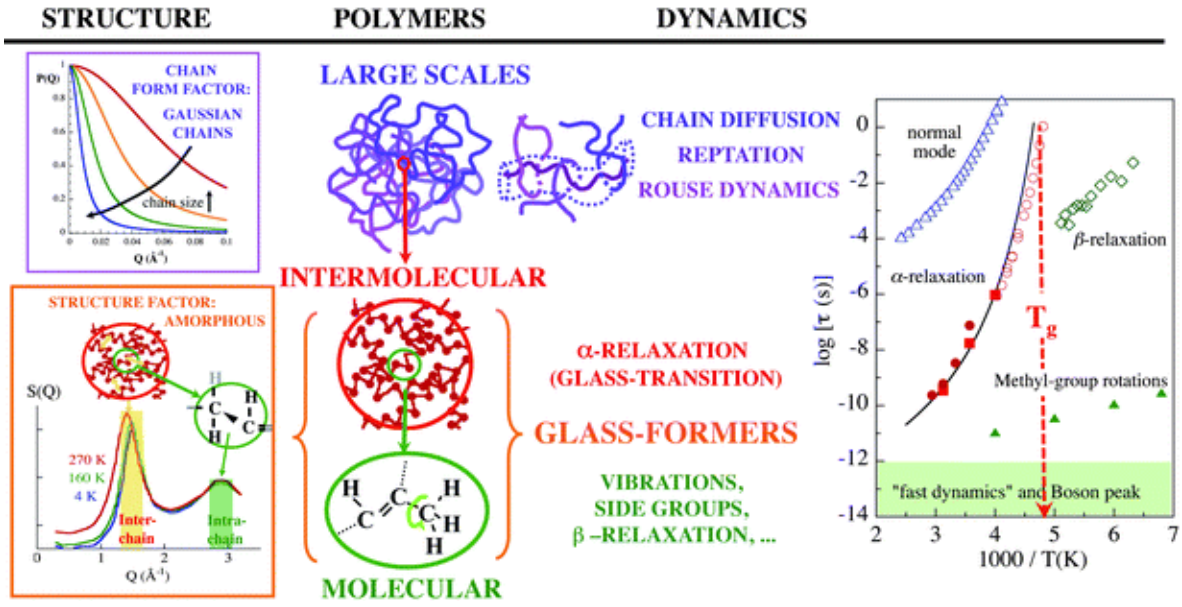

Figure 1.8. Relevant features of polymers as a function of the length scale under observation. On the right, the relaxation map of polyisoprene showing the temperature dependence of the relaxation time for the main dynamical processes. Reproduced from Ref. 54.

1.6.1. The Rouse model

The Rouse model [56] is frequently used in polymer physics to describe the dynamics of short chain polymers. In this model, the chain is subdivided into segments that are sufficiently large to display rubber like elasticity (spring-like behaviour). The most important assumption is that there is no interaction between segments (neither of the

same chain nor of different chains) except for a global friction force and a random force as assumed in the derivation of Brownian motion of a single particle.

The results obtained for the macroscopic rheological properties, terminal viscosity η and self-diffusion constant D are

$$\eta = \frac{\xi l^2 \rho N}{36} \tag{1.7}$$

$$D = \frac{k_B T}{\xi N} \tag{1.8}$$

which are in good agreement with what is found for low molecular weight polymers (N is the number of segments, ρ the number density of the polymer segments, ξ the friction coefficient and l the average length of a segment). These results rely on the rough argument that if the only interaction is a friction with the environment, its effect on the macromolecule will increase proportionally to the number of repeat units.

Microscopically, this method predicts a proportionality of the mean-square distance of a typical segment to $t^{1/2}$, instead of t for single diffusion, which is a consequence of the connectivity of the chain.

In larger chains, the predictions of the Rouse model start to fail after a crossover "entanglement time", and other models, such as the reptation model, need to be considered.

1.6.2. Polymer reptation

The most relevant model describing the macroscopic properties for polymers beyond the entanglement onset is the tube model of Edwards [57] developed by de Gennes [58]. Here, the motion of a polymer chain is hindered by a virtual tube formed by the

surrounding macromolecules (Figure 1.9). As a consequence, the chain performs a snake-like motion (reptation) along the tube.

This virtual tube restricts the motion of the macromolecule on an intermediate length scale ($d \approx 5$ nm). At shorter times, the restriction is not effective and the motion shows a Rouse-like behaviour with $D \propto N^{-1}$. The onset of the tube interaction defines a new intermediate time scale, the entanglement time, τ_e.

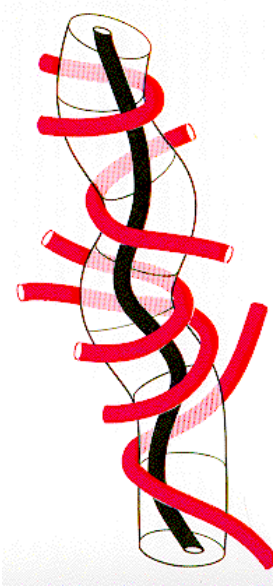

Figure 1.9. Representation of the virtual tube created by the surrounding macromolecules (in red).

In this model, the viscosity η of a polymer melt is determined by the time needed by the chain to leave the initial tube and constitute a new one. The value of η is predicted to be proportional to the cube of the number of segments $\eta \propto N^3$, which is a reasonable approximation to the actual $\eta \propto N^{3.4}$ observed relationship. The self-diffusion constant of the chain follows $D \propto N^{-2}$.

1.6.3. Polymer relaxations and the glass transition

As a polymer is cooled to lower temperatures, its viscosity increases and the chains move more and more slowly. At a certain temperature, the dynamics will be so slow that the macromolecules will not have time to rearrange significantly before the temperature is lowered further. The time scales at this point become prohibitively long compared to the experimental ones. This is what is known as a glass, a material which structure is frozen for practical purposes [59].

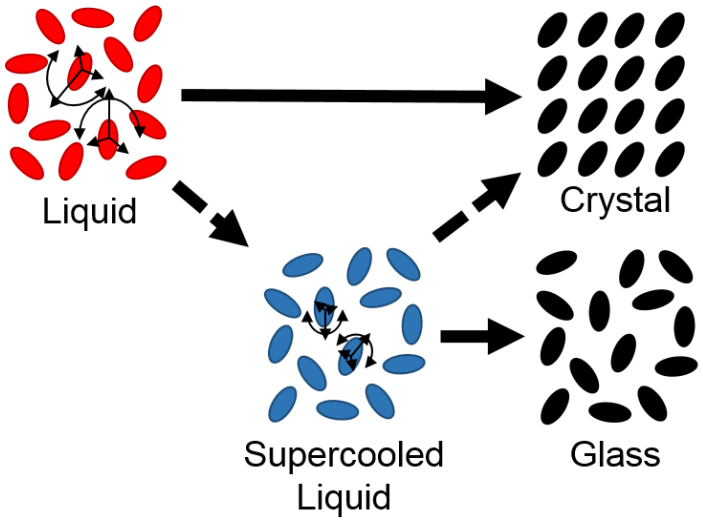

Figure 1.10. Scheme of the molecular motions and structure of liquids, crystals, supercooled liquids and glasses.

The temperature at which this process takes place is called the glass transition temperature T_g. It is worth mentioning that, as the glass-transition does not occur suddenly, but rather over a range of temperatures, T_g does not have a single fixed value, and it will be different for different cooling rates. T_g is a very important material property, as it has a pronounced impact on the mechanical properties of the polymer.

The main structural relaxation is the so called α-relaxation, and it is associated with the glass transition [60]. As a consequence, T_g and segmental relaxation (the α-process)

have the same dependence on M_w and crosslinking. It is generally accepted that the α-process is related to conformational changes.

A simple relaxation process usually has a single exponential relaxation. The α-relaxation, however, is not a single exponential decay, and it is usually described by a stretched exponential relaxation, the so-called Kolrausch-William-Watts (KWW) equation:

$$G(t) \propto \exp[-(t/\tau)^{\beta}] \tag{1.9}$$

The smaller the value of β, the less exponential the response function.

The temperature dependence of the α-relaxation time is usually described by the Vogel-Tamman-Fulcher (VTF) equation (see Figure 1.8):

$$\tau = \tau_0 \exp\left(\frac{B}{T-T_\infty}\right) \tag{1.10}$$

When $T = T_\infty$ an Arrhenius-like equation is obtained.

Secondary processes occur at shorter time scales, usually attributed to local conformational rearrangements and they are commonly referred to as β-processes or γ-processes.

1.7. Outline and objectives of this Thesis.

This thesis presents conscientious work on polymeric single-chain nanoparticles (SCNPs). The combination of state-of-the-art polymer synthesis and advanced characterization techniques will allow us to:

1. Establish new synthetic routes towards SCNPs.
2. Synthesize SCNPs with novel topologies.
3. Carry out a thorough study of the physical properties of SCNP melts.

Chapters 1 and 2 introduce this emerging field and review the fundamental concepts, current synthetic methods, potential applications and some of the typical experimental techniques. Details concerning instrument types and setups used for this work are summarized in Chapter 2.

Chapter 3 presents an unprecedented merging of zwitterionic ring-opening polymerization and photoactivated thiol-yne coupling, resulting in an interesting new pathway towards SCNPs. Advanced techniques including, among others, *in situ* ^{13}C nuclear magnetic resonance (NMR) measurements or Mark-Houwink-Sakurada plots are employed to gain insight into the polymerization and SCNP formation processes.

In Chapter 4, a new SCNP topology is targeted: the single-ring nanoparticle (SRNP). It is finally achieved by a combination of controlled radical polymerization, photoactivated hetero Diels-Alder reactions and copper-catalyzed click chemistry. The resulting SCNPs are thoroughly characterized by size exclusion chromatography, nuclear magnetic resonance, infrared spectroscopy and UV-Vis spectroscopy.

Chapter 5 comprises a quantitative study of the size reduction upon reversible SCNP formation. Following a Flory-like argument, we propose an expression that provides a *priori* estimation of the size reduction upon folding single-chains. We perform a comparison of the predicted size reduction with extensive literature data (72 SCNPs, 22 reversible interactions).

To conclude, Chapter 6 presents a novel method to synthesize totally deuterated SCNPs starting from commercially available monomers and initiators. An exhaustive study of

the structural and dynamical properties of melts of these SCNPs is also performed, combining a variety of techniques, including elastic and quasi-elastic neutron scattering, dielectric and mechanical spectroscopy and calorimetries.

1.8. References

[1] Toumey, C. Reading Feynman into nanotechnology: a text for a new science. *Techné*, **2008**, *12*, 133−167.

[2] Whitesides, G. M. Nanoscience, nanotechnology and chemistry. *Small*, **2004**, *1*, 172−179.

[3] Mishra, A.K. Nanomedicine for drug delivery and therapeutics. *John Wiley & Sons*, **2013**.

[4] Puers, R.; Baldi, L.; Van de Voorde, M.; Van Nooten, S. Nanoelectronics. *John Wiley & Sons*, **2017**.

[5] Bahadur−Singh, S.; Kumar−Tandon, P. Catalysis: a brief review on nano−catalyst. *Journal of Energy and Chemical Engineering*. **2014**, *2*, 106−115.

[6] Velmurugan, C.; Radhakrishnan, N. Visualizing global nanotechnology research on publication deeds, 1989−2014. *Library Philosophy and Practice (e−journal)*, **2016**, 1372.

[7] Chen, Y.; Pépin, A. Nanofabrication: conventional and nonconventional methods. *Electrophoresis*, **2001**, *22*, 187−207.

[8] Hamley, I. W. Introduction to soft matter: synthetic and biological self−assembling materials. *John Wiley & Sons*, **2007**.

[9] Gonzalez−Burgos, M.; Latorre−Sanchez, A.; Pomposo, J. A. Advances in single − chain technology. *Chemical Society Reviews*, **2015**, *44*, 6122−6142.

[10] Pomposo, J. A. Single−chain polymer nanoparticles: synthesis, characterization, simulations and applications. *John Wiley & Sons*, **2017**.

[11] Barner–Kowollik, C. Handbook of RAFT polymerization. *John Wiley & Sons*, **2008**.

[12] Hawker, C. J.; Bosman, A. W.; Harth, E. New polymer synthesis by nitroxide mediated living radical polymerizations. *Chemical Reviews*, **2001**, *101*, 3661–3688.

[13] Wang, J. S.; Matyjaszewski, K. Controlled / living radical polymerization: Atom transfer radical polymerization in the presence of transition−metal complexes. *Journal of the American Chemical Society*, **1995**, *117*, 5614–5615.

[14] Nuyken, O.; Pask, S. D. Ring–opening polymerization: an introductory review. *Polymers*, **2013**, *5*, 361−403.

[15] Perrier, S. 50th anniversary perspective: RAFT polymerization: a user guide. *Macromolecules*, **2017**, 50, 7433−7447.

[16] Mansfeld, U.; Pietsch, C.; Hoogenboom, R.; Remzi–Bezer, C.; Schubert, U. Clickable initiators, monomers and polymers in controlled radical polymerizations–a propective combination in polymer science. *Polymer Chemistry*, **2010**, *1*, 1560–1598.

[17] Andrews, J.M.; Jones, F.R.; Semlyen, J.A. Equilibrium ring concentration and the statistical conformations of polymeric chains. *Polymer*, **1974**, *15*, 420–424.

[18] Endo, T.; Kanda, N. Syntheses of 2−phenyl−3−vinyloxirane derivatives that undergo radical ring−opening polymerization. *The Journal of Polymer Science, Part A: Polymer Chemistry*, **1985**, *23*, 1931–1938.

[19] Wang, Y−F.; Chan, K−P.; Hay, A−S. Free–radical ring–opening polymerization of macrocyclic aryl ether thioether ketone oligomers. *Macromolecules*, **1996**, *29*, 3717–3726.

[20] Suzuki, A.; Sudo, A.; Endo, T. Cationic ROP of 3−isochromanone through the formation of benzyl cationic intermediate and its friedel−crafts reaction. *The Journal of Polymer Science, Part A: Polymer Chemistry*, **2009**, *47*, 2214–2218.

[21] Overberger, C−G.; Weise, K−J. Anionic ring−opening polymerization of thiolactones. *Journal of the American Chemical Society*, **1968**, *90*, 3533−3537.

[22] Hashimoto, K. Ring−opening polymerization of lactams. Living anionic polymerization and its applications. *Progress in Polymer Science*, **2000**, *25*, 1411−1462.

[23] Asenjo−Sanz, I.; Veloso, A.; Miranda, J. I.; Alegría, A.; Pomposo, J. A.; Barroso−Bujans, F. Zwitterionic ring−opening copolymerization of tetrahydrofuran and glycidyl plenyl ether with $B(C_6F_5)_3$. *Macromolecules*, **2015**, *48*, 1664−1672.

[24] Gonzalez−Burgos, M.; Alegria, A.; Arbe, A.; Colmenero, J.; Pomposo, J. A. An unexpected way to aldehyde−decorated single−chain nanoparticles from azides. *Polymer Chemistry*, **2016**, *43*, 6570−6574.

[25] Perez−Baena, I.; Asenjo−Sanz, I.; Arbe, A.; Moreno, A. J.; Lo Verso, F.; Colmenero, J.; Pomposo, J. A. Efficient route to compact single−chain nanoparticles: photoactivated synthesis via thiol−yne coupling reaction. *Macromolecules*, **2014**, *47*, 8270−8280.

[26] Oria, L.; Aguado, R.; Pomposo, J. A.; Colmenero, J. A versatile "click" chemistry precursor of functional polystyrene nanoparticles. *Advanced Materials*, **2010**, *22*, 3038−3041.

[27] Ryu, J−H.; Chacko, R. T.; Jiwpanich, S.; Bickerton, S.; Babu, R. P.; Thayumanavan, S. Self−cross−linked polymer nanogels: a versatile nanoscopic drug delivery platform. *Journal of the American Chemical Society*, **2010**, *132*, 17227−17235.

[28] Croce, T. A.; Hamilton, S. K.; Chen, M. L.; Muchalski, H.; Harth, E. Alternative o−quinodimethane cross−linking precursors for intramolecular chain collapse nanoparticles. *Macromolecules*, **2007**, *40*, 6028−6031.

[29] Njiang, G.; Liu, G.; Hong, L. Chiral imprinting of diblock copolymer single−chain particles. *Langmuir*, **2012**, *27*, 7176−7184.

[30] Pomposo, J. A.; Perez−Baena, I.; Lo Verso, F.; Moreno, A. J.; Arbe, A.; Colmenero, J. How far are single−chain nanoparticles in solution from the globular state? *ACS Macro Letters*, **2014**, *3*, 767−772.

[31] Sanchez−Sanchez, A.; Asenjo−Sanz, I.; Buruaga, L.; Pomposo, J. A. Naked and self−clickable propargylic−decorated single−chain nanoparticle precursors via redox initiated RAFT polymerization. *Macromolecular Rapid Communications*, **2012**, *15*, 1262−1267.

[32] Jiang, X.; Pu, H.; Wang, P. Polymer nanoparticles via intramolecular crosslinking of sulfonyl azide functionalized polymers. *Polymer*, **2011**, *44*, 7242−7252.

[33] Dobish, J. N.; Hamilton, S. K.; Harth, E. Synthesis of low−temperature benzocyclobutene cross−linker and utilization. *Polymer Chemistry*, **2012**, *3*, 857−860.

[34] Liang, L.; Astruc, D. The copper (I)−catalyzed alkyne−azide cycloaddition (CuAAC) "click" reaction and its applications. An overview. *Coordination Chemistry Reviews*, **2011**, *255*, 2933−2945.

[35] Sanchez−Sanchez, A.; Fulton, D. A.; Pomposo, J. A. pH−responsive single−chain polymer nanoparticles utilizing dynamic covalent enamine bonds. *Chemical Communications*, **2014**, *50*, 1871−1874.

[36] Sanchez−Sanchez, A.; Akbari, S.; Moreno, A. J.; Lo Verso, F.; Arbe, A.; Colmenero, J.; Pomposo, J. A. Design and preparation of single−chain nanocarriers mimicking disordered proteins for combined delivery of dermal bioactive cargos. *Macromolecular Rapid Communications*, **2013**, *34*, 1681−1686.

[37] Sanchez−Sanchez, A.; Pomposo, J. A. Single−chain polymer nanoparticles via non−covalent and dynamic covalent bonds. *Particle & Particle Systems Characterization*, **2014**, *31*, 11−23.

[38] Ruiz de Luzuriaga, A.; Garcia, I.; Mecerreyes, D.; Etxeberria, A.; Pomposo, J. A. Design and stabilization of block copolymer micelles via phenol−pyridine hydrogen−bonding interactions. *Polymer*, **2010**, *51*, 1355.

[39] Josse, T.; De Winter, J.; Gerbaux, P.; Coulembier, O. Cyclic polymers by ring−closure strategies. *Angewandte Chemie International Edition*, **2016**, *55*, 13994−13958.

[40] Jacobson, H.; Stockmayer, W.H. Intramolecular reaction in polycondensations. I. The theory of linear systems. *The Journal of Chemical Physics*, **1950**, *18*, 1600.

[41] Mecerreyes, D.; Lee, V.; Hawker, C. J.; Hedrick, J. L.; Wursch, A.; Volksen, W.; Magbitang, T.; Huang, E.; Miller, R. D. A novel approach to functionalized nanoparticles: self−crosslinking of macromolecules in ultradilute solution. *Advanced Materials*, **2001**, *13*, 204−208.

[42] Seo, M.; Beck, B. J.; Paulusse, J. M. J.; Hawker, C. J.; Kim, S. Y. Polymeric nanoparticles via noncovalent cross−linking of linear chains. *Macromolecules*, **2008**, *41*, 6431−6418.

[43] Peer, D.; Karp, J. M.; Hong, S.; Farokhzad, O. C.; Margalit, R.; Langer, R. Nanocarriers as an emerging platform for cancer therapy. *Nature Nanotechnology*, **2007**, *2*, 751−760.

[44] Wong, E, H, H.; Lam, S. J.; Nam, E.; Qiao, G. G. Biocompatible single−chain polymeric nanoparticles via organo−catalyzed ring−opening polymerization. *ACS Macro Letters*, **2014**, 3, 524−528.

[45] Bai, Y.; Xing, H.; Vincil, G. A.; Lee, J.; Henderson, E. J.; Lu, Y.; Lemcoff, N. G.; Zimmerman, S. C. Practical synthesis of water−soluble organic nanoparticles with a single reactive group and a functional carrier scaffold. *Chemical Science*, **2014**, *5*, 2862−2868.

[46] Sanchez−Sanchez, A.; Akbari, S.; Etxeberria, A.; Arbe, A.; Gasser, U.; Moreno, A. J.; Colmenero, J.; Pomposo, J. A. "Michael" nanocarriers mimicking transient−binding disordered proteins. *ACS Macro Letters*, **2013**, *2*, 491−495.

[47] Perez−Baena, I.; Loinaz, I.; Padro, D.; García, I.; Grande, H. J.; Odriozola, I. Single−chain polyacrylic nanoparticles with multiple Gd (III) centres as potential MRI contrast agents. *Journal of Materials Chemistry*, **2010**, *20*, 6916−6922.

[48] Adkins, C. T.; Muchalski, H.; Harth, E. Nanoparticles with individual site−isolated semiconducting polymers from intramolecular chain collapse processes. *Macromolecules*, **2009**, *42*, 5786−5792.

[49] Pomposo, J. A. Bioinspired single−chain polymer nanoparticles. *Polymer International*, **2014**, *63*, 589−592.

[50] Perez−Baena, I.; Barroso−Bujans, F.; Gasser, U.; Arbe, A.; Moreno, A. J.; Colmenero, J.; Pomposo, J. A. Endowing single−chain polymer nanoparticles with enzyme−mimetic activity. *ACS Macro Letters*, **2013**, *2*, 775−779.

[51] Gillisen, M. A. J.; Voets, I. K.; Meijer, E. W.; Palmans, A. R. A. Single chain polymeric nanoparticles as compartmentalised sensors for metal ions. *Polymer Chemistry*, **2012**, *3*, 3166−3174.

[52] Latorre−Sanchez, A.; Pomposo, J. A. A simple, fast and highly sensitive colorimetric detection of zein in aqueous ethanol via zein−pyridine−gold interactions. *Chemical Communications*, **2015**, *51*, 15736−15738.

[53] Bhattacharjee, S. M.; Giacometti, A.; Maritan, A. Flory theory for polymers. *Journal of Physics: Condensed Matter*, **2013**, *25*, 503101.

[54] Arbe, A.; Alvarez, F.; Colmenero, J. Neutron scattering and molecular dynamic simulations: synergetic tools to unravel structure and dynamics in polymers. *Soft Matter*, **2012**, *8*, 8257-8270.

[55] Frick, B.; Alba-Simionesco, C.; Andersen, K. H.; Willner, L. Influence of density and temperature on the microscopic structure and the segmental relaxation of

polybutadiene. *Physical review E, Statistical physics, plasmas, fluids, and related interdisciplinary topics,* **2003**, *67*, 011804.

[56] Rouse, P. E. A theory of the linear viscoelastic properties of dilute solutions of coiling polymers. *The Journal of Chemical Physics,* **1953**, *21*, 1272.

[57] Edwards, S. F. The statistical mechanics of polymerized material. *Proceedings of the Physical Society,* **1967**, *92*, 9-16.

[58] de Gennes, P. G. Reptation of a polymer chain in the presence of fixed obstacles. *The Journal of Chemical Physics*, **1971**, *55*, 572.

[59] Ediger, M. D.; Angell, C. A.; Nagel, S. R. Supercooled liquids and glasses. *The Journal of Physical Chemistry*, **1996**, *100*, 13200-13212.

[60] Alegria, A.; Guerrica-Echevarria, E.; Goitiandia, L.; Telleria, I.; Colmenero, J. α-relaxation in the glass transition range of amorphous polymers. Temperature behavior across the glass transition. *Macromolecules*, **1995**, *28*, 1516-1527.

CHAPTER 2

Experimental Techniques

2.1. Gel permeation chromatography

Gel permeation chromatography (GPC) is a type of size exclusion chromatography (SEC) in which molecules are sorted based on their size. J. C. Moore of the Dow Chemical Company first introduced the term GPC [1], which has become a central characterization technique in both polymer industry and academic polymer research since then. In a typical procedure, a polymer solution is passed through a column packed with porous particles. A polymer sample comprises a polydisperse ensemble of macromolecules, therefore, chains of different size have different ability to penetrate the pores and pass through the column: smaller chains are withheld by most particle pores, and consequently take more time to elute, whereas larger chains can bypass most pores and elute faster. The separation is hence based on hydrodynamic radii (R_H) differences.

GPC is the most widely used experimental technique to measure molecular weight distributions of synthetic polymers. A frequently used technique to obtain quantitative data is to construct a calibration curve with well-defined monodisperse polymer standards of different molecular weight M_w. The M_w of the sample can be estimated by interpolating its retention time along the curve. Among the concentration-sensitive detectors needed for this method, refractive index (RI) detectors and UV detectors are the most versatile and common. Equation 2.1 relates the concentration c of a dissolved analyte with the refractive index of the solution n, solvent n_0 and analyte n_p [2].

$$n \propto n_0 + c(n_p - n_0) \tag{2.1}$$

UV detectors rely on the Beer−Lambert law, which relates the absorbance of a solution and its concentration. However, these are only suitable for UV-active polymers, and are therefore less common than RI detectors.

In addition to the relative data obtained by calibration methods, absolute molecular weight measurements are possible with the use of multi-angle light scattering (MALS) detectors. MALS provides retention time independent M_w values, as the angular variation of the scattered light is directly related to the size of the material. Equation 2.2 shows the relation between the intensity of the scattered light I_s, the polymer molar mass M and the concentration c.

$$I_s \propto \mathrm{M\ c} \left(\frac{dn}{dc}\right)^2 \tag{2.2}$$

Viscometers are also often coupled to GPC columns as they provide a facile way to measure the hydrodynamic volume V_H. The intrinsic viscosity of the solution [η] is related to V_H through the Einstein−Simha relation (Equation 2.3), where M is the molar mass of the polymer and N_A is Avogadro's number.

$$V_H = \left(\frac{M[\eta]}{2.5N_A}\right) \tag{2.3}$$

Combination of intrinsic viscosity measurements and molecular weight enables the study of the polymer conformation by means of the Mark−Houwink−Sakurada equation (Equation 2.4).

$$[\eta] = KM^{\alpha} \tag{2.4}$$

Here, K and α values depend on the specific polymer−solvent system. An α value of zero represents a solid sphere, 0.5 random coils in theta conditions, 0.5−0.8 linear polymers in a good solvent and 1.8−2 values a rigid rod conformation.

Concerning SCNP synthesis, the collapse of the polymer precursor and consequent decrease of hydrodynamic volume can be easily monitored and quantified by GPC [3]. Moreover, shape−related information is of great value to unravel the intriguing mechanisms of nanoparticle formation, as well as to elucidate the impact of other factors such as polymer composition or solvent effects.

In this work, GPC measurements were carried out at 30 ºC on an Agilent 1200 system (Figure 2.1) equipped with PLgel 5 µm Guard and PLgel 5 µm MIXED-C columns, a differential refractive index (RI) detector (Optilab Rex, Wyatt), a multiangle laser light scattering (MALLS) detector (MiniDawn Treos, Wyatt), and a viscosimetric (VI) detector (Viscostar-II, Wyatt). Data analysis was performed with ASTRA Software (version 6.1) from Wyatt. THF was used as eluent at a flow rate of 1 mL/min.

Figure 2.1. GPC equipment used in this work.

2.2. Nuclear magnetic resonance

Nuclear magnetic resonance (NMR) spectroscopy is a broadly extended characterization technique in which an external magnetic field is applied to the sample, inducing the excitation of the nuclei, and radio waves are employed to promote transitions between nuclear spin energy levels (resonance) [4]. This resonance frequency is given by the intramolecular magnetic field around the atom, and consequently gives information about the chemical environment. As the precise resonant frequency is influenced by the magnetic field employed, a reference frequency (typically that of tetramethylsilane) is employed to remove this dependence. The resonant frequency of a nucleus relative to the reference is known as chemical shift δ (Equation 2.5), where ν and ν_0 are the resonant frequencies of the analyte and the reference, respectively.

$$\delta = \frac{\nu - \nu_0}{\nu_0} \tag{2.5}$$

Although many nuclei can be observed by this technique, ^{1}H NMR and ^{13}C NMR are the most relevant in polymer chemistry, as these atoms are present in almost all macromolecules. 1D (single nucleus) and 2D (combination of two nuclei) spectra provide critical information for SCNP synthesis, as they give precise information of the chemical composition of the polymers and allow monitoring the chemical changes that occur upon SCNP formation [5].

Figure 2.2. NMR equipment used in this work.

NMR can also be used to perform structural and conformational analyses [6], however, as it was not the case for this work, I will not delve further.

^{1}H NMR and ^{13}C NMR spectra were acquired at room temperature on a Bruker Avance spectrometer operating at 300, 400 and 500 MHz, equipped with a Z-gradient BBO probe, using deuterated solvents.

2.3. Fourier−transform infrared spectroscopy

Fourier−transform infrared spectroscopy (FTIR) is a technique used to record the infrared spectrum of a given substance [7]. As the vibrational frequencies of most molecules fall into the infrared region of the electromagnetic spectrum, FTIR is a powerful technique to analyse the chemical composition [8]. Unlike other spectroscopic techniques, FTIR does not require a monochromatic beam. Instead, the sample is irradiated with the entire range of frequencies simultaneously, and the absorption at each wavelength is inferred performing a Fourier Transform afterwards.

In a typical FTIR experiment, the sample is mixed with a non−absorbing salt (commonly KBr) to form a pellet, which is later exposed to the IR beam. However, the development of attenuated total reflection (ATR) techniques has simplified the sample preparation procedures. In an ATR−FTIR experiment, the sample is directly placed on a high refractive index crystal. A beam of infrared light is passed through the crystal in such a way that it reflects at least once off the internal surface in contact with the sample. This reflection forms an evanescence wave that extends into the sample. After performing multiple internal reflections, the beam is finally collected as it exits the crystal.

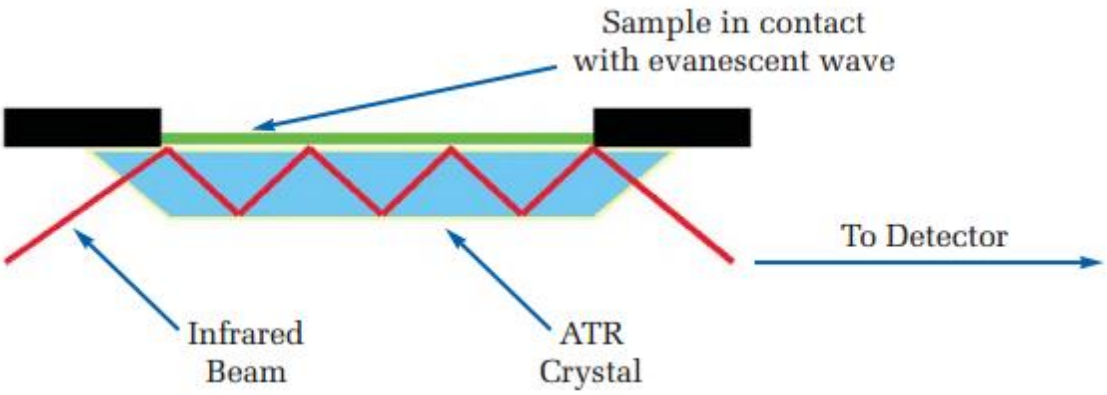

Figure 2.3. Schematic illustration of an ATR set−up.

FTIR is broadly used in polymer chemistry and SCNP synthesis [9], as it provides complementary information to other spectroscopic techniques.

In this work, ATR−FTIR spectra were recorded at room temperature on a JASCO 3600 FTIR spectrometer.

2.4. Ultraviolet−visible spectroscopy

Ultraviolet-visible spectroscopy (UV−Vis) probes the electronic transitions of the materials by the use of ultraviolet−visible light ($\lambda \approx 200 - 800$ nm) [10]. Typical observable electronic transitions include n−π* and π−π* for unsaturated systems and charge−transfer transitions for metal−ligand complexes.

Although NMR and FTIR receive most attention for polymer and SCNP characterization, UV-Vis spectroscopy is a valuable tool for relevant chemical transformations such as chain−transfer agent modification [11] or metal−ligand induced SCNP formation [12].

In this work, UV-Vis measurements were performed at room temperature on an Agilent 8453A apparatus with a Peltier thermostatic cell holder, T−controller 89090A.

Figure 2.4. UV-Vis equipment used in this work.

2.5. Differential scanning calorimetry

Diferential scanning calorimetry (DSC) is an analytic technique that measures the amount of energy needed to increase the temperature of the sample as a function of temperature [13]. The underlying physical principle is that during physical

transformations such as phase transitions, the sample requires more (endothermic process) or less (exothermic process) heat to maintain the same temperature when compared to a stable reference material.

In addition to thermodynamic phase transitions, DSC is capable of detecting other physical changes such as glass transitions, which makes it a particularly valuable technique for the physical characterization of polymers in general [14] and SCNPs in particular [15].

DSC measurement in this work were carried out on a Q2000 TA Instruments in standard mode. A helium rate of 25 mL/min was used throughout. Measurements were performed by placing the samples in sealed aluminium pans.

Figure 2.5. DSC equipment used in this work.

2.6. Transmission electron microscopy

Transmission electron microscopy (TEM) is a microscopy technique in which a beam of electrons is passed through a thin (thickness < 100 nm) sample [16]. Transmitted

electrons reach a fluorescent screen where the image is projected. The contrast of the image is a function of the density of the material, as higher densities increase the scattering events, allowing fewer electrons reach the detector. Selective addition of heavy metals to specific parts of the sample can improve the contrast of the image. The resolution of electronic microscopes is significantly higher than the resolution of light microscopes, due to the much smaller associated wavelength of electrons compared to light.

Several authors have employed TEM to observe the size and morphology of SCNPs in dry state [9, 17].

TEM measurements were performed using a high-resolution transmission electron microscope TECNAI G220 TWIN (Figure 2.6). The measurements were carried out by using an accelerating voltage of 200 kV under low dose conditions.

Figure 2.6. TEM equipment used in this work.

2.7. Elemental analysis

Elemental analysis (EA) provides information about the chemical elements present in a sample and their proportions. The most widely used type of elemental analysis in organic chemistry and polymer science is combustion analysis. In this technique, the sample is burned and the combustion products (CO_2, H_2O, NO) are collected and weighed. The composition of the sample (C, H, N, S) can be calculated from the obtained masses.

Elemental analysis measurements were performed in a Euro EA3000 Elemental Analyzer provided by the general research services at the University of the Basque Country.

2.8. Neutron scattering

In a scattering experiment a beam of particles (typically photons or neutrons) is shot towards a given sample to obtain information about the structure and/or the dynamics by analysing the scattered particles into a given solid angle dΩ. The difference between the wavevectors of the incident particles $\vec{k}$ and the scattered particles $\vec{k'}$ is called the scattering vector $\vec{Q}$, which modulus follows Q = k' - k. The Q-dependence of the measured magnitudes provides special resolution, as the spatial scale probed ζ is inversely proportional to the Q-value: $\zeta \sim 2\pi / Q$. Therefore, by tuning the Q-value it is possible to explore different spatial scales.

In a diffraction experiment the number of scattered particles into a solid angle is measured (the differential scattering cross-section $d\sigma/d\Omega$), which gives information about the structure of the sample. In quasielastic measurements, also the energy of the scattered particles E' is analized. The energy change between the incident and scattered

particles ħω = E' – E, can provide valuable information about the dynamics of the sample.

In quasielastic neutron scattering (QENS) experiments, the double differential scattering cross-section $d^2\sigma/(d\Omega d\hbar\omega)$ is measured, which counts the number of electrons scattered into a solid angle between Ω and Ω + dΩ, which have experienced an energy change between ħω and ħω + dħω. This magnitude depends on the interactions between the atoms in the sample and the probe particles (quantified by the scattering length b_α). In neutron scattering, b_α depends on the isotope considered, as neutrons interact with the nucleus. Table 2.1 summarizes the scattering lengths of the most common elements used in polymer science [18].

In $d^2\sigma/(d\Omega d\hbar\omega)$ we can identify a coherent (related with pair correlations) and an incoherent contribution (related with atom self-motions) (Equation 2.6).

$$\frac{\delta^2\sigma}{\delta\hbar\delta\Omega} = \left(\frac{1}{4\pi\hbar}\right)\frac{k}{k_0}\left\{\sum_{\alpha,\beta}\bar{b}_\alpha\bar{b}_\beta\, S_{\alpha\beta}^{coh}(\vec{Q},\omega) + \sum_\alpha \overline{\Delta b^2}_\alpha\, S_\alpha^{incoh}(\vec{Q},\omega)\right\} \qquad (2.6)$$

Table 2.1. Average length scales $\bar{b}_\alpha$, their squares $\bar{b}_\alpha{}^2$, and their deviations $\overline{\Delta b^2}_\alpha$ for different isotopes. Reproduced from Ref. 18.

Isotope	$\bar{b}_\alpha/fm$	$\bar{b}_\alpha{}^2/fm^2$	$\overline{\Delta b^2}_\alpha\ /\ fm^2$
^{1}H	-3.7406	13.992	638.78
^{2}H (D)	6.6710	44.502	16.322
^{12}C	6.6511	44.237	0
^{16}O	5.8030	33.675	0

The indexes (α, β) represent the different isotopes in the sample. The incoherent contribution arises from the random deviations of the scattering lengths from their mean

value, $\overline{\Delta b^2}_{\alpha}$. For hydrogen-containing systems, the large value of $\overline{\Delta b^2}_{H}$ implies that the signal is dominated by the incoherent scattering from hydrogens, whereas in fully deuterated samples the coherent contribution dominates the scattering and, since $\bar{b}_D \approx \bar{b}_C$ all correlations are almost equally weighted.

2.8.1. Small-angle neutron scattering (SANS): D11

Small-angle neutron scattering (SANS) is a widely used technique in soft matter, as it allows to resolve structures of the order of 1 – 100 nm [19].

The measured intensity I(Q) is the sum of coherent and incoherent elastic scattering. Since the incoherent contribution is Q-independent, structural information can only be obtained from the coherent fraction, whilst the incoherent part manifests as flat background noise.

The parameters affecting the coherent signal are the form factor P(Q) and the structure factor S(Q). P(Q) accounts for the scattering from a single particle, which depends basically on its size and shape. S(Q) contains information about the correlations between different particles, i.e. the structure of the material.

SANS measurements were performed at the D11 instrument (Figure 2.7) at the Institute Laue Langevin (ILL) in Grenoble (France).

Figure 2.7. Picture of the D11 instrument at ILL.

2.8.2. Neutron spin echo (NSE): IN11

Neutron spin echo (NSE) is a quasielastic neutron scattering (QENS) technique that codes, for each neutron individually, the energy transfer in the scattering process into its spin rotation [20]. Precession magnetic fields are applied before and after the scattering event, so that the polarization of the neutron depends only on the velocity difference of each neutron individually. NSE allows to explore broader time and length scales than other QENS techniques. The magnitude measured in an NSE experiment is:

$$\tilde{S}_{NSE}(Q,t) = \frac{I_{coh}\tilde{S}_{coh}(Q,t) - \frac{1}{3}I_{inc}\tilde{S}_{inc}(Q,t)}{I_{coh} - \frac{1}{3}I_{inc}} \qquad (2.7)$$

Where $S_{coh}(Q,t)$ and $S_{inc}(Q,t)$ are the normalized intermediate pair and self-correlation functions. I_{coh} and I_{inc} are the total static coherent and incoherent intensities.

The Neutron Spin Echo Spectrometer IN11c at the Institute Laue Langevin (ILL) was used to study the dynamic structure factor in the $0.15 \leq Q \leq 1.64$ Å^{-1} range on fully deuterated samples.

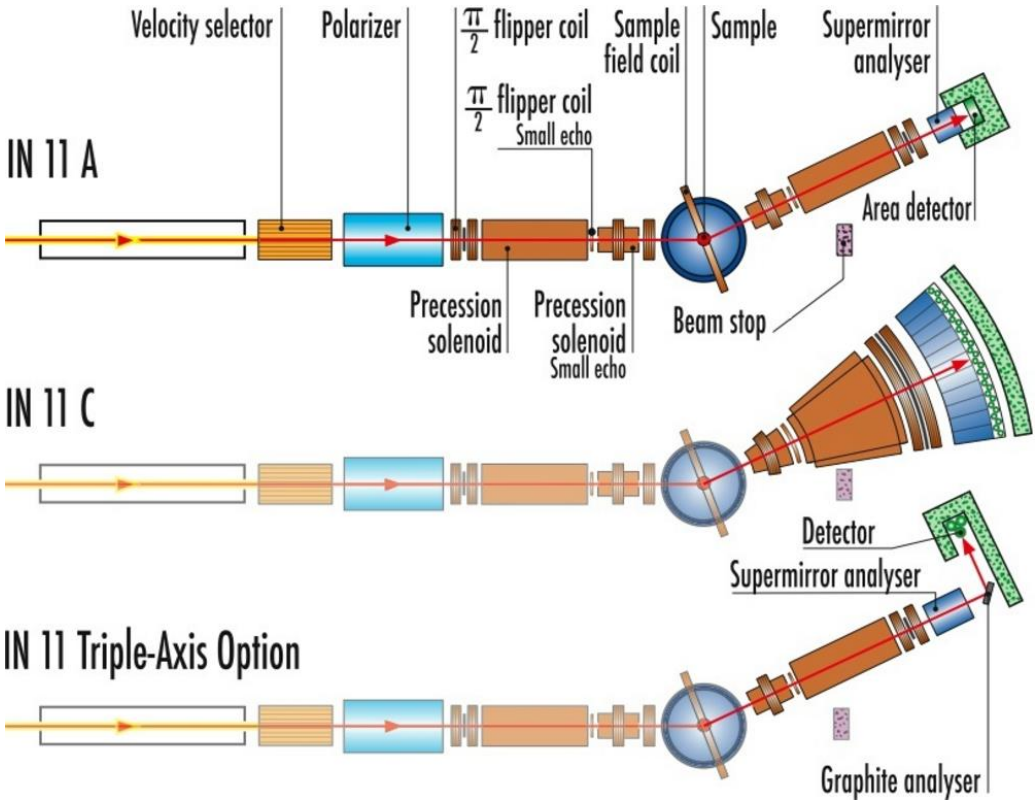

Figure 2.8. Scheme of the different NSE instrument setups available at ILL.

2.8.3. Time-of-flight neutron scattering: FOCUS

Time-of-flight (ToF) spectrometers measure the number of neutrons arriving at each detector as a function of the time of flight. The beam is pulsed by a combination of choppers and a crystal monochromator. This enables also to tune the incident energy, while the final energy is calculated from the time of arrival in the detectors and the flight path.

QENS experiments on bulk protonated samples were performed on the time-of-flight FOCUS instrument (Figure 2.9) at the Paul Scherrer Institute (PSI) in Villigen (Switzerland) in the $0.22 \leq Q \leq 1.84$ Å^{-1} range.

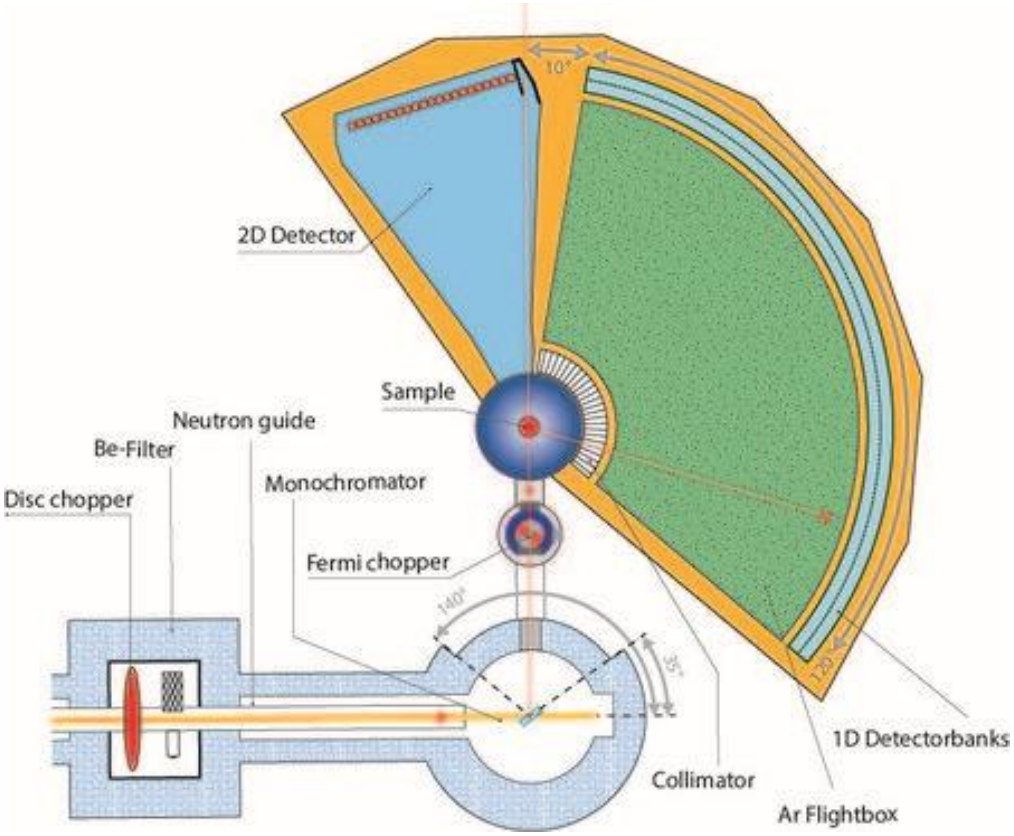

Figure 2.9. Layout of time-of-flight spectrometer FOCUS at PSI.

2.8.4. Backscattering spectrometry: SPHERES

Backscattering (BS) spectrometry is another QENS technique. Figure 2.10 shows the layout of the SPHERES instrument. Incoming neutrons are pre-monochromized by a velocity detector. The beam is then focused and reaches a rotating chopper, where it is reflected towards the monochromator. The monochromator selects an energy band $E_i \pm \delta E$, so that neutrons within this band are backscattered to the sample. Neutrons scattered by the sample hit the analysers, where only neutrons within a narrow energy distribution

$E_f \pm \delta E$ are sent back to the sample. Finally, after traversing the sample (BS samples should have transmissions of ≈ 90 %) the neutrons reach the detector.

Backscattering measurements on bulk protonated samples were perfomed on the SPHERES spectrometers at the Heinz-Maier-Leibnitz Zentrum in Garching (Germany).

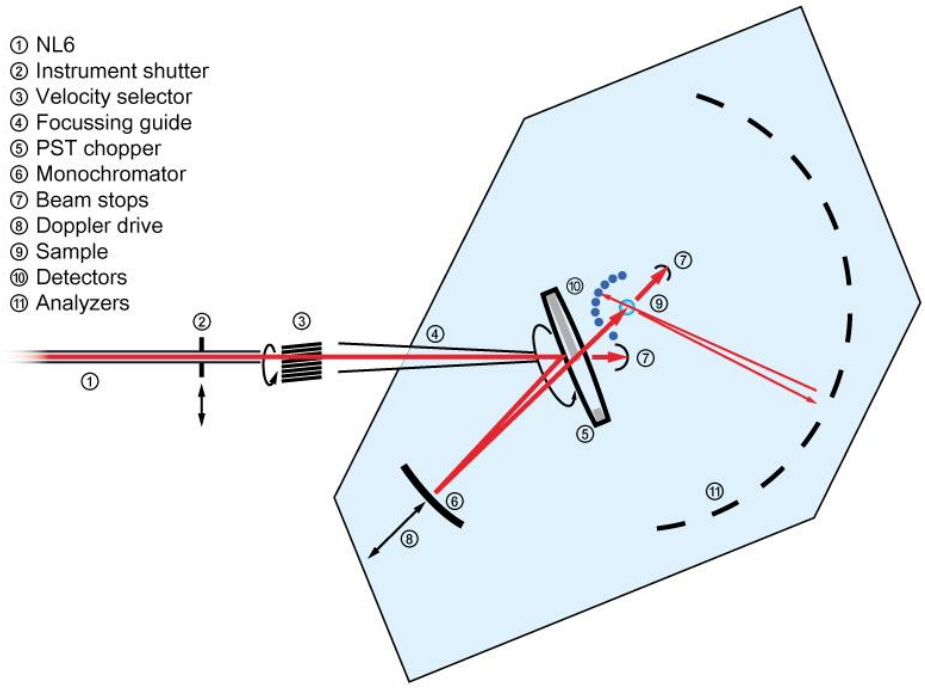

Figure 2.10. Layout of backscattering spectrometer SPHERES at FRM II in Garching.

2.9. Broadband dielectric spectroscopy (BDS)

Dielectric spectroscopy (DS) is a widely used technique in polymer physics that measures the dielectric properties of a medium to extract information about relaxation processes [21].

The application of an external oscillating electric field leads to an orientation of the molecular dipoles in the direction of the field (Figure 2.11). The subsequent loss of

polarization due to thermal noise can be monitored since it gives rise to a band in the imaginary part of the dielectric permittivity ε'' (Equation 2.8):

$$\epsilon^*(\omega) = \epsilon'(\omega) - i\epsilon''(\omega) \tag{2.8}$$

Where ε* is the complex permittivity and ε' the real part, with ω = 2πf.

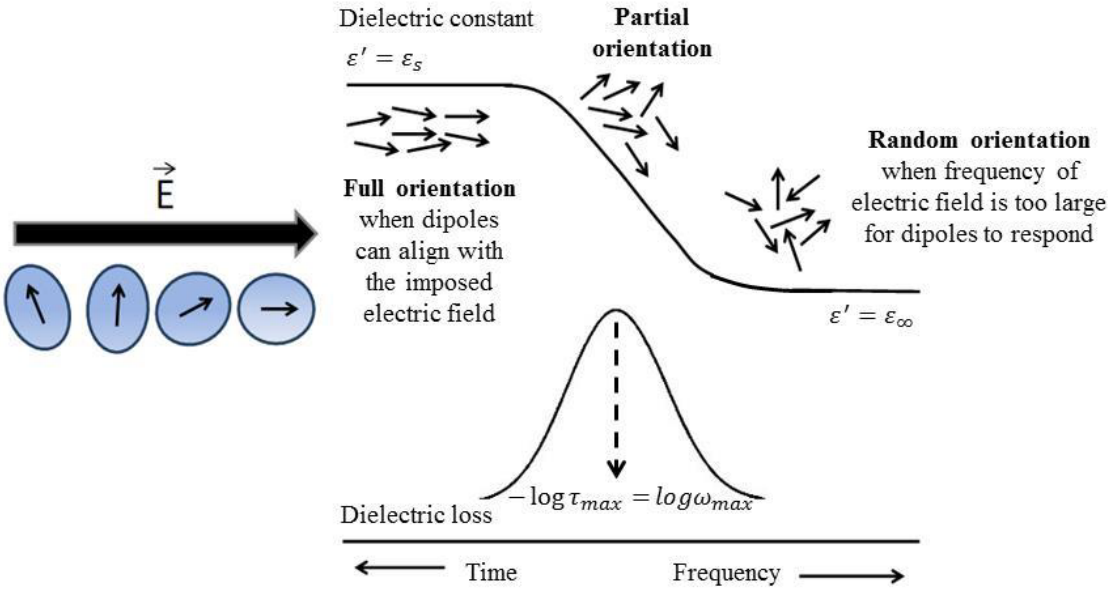

Figure 2.11. Dipole reorientations after applying an external electric field and the subsequent loss of polarization.

The frequency of the maxima of the loss peak in a dielectric spectrum is commonly used to obtain the relaxation time of characteristic dynamic processes (α-relaxation, β-relaxation…) in polymers:

$$\tau = \frac{1}{2\pi\omega} \tag{2.9}$$

Dielectric spectroscopy measurements were carried out with an Alpha-A Novocontrol dielectric analyzer (10^{-2} – 10^{7} Hz, Figure 2.12) and an Agilent 4291B Impedance analyzer (10^{6} – 10^{9} Hz).

Figure 2.12. Setup of the Alpha-A Novocontrol dielectric analyzer used in this work.

2.10. Rheology measurements

Rheology is the study of the flow and deformations of matter under externally applied forces. It is particularly interesting to study materials whose properties are between purely elastic and Newtonian fluids. In this regard, it is a very convenient tool to investigate the interesting mechanical properties of polymers, which have been extensively exploited for industrial applications [22].

Most polymers show a viscoelastic behavior when undergoing deformation [23]. This means that they exhibit characteristics of both viscous and elastic materials and, consequently, a time-dependency of the strain.

For polymers, the energy of plastic deformation can be related to the dynamic shear loss modulus (G'') and the elastic deformation to the dynamic shear storage modulus (G'). Dynamic mechanical spectroscopy measurements, where a sinusoidal stress is applied and the strain is measured, allow determining these moduli (Figure 2.13).

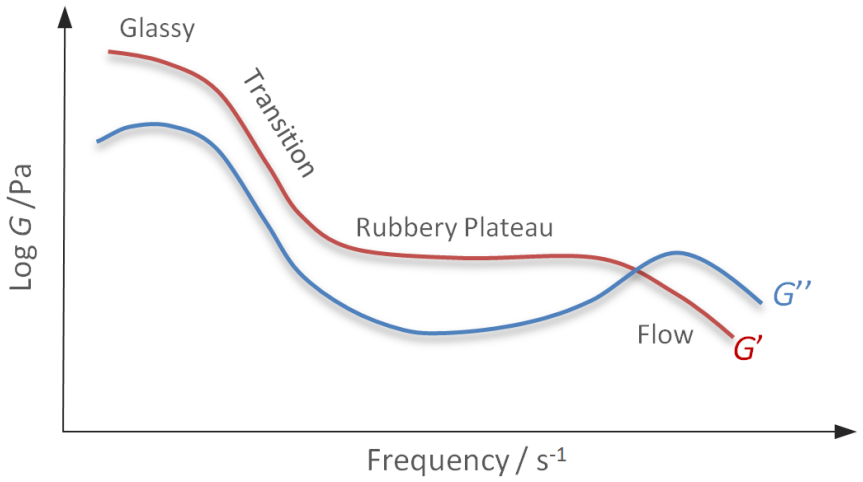

Figure 2.13. Example of a dynamic mechanical spectrum.

G' and G'' are related with fundamental properties of polymers, such as the glass transition temperature or the entanglement molecular weight, which can be calculated from the modulus in the plateau region, where G' is proportional to the number of physical and chemical crosslinks per unit volume.

Rheological experiments in the linear regime (≈ 0.03 – 16 Hz) were performed by using an ARES torsional rheometer (Figure 2.14) with a parallel plate geometry.

Figure 2.14. Picture of an ARES torsional rheometer.

2.11. References

[1] Moore, J. Gel permeation chromatography. I. A new method for molecular weight distribution of high polymers. *Journal of Polymer Science. Part A: General Papers*, **1964**, *2*, 835-843.

[2] Striegel, A.; Yau, W. W.; Kirkland, J. J.; Bly, D. D. Modern size-exclusion liquid chromatography: practice of gel permeation and gel filtration chromatography. *John Wiley and Sons*, **2009**.

[3] Latorre−Sanchez, A.; Alegría, A.; Lo Verso, F.; Moreno, A. J.; Arbe, A.; Colmenero, J.; Pomposo, J. A. A useful methodology for determining the compaction degree of single−chain nanoparticles by conventional SEC. *Particle & Particle Systems Characterization*, **2016**, *33*, 373−381.

[4] Jacobsen, N. E. NMR spectroscopy explained: simplified theory, applications and examples for organic chemistry and structural biology. *John Wiley and Sons*, **2007**.

[5] Willenbacher, J.; Altintas, O.; Trouillet, V.; Knofel, N.; Monteiro, M. J.; Roesky, P. W.; Barner−Kowollik. Pd−complex driven formation of single−chain nanoparticles. *Polymer Chemistry*, **2015**, *6*, 4358−4365.

[6] Tonelli, A. E. Polymer microstructure: the conformational connection to NMR. *Modern Magnetic Resonance*, **2008**, *1*, 567−574.

[7] McDonald, R. S. Review: intrared spectroscopy. *Analytical Chemistry*, **1986**, *58*, 1906−1925.

[8] Siesler, H. W. Fourier transform infrared (FTIR) spectroscopy in polymer research. *Journal of Molecular Structure*, **1980**, *59*, 15−37.

[9] Perez−Baena, I.; Asenjo−Sanz, I.; Arbe, A.; Moreno, A. J.; Lo Verso, F.; Colmenero, J.; Pomposo, J. A. Efficient route to compact single−chain nanoparticles: photoactivated synthesis via thiol−yne coupling reaction. *Macromolecules*, **2014**, *47*, 8270−8280.

[10] Perkampus, H. H. UV-VIS spectroscopy and its applications. *Springer Laboratory*, **2013**.

[11] Boyer, C.; Granville, A.; Davis, T. P.; Bulmus, V. Modification of RAFT−polymers via thiol−ene reactions: a general route to functional polymers and new architectures. *Journal of Polymer Science: Part A: Polymer Chemistry*, **2009**, *47*, 3773−3794.

[12] Sanchez−Sanchez, A.; Arbe, A.; Colmenero, J.; Pomposo, J. A. Metallo−folded single−chain nanoparticles with catalytic selectivity. *ACS Macro Letters*, **2014**, *3*, 439−443.

[13] Hohne, G.; Hemminger, W. F; Flammersheim, H. J. Differential scanning calorimetry. *Springer Laboratory*, **2013**.

[14] Bershtein, A. A.; Egorov, V. M. Differential scanning calorimetry of polymers: physics, chemistry, analysis, technology. *Prentice−Hall International*, **1994**.

[15] Asenjo−Sanz, I.; Veloso, A.; Miranda, J. I.; Alegría, A.; Pomposo, J. A.; Barroso−Bujans, F. Zwitterionic ring−opening copolymerization of tetrahydrofuran and glycidyl plenyl ether with $B(C_6F_5)_3$. *Macromolecules*, **2015**, *48*, 1664−1672.

[16] Williams, D. B.; Carter, C. B. Transmission electron microscopy: a textbook for materials science. *Springer Science & Business Media*, **2013**.

[17] Wen, J.; Yuan, L.; Yang, Y.; Liu, L.; Zhao, H. Self−assembly of monotethered single−chain nanoparticle shape amphiphiles. *ACS Macro Letters*, **2013**, *2*, 100−106.

[18] Arbe, A.; Alvarez, F.; Colmenero, J. Neutron scattering and molecular dynamic simulations: synergetic tools to unravel structure and dynamics in polymers. *Soft Matter*, **2012**, *8*, 8257-8270.

[19] Hollamby, M. J. Practical applications of small-angle neutron scattering. *Physical Chemistry Chemical Physics*, **2013**, *15*, 10566-10579.

[20] Lindner, P.; Zemb, T. Neutrons, x-rays and light: scattering methods applied to soft condensed matter, *North Holland Delta Series*, **2002**.

[21] Kremer, F.; Schönhals, A. Broadband Dielectric Spectroscopy, *Springer*, **2003**.

[22] Campo, A. Industrial polymers, *Carl Hanser Verlag GmbH & Co*, **2007**.

[23] Ferry, J. D. Viscoelastic properties of polymers, *John Wiley & Sons*, **1980**.

CHAPTER 3

Synthesis of Polyether SCNPs

3.1. Introduction

Single chain technology is an emerging discipline that aims for the construction of a variety of functional soft nano−objects via chain compaction [1]. Among them, single−chain nanoparticles (SCNPs) are useful constructs showing ultrasmall size (5−20 nm) and promising prospects for nanomedicine, catalysis, sensing, and other diverse end−use applications [2−7].

As described in Chapter 1, SCNPs can be synthesized via intrachain cross−linking [8] using covalent [9−17] and dynamic covalent bonds [18−21] as well as supramolecular interactions [22−29]. SCNP synthesis typically consists of three steps [4]: (i) preparation of a SCNP precursor, often being a random copolymer synthesized via a controlled/living radical polymerization process (e.g., atom transfer radical polymerization (ATRP) [30], nitroxide−mediated radical polymerization (NMP) [31], reversible addition−fragmentation chain transfer (RAFT) polymerization [32]; (ii) functionalization of a SCNP precursor to introduce reactive cross−linking groups along the chain (e.g., by deprotection of masked reactive groups [33]) or by postpolymerization modification [34]; and (iii) intrachain cross−linking of such reactive functionalities under appropriate reaction conditions [8]. Sometimes, step ii is avoided by using monomers decorated with functional groups unreactive under the polymerization conditions.

In the light of the rapid expansion of single−chain technology related research in the last years, a large selection of SCNP precursors of different nature have been reported, including polystyrene, poly(metha)acrylate, poly(metha)acrylamide, and

polyoligo(ethylene)glycol (metha)acrylate derivatives [35]. Polycaprolactone−, polycarbonate−, and polynorbornene− based SCNP precursors have been synthesized via ring−opening polymerization (ROP) and ring−opening metathesis polymerization (ROMP) [35]. However, in spite of the significant interest in the synthesis of polyether derivatives with complex architectures such as star−shaped [36], cyclic [37], multicyclic [38], and supramolecular structures [39−40], access to polyether SCNPs has not been achieved yet.

Polyethers can be synthesized by living anionic or cationic ROP, depending on the cyclic ether monomer structure (i.e., oxiranes, oxolanes) [41−43]. Sometimes, the use of certain anionic or cationic ROP catalysts is not compatible with the use of functional monomers (e.g., alkyne functionalities show a tendency for cross−linking reactions under basic reaction conditions at high temperatures [44]), thus limiting the broad scope of these techniques for synthesizing polyether SCNP precursors.

Polytetrahydrofuran (polyTHF) polyols are polyethers widely used in the plastic and synthetic fiber industry, particularly in the technology of polyurethanes [45]. Poly(THF) is the key raw material to produce spandex fibers, which are intensively used for the production of athletic outfits, baby diapers and bandages, among other products.

Poly(THF) is obtained by cationic ROP of tetrahydrofuran (THF) with common initiators such as strong protonic acids (H_2SO_4, HSO_3F, or $HClO_4$) or Lewis acids (BF_3, PF_5, or $SbCl_5$) [42,46]. Introduction of functional groups into the poly(THF) backbone

is a way to generate, for instance, polyurethanes with modifiable pendant alkyne groups [47].

Barroso−Bujans *et al.* reported the synthesis of linear poly(THF) based copolymers decorated with (unreactive) phenyl moieties via $B(C_6F_5)_3$−promoted zwitterionic ring−opening polymerization (ZROP) of THF and glycidyl phenyl ether (GPE) at high THF content in the feed [48]. By replacing the GPE monomer by glycidyl propargyl ether (GPgE), we envisioned the facile access to polyether SCNPs by combining ZROP and highly efficient thiol−yne coupling (TYC) techniques. The photoactivated radical−mediated TYC reaction has emerged as a powerful technique [49−53] that can be carried out under UV irradiation in the presence of a photoinitiator with high efficiency and rapid kinetics (in certain cases, even in the presence of oxygen/water traces) [54,55].

3.2. Objectives

In this Chapter we report the synthesis and characterization of polyether SCNPs by combining zwitterionic ring−opening polymerization (ZROP) and thyol−yne coupling (TYC) techniques. We will synthesize linear copolymers of tetrahydrofuran (THF) and glycidyl propargyl ether (GPgE), poly(THF−*co*−GPgE), as well as terpolymers of THF, GPgE and glycidyl phenyl ether (GPE), poly(THF−*co*−GPgE−*co*−GPE). These polymerization reactions will be performed with high content of THF in the feed and $B(C_6F_5)_3$ acting as initiator. Photoactivated TYC between the naked alkyne functional groups present in the GPgE moieties and a dithiol homobifunctional cross−linker at high dilution conditions will promote chain folding and, consequently, SCNP formation.

The obtained nanoparticles will be characterized by different techniques, including SEC with triple detection, Fourier transform infrared (FTIR) spectroscopy, ^{1}H NMR spectroscopy, transmission electron microscopy (TEM), and differential scanning calorimetry (DSC).

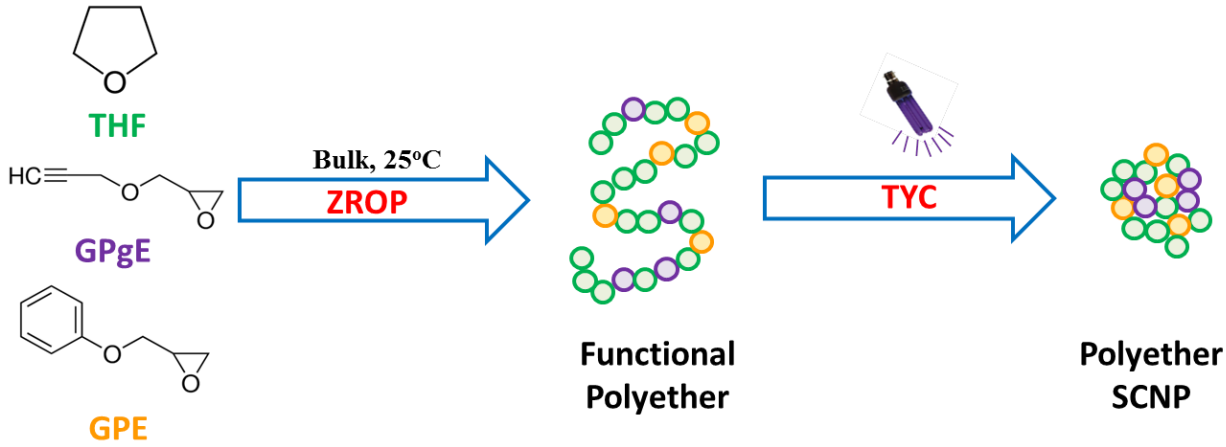

Scheme 3.1. Schematic illustration of the synthesis of poly(THF−*co*−GPgE−*co*−GPE) SCNPs.

3.3. Experimental part

3.3.1. Materials

Tetrahydrofuran (THF) and glycidyl phenyl ether (GPE) were dried over CaH_2, degassed, and distilled in a vacuum line before use. $B(C_6F_5)_3$ was sublimed in vacuum at 90 °C and stored in a glovebox. Any other reagent was used as received. $B(C_6F_5)_3$ (95%), GPE (99%), glycidyl propargyl ether (GPgE) (90%), 2,2−dimethoxy−2−phenylacetophenone (DMPA) (99%), 3,6−dioxa−1,8−octanedithiol (DODT) (95%), dichloromethane (CH_2Cl_2) (99.5%), deuterated chloroform ($CDCl_3$) (99.96%, containing 0.03% tetramethylsilane, TMS), and CaH_2 (99.9%) were purchased from Sigma−Aldrich. THF (99.5%) and methanol (MeOH) (99.9%) were purchased from Scharlau.

3.3.2. Synthesis of SCNP precursors via ZROP

All reactions were performed under an argon atmosphere in a vacuum line using Schlenk flasks. Copolymers of THF anf GPgE and terpolymers of THF, GPgE and GPE were synthesized at room temperature in bulk conditions (Scheme 3.2). Table 3.1 shows the reaction conditions of this study.

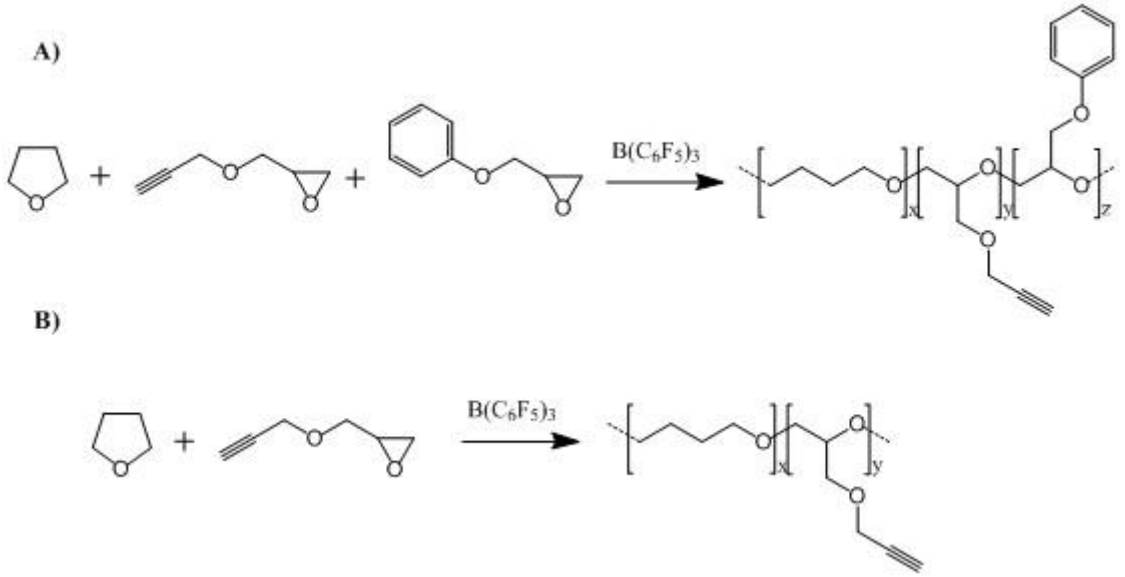

Scheme 3.2. Schematic illustration of the synthesis of precursors (A) poly(THF−*co*−GPgE−*co*−GPE) and (B) poly(THF−*co*−GPgE).

Table 3.1. Reaction conditions for the synthesis of SCNP precursors.

Sample	Monomer feed[a] (mol % THF/GPgE/GPE)	Composition[b] (mol %)	$[glycidyl]_0$[c] /$[B(C_6F_5)3]_0$ (mol/mol)	Reaction time (h)	Conversion[d] (%)
C1	80/20/0	79/21	950	24	8
C2	85/15/0	85/15	317	72	38
T1	60/20/20	62/18/20	1893	72	83
T2	80/10/10	77/10/13	1893	24	65

[a]THF = tetrahydrofuran; GPgE = glycidyl propargyl ether; GPE = glycidyl phenyl ether. [b]Obtained by integration of quantitative ^{1}H NMR signals. [c]$[glycidyl]_0$ = initial number of moles of GPgE + GPE. [d]Obtained by gravimetric analysis.

In a typical experiment (sample T2, Table 3.1), $B(C_6F_5)_3$ (2 mg, 3.9 μmol), tetrahydrofuran (2.4 mL, 30 mmol), glycidyl phenyl ether (0.5 mL, 3.7 mmol), and

glycidyl propargyl ether (0.4 mL, 3.7 mmol) were placed in a Schlenk flask and stirred at room temperature for 24 h. The reaction crude was dissolved in CH_2Cl_2 (≈ 0.5 mL), precipitated in MeOH, and dried at room temperature in a vacuum oven. Molecular weight, polydispersity and hydrodynamic radius of the samples synthesized in this work are reported in Table 3.2.

Table 3.2. Characteristics of SCNP precursors.

Sample	M_p[a] (kDa)	M_w/M_n	R_H[b] (nm)
C1	17.5	1.3	4.9
C2	16.7	1.3	4.7
T1	24.5	1.5	4.8
T2	42.6	1.6	6.5

[a]Absolute molecular weight at the peak maximum as determined by SEC/MALLS. [b]Hydrodynamic radius at the peak maximum as determined by SEC/VI.

3.3.3. Kinetic experiments via real−time ^{13}C NMR spectroscopy

Copolymerization and terpolymerization reactions were carried out in bulk by mixing the amounts of monomer and catalyst reported in Table 3.3.

Table 3.3. Amount of monomer and catalyst used in the kinetic study

Monomer feed (mol %)	THF (mL)	GPgE (mL)	GPE (mL)	$B(C_6F_5)_3$ (mg)	$[glycidyl]_0$[a]/$[B(C_6F_5)_3]_0$ (mol/mol)
50/50	0.38	0.50	−	4	594
80/20	0.75	0.25	−	20	59
33/33/33	0.28	0.37	0.47	6	594
80/10/10	0.75	0.12	0.16	20	59

[a]$[glycidyl]_0$ = initial number of moles of GPgE + GPE.

Monomers were first transferred into the NMR tube in a glovebox. After adjustment of NMR experimental parameters, the catalyst was added, and the tube was rapidly introduced in the equipment at ambient temperature. Monomer conversion was

evaluated from the signal integration of GPgE at 44.7 − 45.0 ppm, GPE at 45.1 − 45.4 ppm, and THF at 26.7 − 26.9 ppm by using the MestReNova software. The amounts of the reacted monomer were calculated as $(1 - I_t/I_0) \times 100$ for each monomer, where I_t is the signal integral at time *t* and I_0 is the signal integral at zero time of reaction.

3.3.4. Synthesis of polyether SCNPs via photoactivated thiol−yne coupling.

In a typical procedure, 50 mg of terpolymer (Sample T2, Table 3.2) was dissolved in THF (100 mL) in a rounded−bottom flask covered with aluminium foil. Then, DMPA photoinitiator (5 mg, 20 mmol) was added, and the mixture was kept under stirring until it was completely dissolved. After that DODT (8.8 μL, 0.5 μmol) was added. 15 mL of the reaction mixture was transferred to a vial, and it was exposed to UV irradiation (λ = 300 – 400 nm) for 160 minutes. The solvent was removed in the vacuum line, and the sample was dried at room temperature. Table 3.4 shows data corresponding to SCNPs prepared from terpolymer precursors of Table 3.2.

Table 3.4. Data for polyether SCNPs synthesized in this work.

Sample	Composition (mol % THF/GPgE/GPE)	M_p[a] (kDa)	Mp_{app}[b] (kDa)	M_w/M_n	R_H[c] (nm)
NP1	62/18/20	31.6	11.7	1.4	3.7
NP2	77/10/13	43.9	23.5	1.5	5.2

[a]Absolute molecular weight at the peak maximum as determined by SEC/MALLS. [b]Apparent molecular weight at the peak maximum calculated from the molecular weight vs retention time curve of the linear precursor. [c]Hydrodynamic radius at the peak maximum as determined by SEC/VI.

3.4. Results and discussion

3.4.1. Synthesis of SCNP precursors bearing naked alkyne functional groups via ZROP

Linear copolymers of poly(THF−*co*−GPgE−*co*−GPE) and poly(THF−*co*−GPgE) with different monomer compositions and molecular weights (Tables 3.1 and 3.2) were synthesized in this work. The amount of alkyne−bearing GPgE in all SCNP precursors was kept below 25 mol % trying to favor a random distribution of alkyne functional groups along the linear polymer chains. The presence of alkyne groups in the obtained polymers was verified and quantified by ^{1}H NMR measurements.

Figure 3.1 shows the ^{1}H NMR spectra of representative copolymer and terpolymer samples. As observed, both the copolymer and the terpolymer samples show a well−defined peak at δ = 2.43 ppm corresponding to alkyne C≡CH protons (signal “g”). ^{1}H NMR data also showed that alkyne groups did not present significant side reactions during ZROP of the alkyne−containing monomer with $B(C_6F_5)_3$, enabling the generation of SCNP precursors with naked alkyne groups.

The specific distribution of the reactive groups along the polymer chain is an important parameter in the synthesis of well−defined nanoobjects via chain compaction [56−58]. To evaluate the distribution of alkyne groups in the poly(GPgE−co−THF) copolymers and poly(THF−GPgE−GPE) terpolymers, we monitored the monomer consumption by in situ polymerization ^{13}C NMR experiments. The use of in situ ^{1}H and ^{13}C NMR techniques to study the monomer sequence distribution in ring−opening copolymerization reactions as well as in living carbanionic and anionic polymerizations has been lately developed by Frey and co−workers [59−62].

Concurrent incorporation of comonomers into the growing polymer chain during the whole reaction time and the nondeviation from the initial ratio of comonomer feed have been explained as to lead to the formation of random copolymers [63].

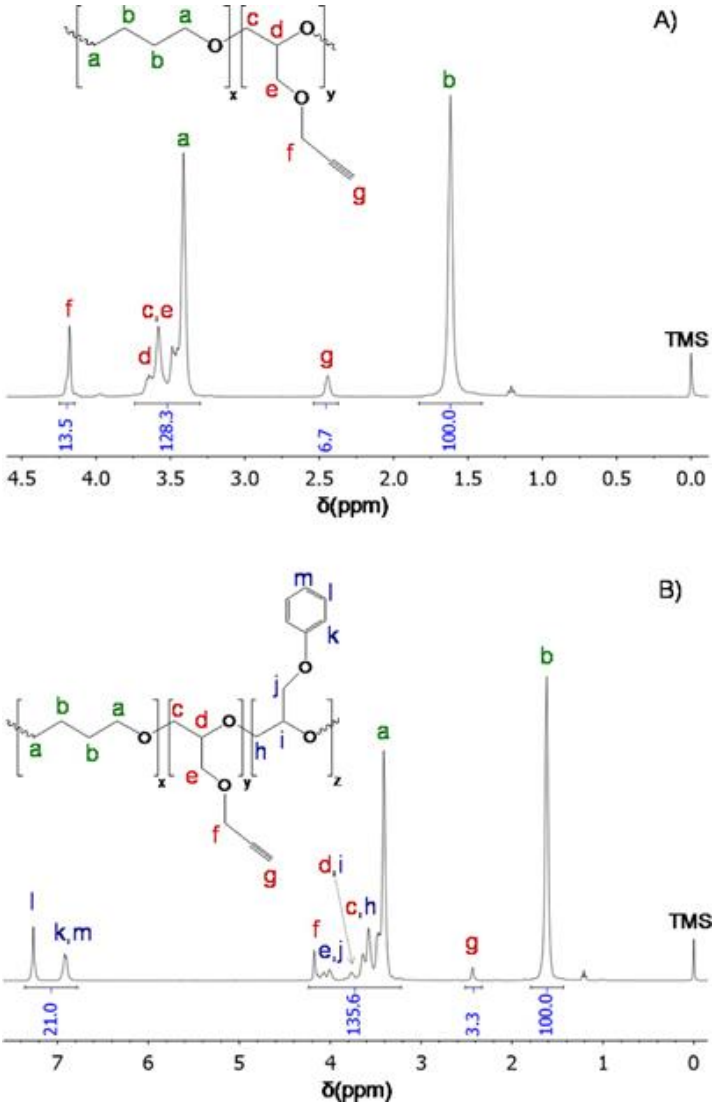

Figure 3.1. ^{1}H NMR spectra: (A) poly($THF_{0.79}$−co−$GPgE_{0.21}$) (C1, Table 3.1) and (B) poly($THF_{0.77}$−$GPgE_{0.10}$−$GPE_{0.13}$) (T2, Table 3.1).

Barroso−Bujans *et al.* studied the ZROP of THF and GPE initiated by $B(C_6F_5)_3$ [48]. In this system the composition of the monomers was observed to continually change with

time, as determined by in situ ^{13}C NMR experiments, suggesting the formation of gradient copolymers. It is expected from previous studies [64] that the monomer distribution shows a dependence on the monomer feed composition. For that reason, we first studied the monomer distribution of equimolar monomer mixtures in the copolymer and in the terpolymer, followed by THF−rich monomer mixtures.

Real−time ^{13}C NMR spectra for the bulk copolymerization of THF and GPgE, with a feed composition of 50/50 mol %, and for the bulk terpolymerization of THF, GPgE, and GPE with a feed ratio of 33/33/33 mol % are shown in Figure 3.2. The data show that ^{13}C NMR signals of monomers are well separated in the spectra and that they are not superposed to the signals of the resulting polymer, enabling data quantification. Analysis of the integration values allowed the calculation of monomer conversion as a function of time. Figure 3.3 shows the evolution of monomer conversion with time for the copolymerization (Figure 3.3A,C) and terpolymerization (Figure 3.3B,D) reactions with different monomer feed compositions.

Concerning the copolymerization of THF and GPgE with 50/50 mol % feed composition, the data in Figure 3.3A show that incorporation of THF in the copolymer is slightly faster compared to GPgE and that THF conversion reaches a maximum value of 95%, while GPgE is completely consumed. These results suggest the formation of a copolymer with random distribution of monomers with a slight gradient composition characterized by a higher incorporation of THF at the beginning of the polymerization and a higher incorporation of GPgE at the end. The incomplete THF conversion suggests that termination or transfer reactions might occur during copolymerization.

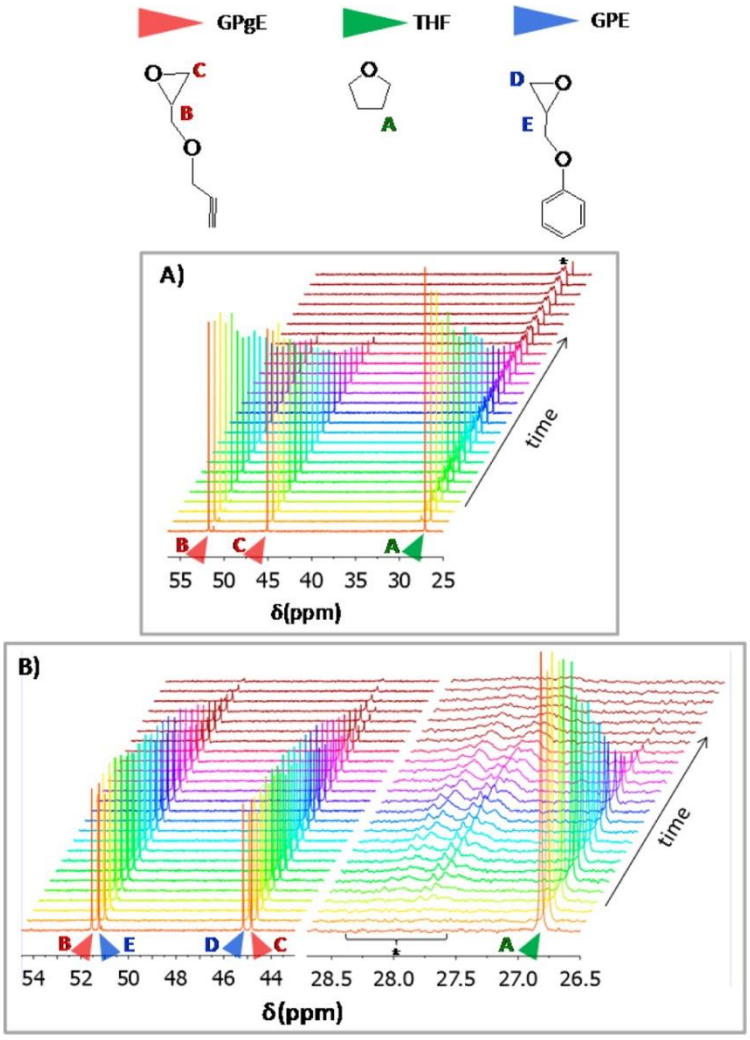

Figure 3.2. Real−time ^{13}C NMR spectra obtained during (A) bulk copolymerization of THF and GPgE with a feed composition of 50/50 mol % and (B) bulk terpolymerization of THF, GPgE, and GPE with a feed composition of 33/33/33 mol %. *Signals from THF moieties in the polymer.

On the basis of these results, we cannot accurately calculate the probability for incorporation of each monomer, as well as the reactivity ratios, as done by Frey et al. [61,62] for living carbanionic copolymerizations, but we can only provide a qualitative description of the compositional growth of chains. In the terpolymerization reaction with 33/33/33 mol % feed composition (Figure 3.3B), the THF also shows faster incorporation, followed by GPgE and GPE, respectively. In this case, the tendency to form gradient structures is much higher than in the copolymer, exhibiting a gradient profile in the order THF/GPgE/GPE.

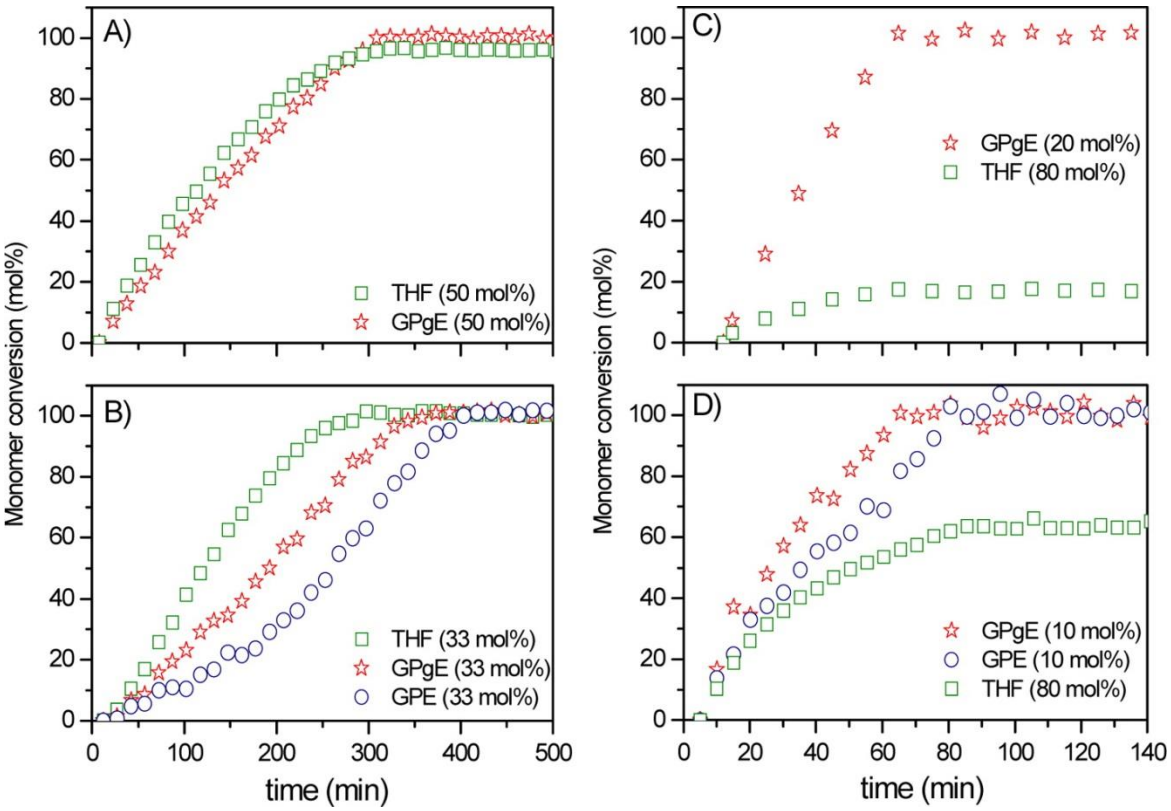

Figure 3.3. Monomer conversion as a function of time for the ZROP copolymerization (A, C) and terpolymerization (B, D) with different monomer feed compositions, as obtained by in situ ^{13}C NMR experiments (see Experimental Section).

Data analysis of real−time ^{13}C NMR experiments for feed monomer compositions of 80/20 mol % of THF/GPgE and 80/10/10 mol % of THF/GPgE/GPE is shown in Figure 3C,D. The data show that GPgE is completely consumed in about 60 min in both the copolymerization and the terpolymerization reactions, whereas the consumption of THF is stopped at such reaction time. The conversion of THF is only of 20 mol % in the copolymer, whereas it increases to 60 mol % in the terpolymer. Unexpectedly from these results, the monomer composition in the obtained polymers after purification was 71/29 mol % for poly(THF−co−GPgE) and 80/10/10 mol % for poly(THF−GPgE−GPE), suggesting a compositional heterogeneous growth of chains. It is likely that GPgE is consumed in parallel reactions to the copolymerization reaction, concurrently generating chains with high GPgE content.

In the terpolymerization reaction, the monomer consumption indicates the generation of statistical chains with a random distribution of monomers up to 20 min of reaction followed by a gradient−like consumption of monomers. The identical monomer composition in the obtained terpolymer as that in the feed, together with the incomplete consumption of THF, suggests that GPgE and GPE are likely consumed in parallel reactions to generate small chains with high content of GPgE and GPE. In spite of this, incorporation of THF in the terpolymer is much more favored than in the copolymer. As it will be shown below, the different monomer distribution in the copolymer and in the terpolymer has a profound effect on the formation of polyether SCNPs.

3.4.2. Synthesis of Polyether SCNPs via Photoactivated Thiol−Yne Coupling.

The linear poly(THF−co−GPgE) copolymers and poly(THF−GPgE−GPE) terpolymers synthesized in this work (Table 3.2) were evaluated as precursors for the synthesis of polyether SCNPs via photoactivated thiol−yne coupling (TYC). The photoactivated TYC reaction was carried out by working at appropriate dilution conditions (0.5 mg/mL) in the presence of 3,6−dioxa−1,8−octanedithiol (DODT) as homobifunctional cross−linker and 2,2−dimethoxy−2−phenylacetophenone (DMPA) as photoinitiator.

Figure 3.4 illustrates SEC/MALLS traces of the copolymer poly($THF_{0.79}$−co−$GPgE_{0.21}$) and the terpolymers poly($THF_{0.77}$−$GPgE_{0.10}$−$GPE_{0.13}$) and poly($THF_{0.62}$−$GPgE_{0.18}$−$GPE_{0.20}$) before and after the TYC reaction. Also included in this figure are the absolute molecular weight vs retention time curves for the precursors and SCNPs.

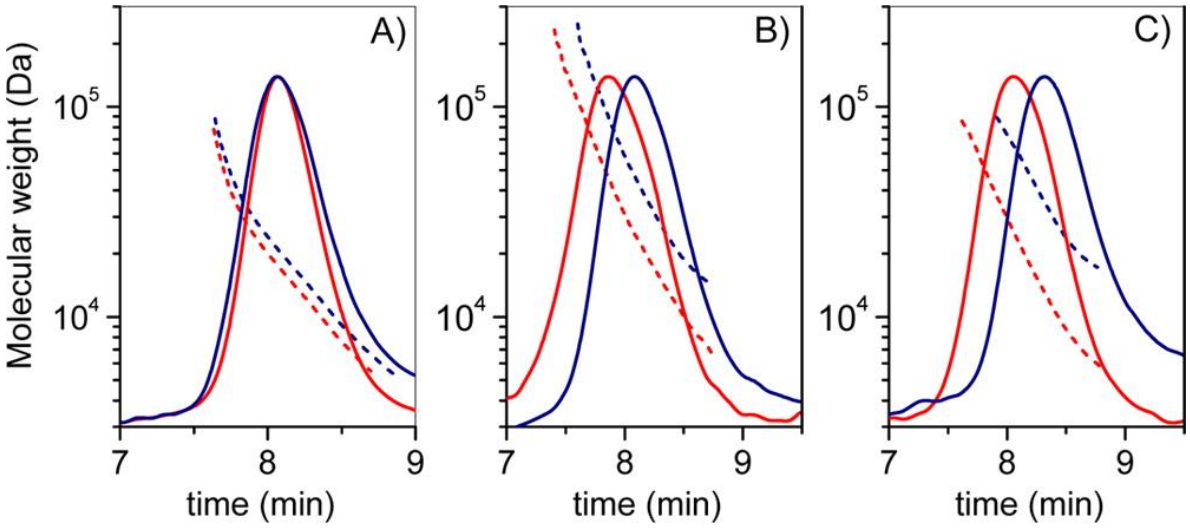

Figure 3.4. SEC/MALLS traces of copolymer poly($THF_{0.79}$−co−$GPgE_{0.21}$) (A) and terpolymers poly($THF_{0.77}$−$GPgE_{0.10}$−$GPE_{0.13}$) (B) and poly($THF_{0.62}$−$GPgE_{0.18}$−$GPE_{0.20}$) (C) before (red lines) and after (blue lines) the TYC reaction. Dashed lines are the corresponding curves of absolute molecular weight vs retention time.

All our attempts to produce polyether SCNPs from the poly(THF−co−GPgE) copolymers (Table 3.2) via photoactivated TYC failed, as no shift could be observed in the SEC/MALLS traces (see Figure 3.4A). We attribute this failure to the specific monomer distribution in the poly(THF−co−GPgE) copolymers and the compositional heterogeneous growth of chains, which according to ^{13}C NMR data (Figure 3.3C) is far from being a statistical one. Gradient−like copolymers highly enriched in GPgE at one of the extremes of the chain would be formed, presumably leading to only very local compaction upon TYC and, hence, to tadpole−like instead of SCNP structures. Conversely, poly(THF−GPgE−GPE) terpolymers synthesized via ZROP (Table 3.2) provide polyether SCNPs upon UV irradiation at λ = 300−400 nm for 160 min, causing a significant shift of the SEC/MALLS traces towards longer retention times (Figure 3.4B,C) and a reduction of the hydrodynamic radius (Tables 3.2 and 3.4).

The formation of the polyether SCNPs via TYC was accompanied by the disappearance of the vibration band located at 3240 cm^{-1} (≡C−H stretching), as clearly observed by

comparison of the FTIR spectra of the terpolymer and the SCNPs (Figure 3.5A). The ^{1}H NMR spectrum also revealed the disappearance of the ≡CH peak and the presence of new peaks from the methylene protons of the DODT cross−linker (Figure 3.5B). The degree of cross−linking of the SCNPs prepared from terpolymers containing 10 and 18 mol % of GPgE was found to be 71 and 98%, respectively.

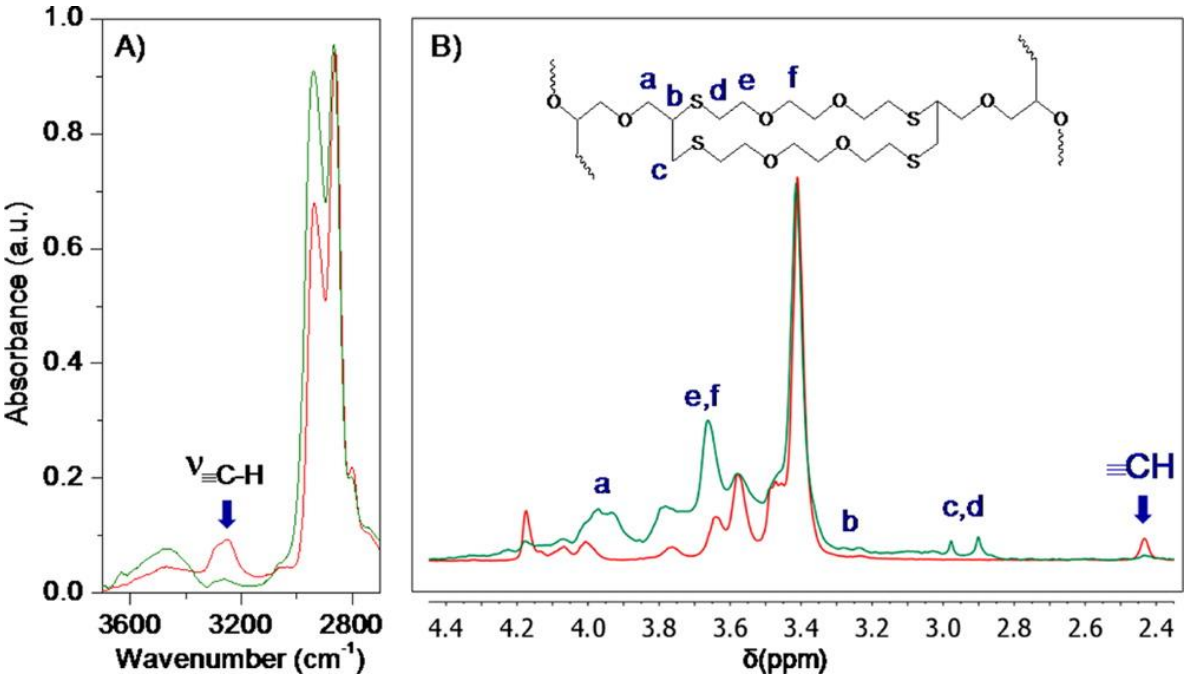

Figure 3.5. (A) Comparison of the FTIR spectra corresponding to the terpolymer P($TH_{F0.77}$−$GPgE_{0.10}$−$GPE_{0.13}$) (red trace) and SCNPs (green trace), showing the disappearance of the vibration band located at 3240 cm^{-1} (≡C−H stretching) upon SCNP formation via photoactivated TYC. (B) ^{1}H NMR spectrum of the SCNPs showing the disappearance of the ≡CH protons and the appearance of new peaks arising from the methylene protons of the DODT cross−linker.

A significant shift in the SEC chromatograms (Figure 3.4B,C) was observed upon polyether SCNP formation, when compared to the SEC traces of the corresponding linear precursors. This shift can be quantified by means of the value of apparent molecular weight at the peak maximum (M_p^{app}) calculated from the molecular weight vs retention time curve of the linear precursor. As an example, terpolymer poly($THF_{0.77}$−$GPgE_{0.10}$−$GPE_{0.13}$) displaying a value of M_p = 42.6 kDa showed a value

of M_p^{app} = 23.5 kDa upon SCNP formation. However, the actual value of M_p, as determined by the MALLS detector, was 43.9 kDa pointing to a successful formation of SCNPs. In fact, hydrodynamic data recorded via online SEC/VI revealed a reduction in R_H at the peak maximum from 6.5 nm, corresponding to the poly($THF_{0.77}$−$GPgE_{0.10}$−$GPE_{0.13}$) precursor, to 5.2 nm for the SCNPs (Tables 3.2 and 3.4). A similar trend was observed for the terpolymer poly($THF_{0.62}$−$GPgE_{0.18}$−$GPE_{0.20}$) having a higher content of alkyne functional groups (see Table 3.3).

More insight about the effect of the terpolymer composition on the hydrodynamic properties of the polyether SCNPs was obtained by analyzing the dependence of the intrinsic viscosity on the absolute molecular weight, as determined by SEC with triple (RI/MALLS/VI) detection. Mark−Houwink−Sakurada (MHS) plots for the terpolymer precursors and the corresponding SCNPs are shown in Figure 3.6. The corresponding values of the exponent a (MHS equation, $\log[\eta] = K_\eta M^a$) are also included for comparison.

As can be seen in Figure 3.6, for a given value of molecular weight, a significant reduction in intrinsic viscosity is observed upon SCNP formation. This reduction is higher for the terpolymer having a higher content of alkyne functional groups. Both terpolymer precursors showed a similar dependence of [η] on M, with a = 0.52. The exponent in the MHS equation can be related to the exponent ν from the dependence of the hydrodynamic radius on M ($R_H = K_H M^\nu$), by means of the following expression: $a = 3\nu - 1$. Consequently, for chains in good ($\nu \approx 0.6$) and theta ($\nu \approx 0.5$) solvents, values of a = 0.8 and a = 0.5 are expected, respectively, whereas for individual globules ($\nu \approx 0.33$) a value of a = 0 is predicted. According to the values of a reported in Figure 3.6, the

terpolymer precursors in THF at 30 °C behave as chains in a theta solvent (ν = 0.51), whereas the polyether SCNPs show more compact conformations in solution under such conditions. SCNPs from precursors poly($THF_{0.77}$–$GPgE_{0.10}$–$GPE_{0.13}$) and poly($THF_{0.62}$–$GPgE_{0.18}$–$GPE_{0.20}$) show ν = 0.48 and ν = 0.43, respectively, pointing to the relatively sparse conformations of these SCNPs in solution [65].

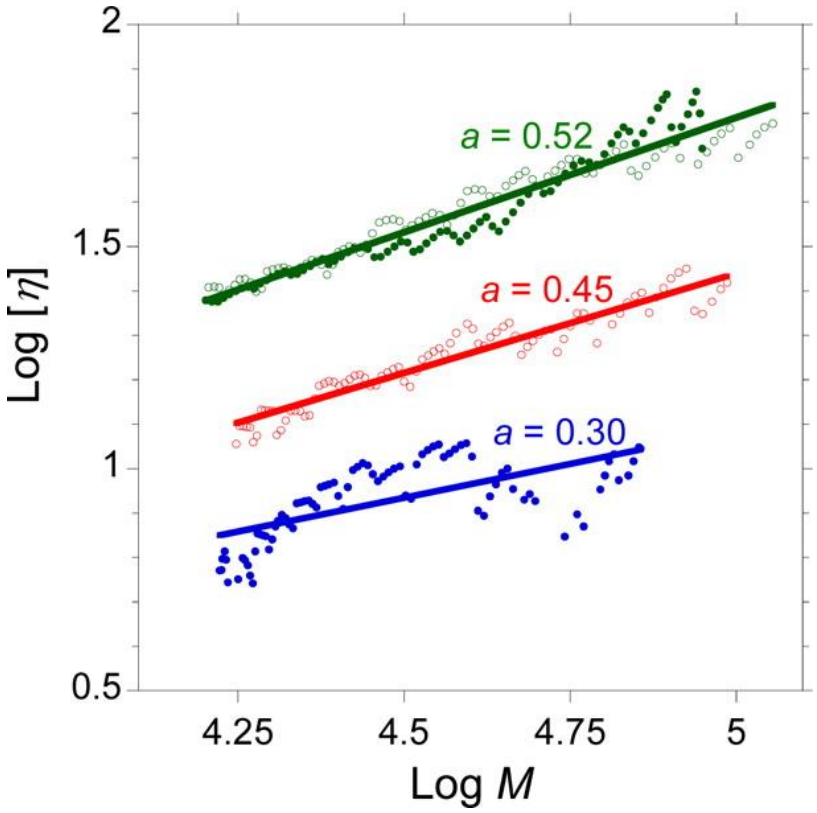

Figure 3.6. Mark–Houwink–Sakurada (MHS) plots for poly($THF_{0.77}$–$GPg_{E0.10}$–$GPE_{0.13}$) (open green circles) and poly($THF_{0.62}$–$GPgE_{0.18}$–$GPE_{0.20}$) (solid green circles) precursors and the corresponding SCNPs (open red circles and solid blue circles, respectively). Values of the *a* exponent according to the MHS equation $\log[\eta] = K_\eta M^a$ are given.

As reported for many other SCNP systems, a globular conformation was observed by TEM upon solvent removal (Figure 3.7). The high contrast provided by the electron–rich sulfur atoms present in the polyether SCNPs reveals the quasispherical shape of the nanoparticles in the dry state, with an average diameter of ca. 12 ± 3 nm.

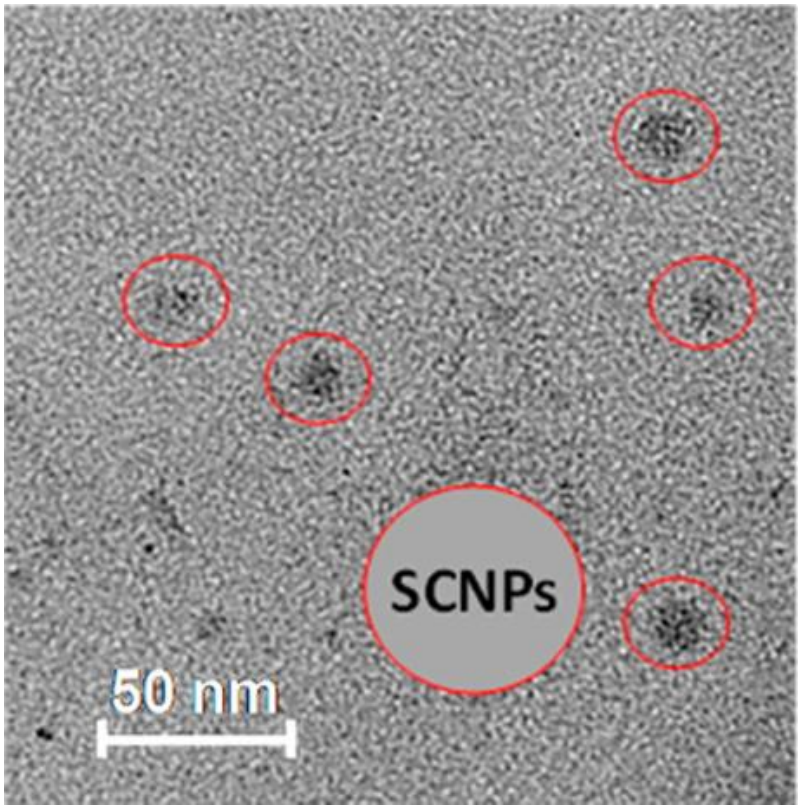

Figure 3.7. TEM picture illustrating the morphology in the dry state of polyether SCNPs prepared from the terpolymer poly($THF_{0.77}$−$GPgE_{0.10}$−$GPE_{0.13}$) via photoactivated TYC.

Finally, the thermal properties of the polyether SCNPs were investigated. The polyether SCNPs were found to be rubbery materials at room temperature, displaying no sign of crystallinity. Figure 3.8 shows the DSC traces of the terpolymer poly($THF_{0.77}$−$GPgE_{0.10}$−$GPE_{0.13}$) and the corresponding SCNPs in the temperature range where the glass transition was observed. Intrachain cross−linking produces a significant increase in the glass transition temperature (T_g), from −62.5 °C for the terpolymer to −55.0 °C for the SCNPs, which is in good agreement with theoretical expectations (i.e., reduction of the overall mobility leads to higher T_gs). However, due to the heterogeneity introduced by the intrachain cross−linking process, a significant broadening of the glass transition was observed when compared to that of the terpolymer precursor.

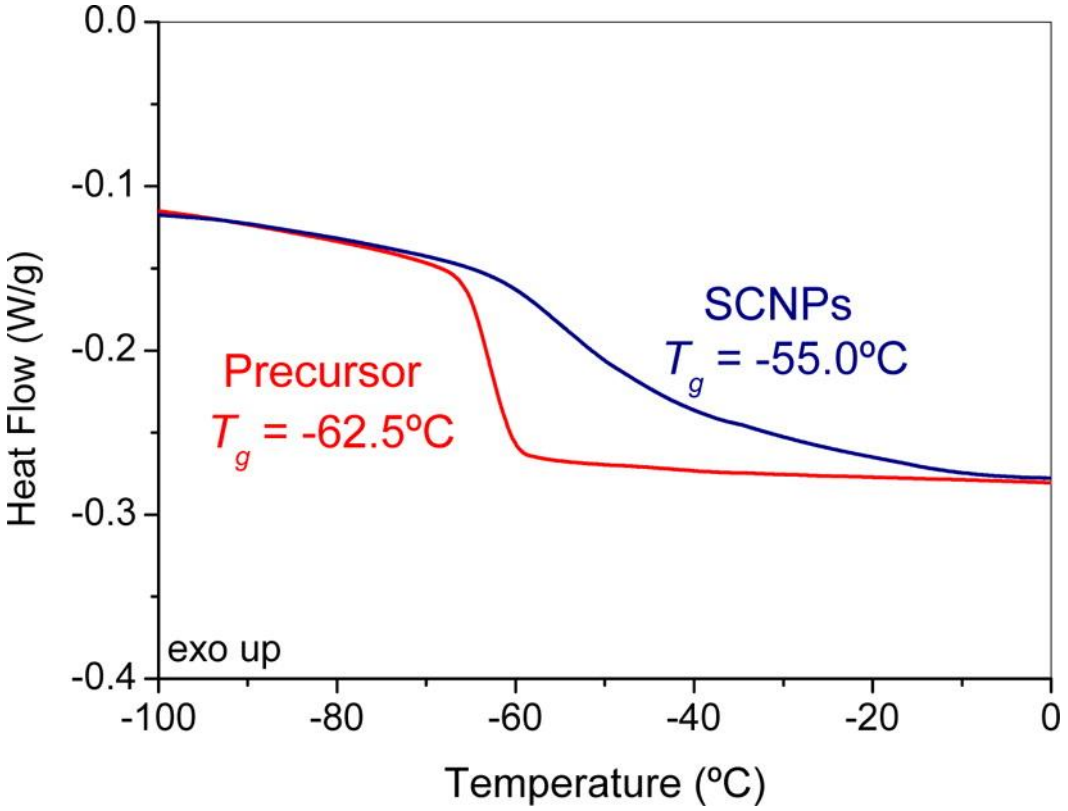

Figure 3.8. DSC traces corresponding to polyether SCNPs (blue trace) prepared from the terpolymer poly($THF_{0.77}$–$GPgE_{0.10}$–$GPE_{0.13}$) (red trace) via photoactivated TYC.

3.5. Conclusions

In this Chapter a useful synthetic strategy for the facile synthesis of polyether SCNPs is reported. Merging of zwitterionic ROP and photoactivated TYC allows the construction of polyether SCNPs from poly(THF–GPgE–GPE) terpolymers with high THF content *via* chain compaction, as revealed by a combination of techniques including SEC with triple detection, FTIR spectroscopy, ^{1}H NMR spectroscopy, TEM, and DSC. Conversely, SCNP formation was not observed from poly(THF–co–GPgE) copolymers under identical TYC conditions due to the different monomer sequence distribution in these copolymers when compared to that in the terpolymer. These monomer sequence distributions were elucidated by kinetic experiments *via* real–time ^{13}C NMR spectroscopy. During SEC experiments in THF at 30 °C, poly(THF–GPgE–GPE) terpolymers were found to behave as chains in a theta solvent (ν = 0.51), whereas the

polyether SCNPs showed more compact conformations under identical conditions (ν = 0.48 and ν = 0.43 for SCNPs prepared from poly($TH_{F0.77}$−$GPgE_{0.10}$−$GPE_{0.13}$) and poly($THF_{0.62}$−$GPgE_{0.18}$−$GPE_{0.20}$) terpolymers, respectively), far from the compact conformation expected for globular nano−objects (ν = 0.33). Upon solvent removal, the nanoparticles were observed as quasi−spherical nano−objects by TEM. Although intrachain cross−linking via TYC produces a significant increase in the glass transition temperature of the nanoparticles when compared to that of the precursor, the polyether SCNPs were found to be amorphous materials showing a glass transition temperature well below 0 °C.

3.6. References

[1] Gonzalez−Burgos, M.; Latorre−Sanchez, A.; Pomposo, J. A. Advances in single − chain technology. *Chemical Society Reviews*, **2015**, *44*, 6122−6142.

[2] Lyon, C. K.; Prasher, A.; Hanlon, A. M.; Tuten, B. T.; Tooley, C. A.; Frank, P. G.; Berda, E. B. A brief user's guide to single−chain nanoparticles. *Polymer Chemistry*, **2015**, *6*, 181−197.

[3] Sanchez−Sanchez, A.; Pomposo, J. A. Single−chain polymer nanoparticles via non−covalent and dynamic covalent bonds. *Particle & Particle Systems Characterization*, **2014**, *31*, 11−23.

[4] Sanchez−Sanchez, A.; Pérez−Baena, I.; Pomposo, J. A. Advances in click chemistry for single−chain nanoparticle construction. *Molecules*, **2013**, *18*, 3339−3355.

[5] Altintas, O.; Barner−Kowollik, C. Single−chain folding of synthetic polymers: a critical update. *Macromolecular Rapid Communications*, **2012**, *33*, 958−971.

[6] Aiertza, M.; Odriozola, I.; Cabañero, G.; Grande, H.−J.; Loinaz, I. Single−chain polymer nanoparticles. *Cellular and Molecular Life Sciences*, **2012**, *69*, 337−346.

[7] Müge, A.; Elisa, H.; Meijer, E. W.; Anja, R. A. P., Dynamic Single Chain Polymeric Nanoparticles: From Structure to Function. In Sequence−Controlled Polymers: Synthesis, Self−Assembly, and Properties. *ACS Symposium Series*, **2014**, 1170, 313−325.

[8] Mavila, S.; Eivgi, O.; Berkovich, I.; Lemcoff, N. G. Intramolecular cross−linking methodologies for the synthesis of polymer nanoparticles. *Chemical Reviews*, **2016**, *116*, 878−961.

[9] Wong, E. H. H.; Lam, S. J.; Nam, E.; Qiao, G. G. Biocompatibles single−chain polymeric nanoparticles via organo−catalyzed ring−opening polymerization. *ACS Macro Letters*, **2014**, *3*, 524−528.

[10] Willenbacher, J.; Wuest, K. N. R.; Mueller, J. O.; Kaupp, M.; Wagenknecht, H.−A.; Barner−Kowollik, C. Photochemical design of functional fluorescent single−chain nanoparticles. *ACS Macro Letters*, **2014**, *3*, 574−579.

[11] Chao, D.; Jia, X.; Tuten, B.; Wang, C.; Berda, E. B. Controlled folding of a novel electroactive polyolefin via multiple sequential orthogonal intra−chain interactions. *Chemical Communications*, **2013**, *49*, 4178−4180.

[12] Dirlam, P. T.; Kim, H. J.; Arrington, K. J.; Chung, W. J.; Sahoo, R.; Hill, L. J.; Costanzo, P. J.; Theato, P.; Char, K.; Pyun, J. Single chain polymer nanoparticles via sequential ATRP and oxidative polymerization. *Polymer Chemistry*, **2013**, *4*, 3765−3773.

[13] Li, G.; Tao, F.; Wang, L.; Li, Y.; Bai, R. A facile strategy for preparation of single−chain polymeric nanoparticles by intramolecular photo−crosslinking of azide polymers. *Polymer*, **2014**, *55*, 3696−3702.

[14] Zhu, B.; Sun, S.; Wang, Y.; Deng, S.; Qian, G.; Wang, M.; Hu, A. Preparation of carbon nanodots from single−chain polymeric nanoparticles and theoretical investigation of the photoluminescence mechanism. *Journal of Material Chemistry C*, **2013**, *1*, 580−586.

[15] Wang, P.; Pu, H.; Ge, J.; Jin, M.; Pan, H.; Chang, Z.; Wan, D. Fluorescence−labeled hydrophilic nanoparticles via single−chain folding. *Materials Letters*, **2014**, *132*, 102−105.

[16] Beck, J. B.; Killops, K. L.; Kang, T.; Sivanandan, K.; Bayles, A.; Mackay, M. E.; Wooley, K. L.; Hawker, C. J. Facile preparation of nanoparticles by intramolecular cross−linking of isocyanate functionalized copolymers. *Macromolecules*, **2009**, *42*, 5629−5635.

[17] Harth, E.; Horn, B. V.; Lee, V. Y.; Germack, D. S.; Gonzales, C. P.; Miller, R. D.; Hawker, C. J. A facile approach to architecturally defined nanoparticles via intramolecular chain collapse. *Journal of the American Chemical Society*, **2002**, *124*, 8653−8660.

[18] Murray, B. S.; Fulton, D. A. Dynamic covalent single−chain polymer nanoparticles. *Macromolecules*, **2011**, *44*, 7242−7252.

[19] Tuten, B. T.; Chao, D.; Lyon, C. K.; Berda, E. B. Single−chain polymer nanoaprticles via reversible disulfide bridges. *Polymer Chemistry*, **2012**, *3*, 3068−3071.

[20] Sanchez−Sanchez, A.; Fulton, D. A.; Pomposo, J. A. pH−responsive single−chain polymer nanoparticles utilizing dynamic covalent enamine bonds. *Chemical Communications*, **2014**, *50*, 1871−1874.

[21] Frank, P. G.; Tuten, B. T.; Prasher, A.; Chao, D.; Berda, E. B. Intra−chain photodimerization of pendant anthracene units as an efficient route to single−chain nanoparticle formation. *Macromolecular Rapid Communications*, **2014**, *35*, 249−253.

[22] Seo, M.; Beck, B. J.; Paulusse, J. M. J.; Hawker, C. J.; Kim, S. Y. Polymeric nanoparticles via noncovalent cross−linking of linear chains. *Macromolecules*, **2008**, *41*, 6413−6418.

[23] Foster, E. J.; Berda, E. B.; Meijer, E. W. Metaaestable supramolecular polymer nanoparticles via intramolecular collapse of single polymer chains. *Journal of the American Chemical Society*, **2009**, *131*, 6964−6966.

[24] Terashima, T.; Mes, T.; De Greef, T. F. A.; Gillissen, M. A. J.; Besenius, P.; Palmans, A. R. A.; Meijer, E. W. Single−chain folding of polymers for catalytic systems in water. *Journal of the American Chemical Society*, **2011**, *133*, 4742−4745.

[25] Gillissen, M. A. J.; Voets, I. K.; Meijer, E. W.; Palmans, A. R. A. Single chain polymeric nanoparticles as compartmentalized sensors for metal ions. *Polymer Chemistry*, **2012**, *3*, 3166−3174.

[26] Appel, E. A.; Dyson, J.; del Barrio, J.; Walsh, Z.; Scherman, O. A. Formation of single−chain polymer nanoparticles in water through host−guest interactions. *Angewandte Chemie International Edition*, **2012**, *51*, 4185−4189.

[27] Willenbacher, J.; Altintas, O.; Trouillet, V.; Knofel, N.; Monteiro, M. J.; Roesky, P. W.; Barner−Kowollik, C. Pd−complex driven formation of single−chain nanoparticles, *Polymer Chemistry*, **2015**, *6*, 4358−4365.

[28] Terashima, T.; Sugita, T.; Fukae, K.; Sawamoto, M. Synthesis and single−chain folding of amphiphilic random copolymers in water. *Macromolecules*, **2014**, *47*, 589−600.

[29] Wang, F.; Pu, H.; Jin, M.; Pan, H.; Chang, Z.; Wan, D.; Du, J. From single−chain folding to polymer nanoparticles via intramolecular quadruple hydrogen−bonding interaction. *Journal of Polymer Science, Part A: Polymer Chemistry*, **2015**, *53*, 1832−1840.

[30] Matyjaszewski, K.; Xia, J. Atom transfer radical polymerization. *Chemical Reviews*, **2001**, *101*, 2921−2990.

[31] Hawker, C. J.; Bosman, A. W.; Harth, E. New polymer synthesis by nitroxide mediated living radical polymerizations. *Chemical Reviews*, **2001**, *101*, 3661−3688.

[32] Moad, G.; Rizzardo, E.; Thang, S. H. Living radical polymerization by the RAFT process. *Australian Journal of Chemistry*, **2005**, *58*, 379−410.

[33] de Luzuriaga, A. R.; Ormategui, N.; Grande, H. J.; Odriozola, I.; Pomposo, J. A.; Loinaz, I. Intramolecular click cycloaddition: an efficient room−temperature route towards bioconjugable polymeric nanoparticles. *Macromolecular Rapid Communications*, **2008**, *29*, 1156−1160.

[34] Günay, K. A.; Theato, P.; Klok, H.−A. History of post−polymerization modification in functional polymers by post−polymerization modification, Wiley, **2012**.

[35] Pomposo, J. A., Polymers: single−chain polymer nanoparticles. *CRC Concise Encyclopedia of Nanotechnology*, **2015**.

[36] Van Renterghem, L. M.; Goethals, E. J.; Du Prez, F. E. Star−shaped poly(tetrahydrofuran) with reactive end groups: design, MALDI−TOF study and solution behavior. *Macromolecules*, **2005**, *39*, 528−534.

[37] Oike, H.; Mouri, T.; Tezuka, Y. Efficient polymer cyclization by electrostatic self−assembly and covalent fixation with telechelic poly(tetrahydrofuran) having cyclic ammonium salt groups. *Macromolecules*, **2001**, *34*, 6592−6600.

[38] Sugai, N.; Heguri, H.; Ohta, K.; Meng, Q.; Yamamoto, T.; Tezuka, Y. Effective click construction of bridged− and spiro−multicyclic polymer topologies with tailored cyclic prepolymers (kyklo−telechelics). *Journal of the American Chemical Society* **2010**, *132*, 14790−14802.

[39] Beck, J. B.; Ineman, J. M.; Rowan, S. J. Metal/ligand−induced formation of metallo−supramolecular polymers. *Macromolecules*, **2005**, *38*, 5060−5068.

[40] Sivakova, S.; Bohnsack, D. A.; Mackay, M. E.; Suwanmala, P.; Rowan, S. Utilization of a combination of weak hydrogen−bonding interactions and phase segregation to yield highly thermosensitive supramolecular polymers. *Journal of the American Chemical Society*, **2005**, *127*, 18202−18211.

[41] Odian, G., Principles of Polymerization. 4th edition, Wiley, **2004**.

[42] Klein, R.; Wurm, F. R. Aliphatic polyethers: Classical polymers for the 21st Century. *Macromolecular Rapid Communications*, **2015**, *36*, 1147−1165.

[43] Brocas, A.−L.; Mantzaridis, C.; Tunc, D.; Carlotti, S. Polyether synthesis: from activated or metal−free anionic ring−opening polymerization of epoxides to functionalization. *Progress in Polymer Science*, **2013**, *38*, 845−873.

[44] Schull, C.; Gieshoff, T.; Frey, H. One−step synthesis of multi−alkyne functional hyperbranched polyglycerols by copolymerization of glycidyl propargyl ether and glycidol. *Polymer Chemistry*, **2013**, *4*, 4730−4736.

[45] Bhowmick, A. K.; Stephens, H. Handbook of Elastomers, *CRC Press*, **2000**.

[46] Pruckmayr, G.; Dreyfuss, P.; Dreyfuss, M. P., Polyethers, Tetrahydrofuran and Oxetane Polymers. *Kirk−Othmer Encyclopedia of Chemical Technology, John Wiley & Sons*, **2000**.

[47] Basko, M.; Bednarek, M.; Billiet, L.; Kubisa, P.; Goethals, E.; Du Prez, F. Combining cationic ring−opening polymerization and click chemistry for the design of functionalized polyurethanes. *Journal of Polymer Science, Part A: Polymer Chemistry*, **2011**, *49*, 1597−1604.

[48] Asenjo−Sanz, I.; Veloso, A.; Miranda, J. I.; Alegría, A.; Pomposo, J. A.; Barroso−Bujans, F. Zwitterionic ring−opening copolymerization of tetrahydrofuran and glycidyl plenyl ether with $B(C_6F_5)_3$. *Macromolecules*, **2015**, *48*, 1664−1672.

[49] Koo, S. P. S.; Stamenović, M. M.; Prasath, R. A.; Inglis, A. J.; Du Prez, F. E.; Barner−Kowollik, C.; Van Camp, W.; Junkers, T. Limitations of radical thiol−ene reactions for polymer−polymer conjugation. *Journal of Polymer Science, Part A: Polymer Chemistry*, **2010**, *48*, 1699−1713.

[50] Derboven, P.; D'hooge, D. R.; Stamenovic, M. M.; Espeel, P.; Marin, G. B.; Du Prez, F. E.; Reyniers, M.−F. Kinetic modeling of radical thiol−ene chemistry for macromolecular design: importance of side reactions and diffusional limitations. *Macromolecules*, **2013**, *46*, 1732−1742.

[51] Han, J.; Zhao, B.; Gao, Y.; Tang, A.; Gao, C. Sequantial click synthesis of hyperbranched polymers via the A2 + CB2 approach. Polymer Chemistry, **2011**, *2*, 2175−2178.

[52] Han, J.; Zhao, B.; Tang, A.; Gao, Y.; Gao, C. Fast and scalable production of hyperbranched polythioether−ynes by a combination of thiol−halogen click−like coupling and thiol−yne click polymerization. *Polymer Chemistry*, **2012**, *3*, 1918−1925.

[53] Han, J.; Zheng, Y.; Zhao, B.; Li, S.; Zhang, Y.; Gao, C. Sequentially hetero−functional, topological polymers by step−growth thiol−yne approach. *Scientific Reports*, **2014**, *4*, 4387.

[54] Lowe, A. B.; Hoyle, C. E.; Bowman, C. N. Thiol−yne click chemistry: a powerful and versatile methodology for materials synthesis. *Journal of Materials Chemistry*, **2010**, *20*, 4745−4750.

[55] Hoyle, C. E.; Lowe, A. B.; Bowman, C. N. Thiol−click chemistry: a multifaceted toolbox for small molecule and polymer synthesis. *Chemical Society Reviews*, **2010**, *39*, 1355−1387.

[56] Schmidt, B. V. K. J.; Fechler, N.; Falkenhagen, J.; Lutz, J.−F. Controlled folding of synthetic polymer chains through the formation of positionable covalent bridges. *Nature Chemistry*, **2011**, *3*, 234−238.

[57] Ouchi, M.; Badi, N.; Lutz, J.−F.; Sawamoto, M. Single−chain technology using discrete synthetic macromolecules. *Nature Chemistry*, **2011**, *3*, 917−924.

[58] Lutz, J.−F.; Ouchi, M.; Liu, D. R.; Sawamoto, M. Sequence−controlled polymers. *Science*, **2013**, *341*, 1238149.

[59] Obermeier, B.; Wurm, F.; Frey, H. Amino functional poly(ethylene glycol) copolymers via protected amino glycidol. *Macromolecules*, **2010**, *43*, 2244−2251.

[60] Alkan, A.; Natalello, A.; Wagner, M.; Frey, H.; Wurm, F. R. Ferrocene−containing multifunctional polyethers: monomer sequence monitoring via quantitative ^{13}C NMR spectroscopy in bulk. *Macromolecules*, **2014**, *47*, 2242−2249.

[61] Natalello, A.; Alkan, A.; von Tiedemann, P.; Wurm, F. R.; Frey, H. Enlarging the toolbox: epoxide termination of polyferrocenylsilane (PFS) as a key step for the synthesis of amphiphilic PFS−polyether block copolymers. *ACS Macro Letters*, **2014**, *3*, 560−564.

[62] Natalello, A.; Werre, M.; Alkan, A.; Frey, H. Monomer sequence distribution monitoring in living carbanionic copolymerization by real−time ^{1}H NMR spectroscopy. *Macromolecules*, **2013**, *46*, 8467−8471.

[63] Ibbett, R. N. NMR Spectroscopy of polymers. *Springer*, **2012**.

[64] Zaremski, M. Y.; Kalugin, D. I.; Golubev, V. B. Gradient copolymers: synthesis, structure and properties. *Polymer Science Series A*, **2009**, *51*, 103−122.

[65] Pomposo, J. A.; Perez−Baena, I.; Lo Verso, F.; Moreno, A. J.; Arbe, A.; Colmenero, J. How far are single−chain nanoparticles in solution from the globular state? *ACS Macro Letters*, **2014**, *3*, 767−772.

CHAPTER 4

Synthesis of Single-Ring Nanoparticles Mimicking Natural Cyclotides

4.1. Introduction

Cyclotides are cyclized peptides stabilized by intra-ring disulfide bonds, typically composed of only 30-40 amino acids [1]. Peptides containing a cyclic backbone are ubiquitous in nature and are found in bacteria, fungi and plants as well as animals [2]. Generally, N- to C-terminally cyclized peptides display enhanced stability against enzymatic degradation by proteases, as well as a variety of biological activities including cytotoxicity or antimicrobial, insecticidal and hemolytic activity [3]. Some cyclotides are able to cross human cell membranes [4, 5] and are able to target protein-protein interactions efficiently in animal models [6].

Due to their small size and pharmaceutical potential, many native and engineered cyclotides have recently been synthesized by chemical methods using solid-phase peptide synthesis techniques combined with intramolecular native chemical ligation methods [7, 8]. Similarly, some specific multi-cyclic polymer constructions have been reported by employing nonlinear telechelic precursors having reactive groups at predefined positions [9-11]. However, mimicking the compact, hierarchical (multi-ring) structure found in naturally occurring cyclotides with simple synthetic polymers remains highly challenging.

Several strategies have been explored trying to mimic (at a fundamental level) the folding of a natural non-cyclized polypeptide to its native, functional conformation as observed e.g. in enzymes [12-15]. Among them, the formation of single-chain nanoparticles (SCNPs) via intra-chain cross-linking at high dilution to promote chain collapse in synthetic precursor polymers has shown to be one such promising approach [16-27]. It is worth noting that polymer folding from synthetic polymer precursors

proceeds via the random linking of the reactive pendant units along the polymer precursor chain, and hence the product inevitably entails structural heterogeneity.

As mentioned in Chapter 1, SCNPs are currently attracting significant interest for nanomedicine [28-32] and biomimetic catalysis applications [33-41]. However, conventional SCNPs synthesized from simple linear synthetic precursor polymers often display a sparse, non-globular conformation in solution, as revealed by neutron scattering experiments and molecular dynamics (MD) simulations [42]. We hypothesized that similar to the case of cyclotides, a higher compaction degree would be obtained by starting from cyclic synthetic polymers instead of linear ones. In particular, cyclization is expected to enhance intra-chain cross-linking between distant functional groups during collapse, hence, leading to an improved overall compaction degree. Interestingly, such an expectation is supported by very recent MD simulations by Formanek and Moreno [43].

4.2. Objectives

The aim of this project is to synthesize single-ring nanoparticles (SRNPs) as a new class of natural cyclotide mimetics at high dilution starting from simple synthetic precursor polymers.

Although we attempted several synthetic routes prior to obtaining a satisfactory outcome, in this Chapter I will focus on the one that gave us access to SRNPs: a three-step folding-activation-collapse process started with copolymers of styrene and chloromethylstyrene (Scheme 4.1).

The initial folding step will be carried out by a photoactivated hetero Diels-Alder (HDA) ring-closing reaction, which will trigger chain compaction of the individual precursor polymer chains. The subsequent activation step comprises a simple azidation procedure, whereas the final collapse step is driven by CuAAC in the presence of an external cross-linker, providing additional compaction to the final single-ring nanoparticles (SRNPs).

The unique structure and compaction degree of the SRNPs will be established via a detailed comparison with conventional single-chain nanoparticles (SCNPs) prepared exclusively by chain collapse from the exact same precursor polymer (without the prefolding step).

The obtained compounds will be characterized by different techniques, including size exclusion chromatography (SEC), ^{1}H NMR spectroscopy, Fourier transform infrared (FTIR) spectroscopy and UV/Vis spectroscopy.

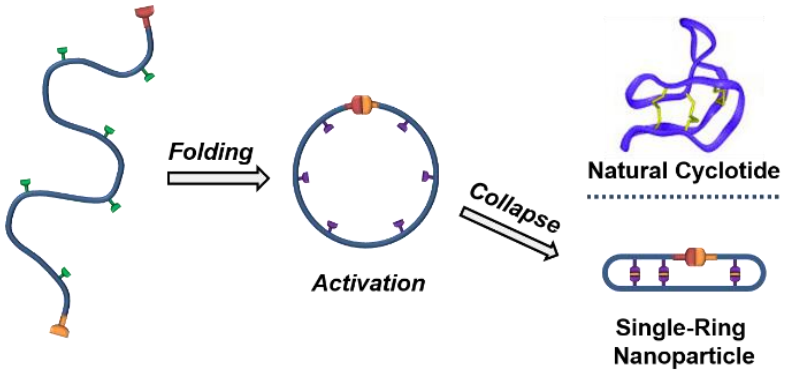

Scheme 4.1. Schematic illustration of the synthesis of poly(S-*r*-CMS) SRNPs mimicking natural cyclotides.

4.3. Experimental part

4.3.1. Materials

Styrene (≥ 99%) and 4-chloromethylstyrene (90%) were purchased from Sigma-Aldrich, passed through a column (≈ 3 cm) of neutral alumina and stored at 4ºC prior to use. Copper (I) bromide (98 %, Aldrich) was purified following the Keller and Wycoff method: it was washed five times with 20 mL of glacial acetic acid, then three times with 30 mL of absolute ethanol (≥ 99.8%, Aldrich) and finally six times with 15 mL of anhydrous ether. The product was dried at 80 °C in vacuum for 2 hours and stored in a glovebox with argon atmosphere. Methanol (reagent grade, Scharlab), hexane (99%, Aldrich), acetonitrile (ACS reagent, ≥ 99.5% , Aldrich), diglycolic acid (98%, Aldrich), propargylamine (98%, Aldrich), HBTU (≥ 99.0%, Aldrich), dichloromethane (anhydrous, ≥99.8%, Aldrich), sodium azide (ReagentPlus, ≥ 99.5%, Aldrich), N,N'-dimethylformamide (DMF) (anhydrous, ≥ 99.8%, Aldrich), L-ascorbic acid (crystalline, ≥ 99%, Aldrich), N,N,N',N´´,N´´-Pentamethyldiethylenetriamine (PMDETA) (99%, Aldrich), toluene (anhydrous, 99.8%, Aldrich) and tetrahydrofuran (anhydrous, Acros) were used as received.

4.3.2. Preparation of the Photoreactive RAFT Agent CEFB

The photoreactive RAFT agent 2-((4-Cyano-4-((phenylcarbonothioyl)thio)pentanoyl) oxy)Ethyl 4-((2-Formyl-3-methylphenoxy)methyl) Benzoate (CEFB) (Scheme 4.2) was synthesized following the procedure reported by Junkers et al. [44].

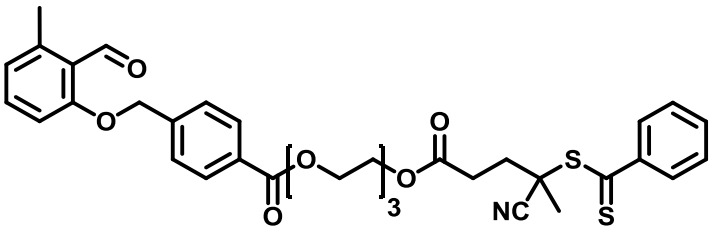

Scheme 4.2. Chemical structure of photoreactive RAFT agent CEFB.

4.3.3. Synthesis of the difunctional cross-linker 2,2'-oxybis(N-(prop-2-yn-1-yl)acetamide) (BPAM)

Diglycolic acid (400 mg, 2.96 mmol, 1.0 eq.), propargylamine (0.57 mL, 8.89 mmol, 3.0 eq.), HBTU (3.39 g, 8.93 mmol, 3.0 eq.) and N,N-Diisopropylethylamine (0.56 mL, 3.24 mmol, 1.1 eq.) were dissolved in 10 mL of dichloromethane and stirred under argon at ambient temperature for 24 h. All volatile compounds were removed under reduced pressure at 40 °C and the crude product was purified via column chromatography over SiO_2 (EtOAc/$CHCl_3$: 1/1 → EtOAc/$CHCl_3$/MeOH : 4.5/4.5/1, R_f = 0.05) yielding the product as a white solid (270 mg, 1.29 mmol, 44%, Scheme 4.3).

^{1}H NMR (600 MHz, DMSO-d_6) (Figure 4.1) δ = 8.47 (t, J = 5.8 Hz, 2H, c), 3.97 (s, 4H, d), 3.93 (dd, J = 5.8, 2.5 Hz, 4H, b), 3.12 (t, J = 2.5 Hz, 2H, a).

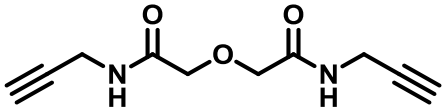

Scheme 4.3. Chemical structure of difunctional cross-linker BPAM.

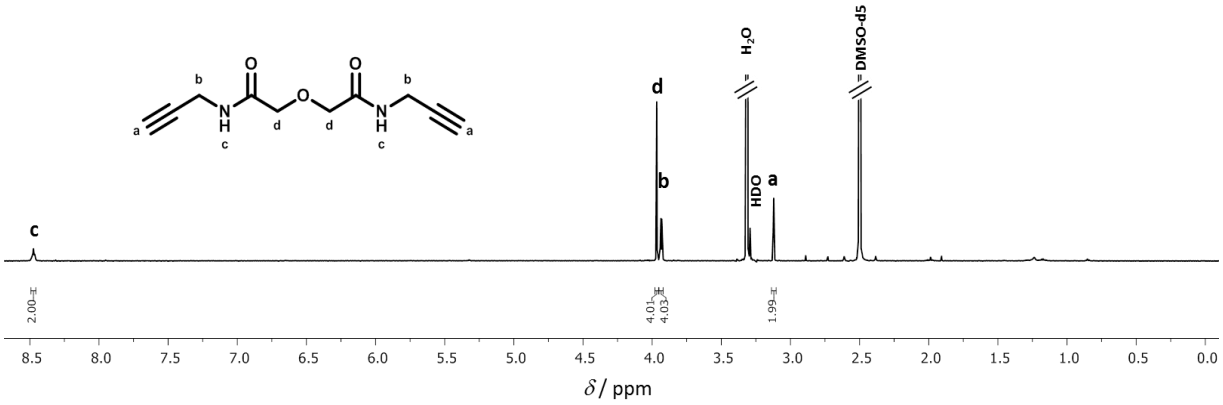

Figure 4.1. ^{1}H NMR spectrum of BPAM in DMSO-d_6.

4.3.4. Preparation of precursor polymer 1

Poly(styrene-r-chloromethylstyrene), poly(S-*r*-CMS) **1**, was synthesized via thermal polymerization without the involvement of an external radical initiator compound. In a typical procedure, styrene (3 mL, 26.1 mmol), 4-chloromethylstyrene (0.65 mL, 4.6 mmol) and CEFB (23 mg, 0.1 mmol) were mixed in a 25 mL rounded bottom flask covered with aluminium foil and equipped with a septum cap. The mixture was purged with argon for 20 minutes and stirred for 2 h at 110 ^{0}C in a silicon bath. The resulting crude product was precipitated three times in cold hexane, yielding a pink powder (**1**, 295 mg, 9 % yield, M_n = 6.7 kDa, Đ = 1.05, CMS content = 41 mol %). The presence of the photoreactive RAFT agent in polymer **1** was confirmed by ^{1}H-NMR spectroscopy (see Figure 4.2).

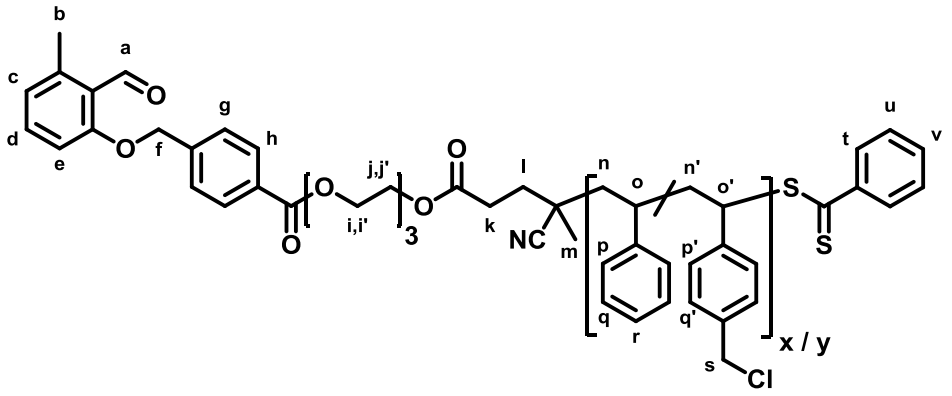

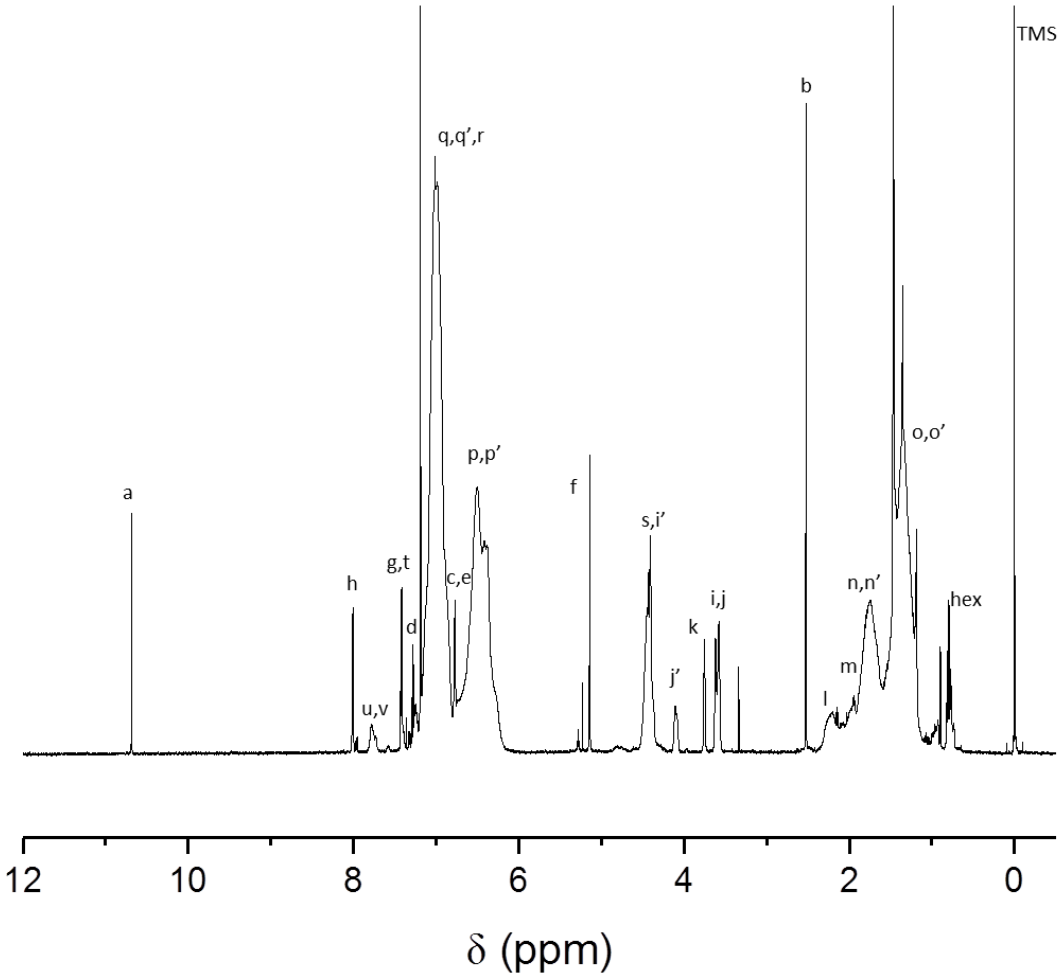

Figure 4.2. ^{1}H NMR spectrum of precursor polymer **1** in $CDCl_3$.

4.3.5. Preparation of cyclic polymer 2 – ("Folding" Step I)

In a typical synthesis of cyclic polymer **2** (Scheme 4.4), 10 mg of **1** were dissolved in 500 mL of a mixture of degassed acetonitrile/dichloromethane (2:1) in a rounded bottom flask with septum cap. After purging the system with argon for 1 hour, it was introduced in a photoreactor equipped with 6 UV-lamps (λ_{max} = 320 nm) and it was left reacting for 2 hours. The solvent mixture was evaporated at reduced pressure and the product was precipitated in cold methanol and dried at 60 ^{0}C in a vacuum oven. The

cyclic polymer **2** was obtained as a white powder (9.4 mg, 94% yield, M_n = 5.8 kDa, $Đ$ = 1.08).

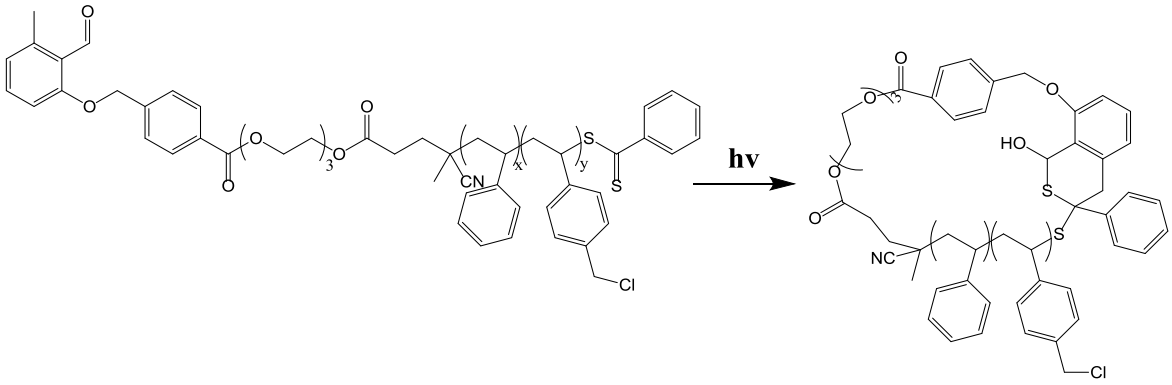

Scheme 4.4. Schematic illustration of the Folding step I.

4.3.6. Preparation of activated cyclic polymer 3 – ("Activation" Step II)

Azidation of **2** was performed by dissolving 30 mg of **2** and 9.5 mg of sodium azide (0.15 mmol, 2 eq.) in DMF (1.2 mL) in a 6 mL vial. The mixture was left stirring at room temperature for 24 h. The crude product was precipitated in a mixture of H_2O/methanol (1:1), yielding the activated product **3** as a white powder (26 mg, 87% yield, M_n = 5.8 kDa, $Đ$ = 1.08).

For the synthesis of conventional single-chain nanoparticles (SCNPs) as a reference material, the same procedure was followed to synthesize the activated product **1´** starting directly from **1**.

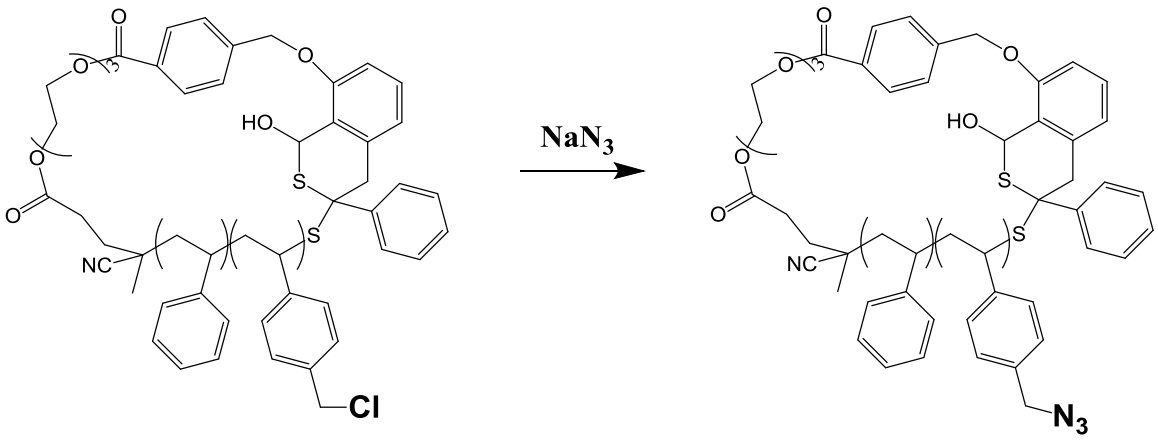

Scheme 4.4. Schematic illustration of the Activation step II.

4.3.7. Synthesis of Single-Ring Nanoparticles 4 – ("Collapse" Step III)

Single-ring nanoparticles (SRNPs) **4** (Scheme 4.5) were synthesized from the activated cyclic polymer **3** via CuAAC click chemistry-induced collapse. In a typical procedure, **3** (10 mg), **BPAM** (3.5 mg, 1.3 N_3 eq.), CuBr (1.8 mg, 0.5 N_3 eq.), L-ascorbic acid (2.2 mg, 0.5 N_3 eq.) and PMDETA (2.7 μL, 0.5 N_3 eq.) were dissolved in 20 mL of a mixture of DMF and toluene (1:1) in a 100 mL rounded bottom flask. The mixture was purged with argon for 1 hour and it was left under stirring at 80 ^{0}C in an oil bath for 48 hours. The catalysts were removed by extraction with a saturated solution of ammonium chloride. The organic phase was dried with magnesium sulfate. After evaporating the solvents at reduced pressure, SRNPs **4** were precipitated twice in cold methanol (3.2 mg, M_n = 4.8 kDa, $Đ$ = 1.25).

Conventional SCNPs **5** were synthesized from **1´** following the same procedure (3.7 mg, M_n = 6.9 kDa, $Đ$ = 1.23).

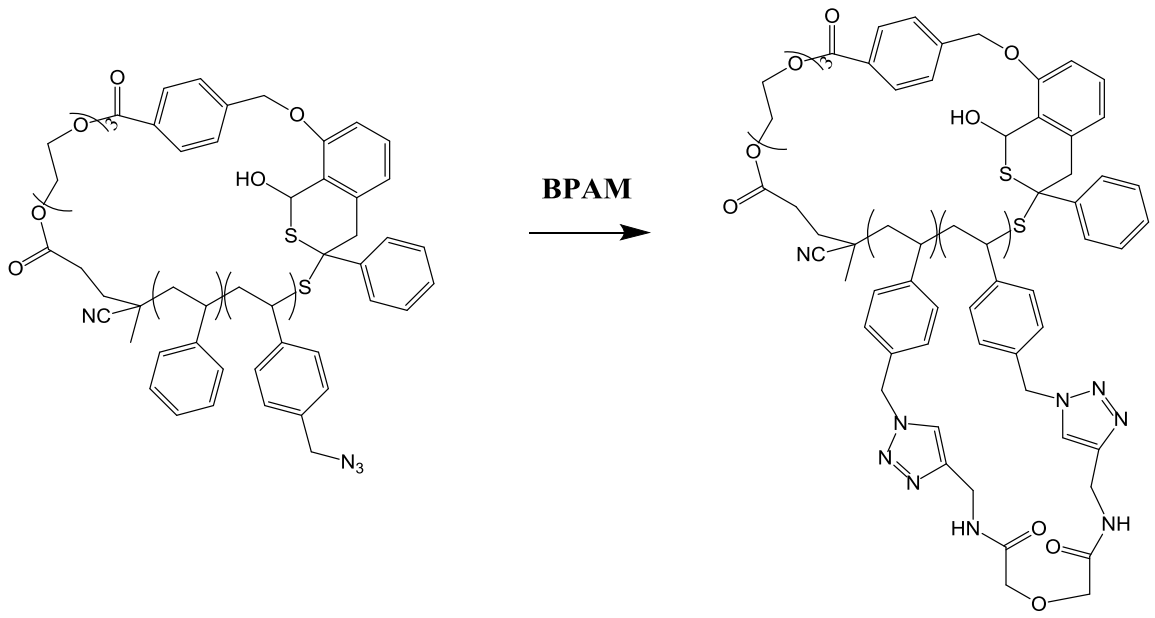

Scheme 4.5. Schematic illustration of the Collapse step III.

4.4. Results and discussion

4.4.1. Synthetic access to Single-Ring Nanoparticles

As precursor polymer of SRNPs, copolymer **1** (Figure 4.2) was synthesized by means of reversible addition fragmentation chain transfer (RAFT) polymerization in bulk at 110 °C using ((4-cyano-4-((phenylcarbonothioyl)thio)pentanoyl)oxy)ethyl4-((2-formyl-3-methylphenoxy)methyl)benzoate (CEFB) as a difunctional photoreactive chain transfer agent. RAFT polymerization was used to install the two functionalities, i.e. an *α*-methylbenzaldehyde and a dithioester function, within one photoreactive RAFT agent as chain-ends in copolymer **1**.

Poly(styrene-*random*-chloromethylstyrene), poly(S-*r*-CMS), copolymers were targeted with variable number weight-average molecular weight (M_n = 4.5 – 6.7 kDa), CMS

contents (*y*) and narrow molecular weight distributions ($Đ$ = 1.05 – 1.08). In the following, we show the results obtained for a representative P(S-*r*-CMS) copolymer containing ≈ 55 monomers per chain (**1**: M_n=6.7 kDa, y=41% and $Đ$=1.05).

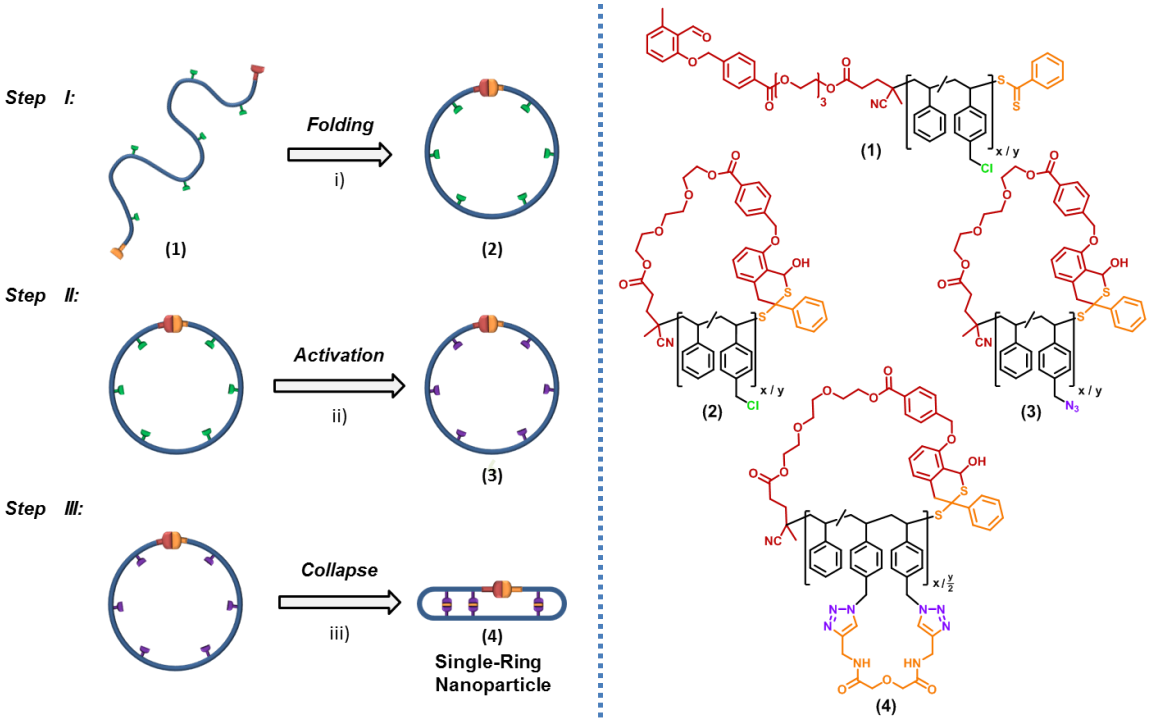

Scheme 4.3. Schematic illustration of the synthetic route towards single-ring nanoparticles (SRNPs) as cyclotide mimetics by a stepwise folding-activation-collapse process.

Ring-closing of **1** ("folding" step I in Scheme 4.3) was carried out via a photo-induced hetero Diels-Alder (HDA) reaction [45] at room temperature and high dilution (0.02 mg mL^{-1}) in a mixture of acetonitrile and dichloromethane (v/v=2/1). UV irradiation at λ_{max} = 350 nm for 2 h induced the rearrangement of the *α*-methylbenzaldehyde end-groups of **1** to active *ortho*-quinodimethanes that react under high dilution with the corresponding dithioester end-groups via an intramolecular HDA cycloaddition.

The success of the photoinduced ligation was confirmed by ^{1}H-NMR, UV/Vis spectroscopy and SEC. Upon ring-closure, complete disappearance of the ^{1}H-NMR

resonances associated with the α-methylbenzaldehyde end-group of **1** (**a**, **b** and **c** in Figure 4.3A) and the appearance of a new resonance centered at ca. 5.2 ppm, attributed to proton **a´** in the HDA cycloadduct (Figure 4.3B), were observed. In addition, the UV-vis spectrum of **2** was found to lack the intense peak associated with the characteristic π-π* transition of the thiocarbonyl moiety, indicating the successful formation of the HDA cycloadduct [45] (Figure 4.3C).

Quantification of the intramolecular ring-closing reaction was carried out by size exclusion chromatography (SEC), which is highly sensitive to the presence of impurities of high molecular weight arising from intermolecular coupling reactions [46].

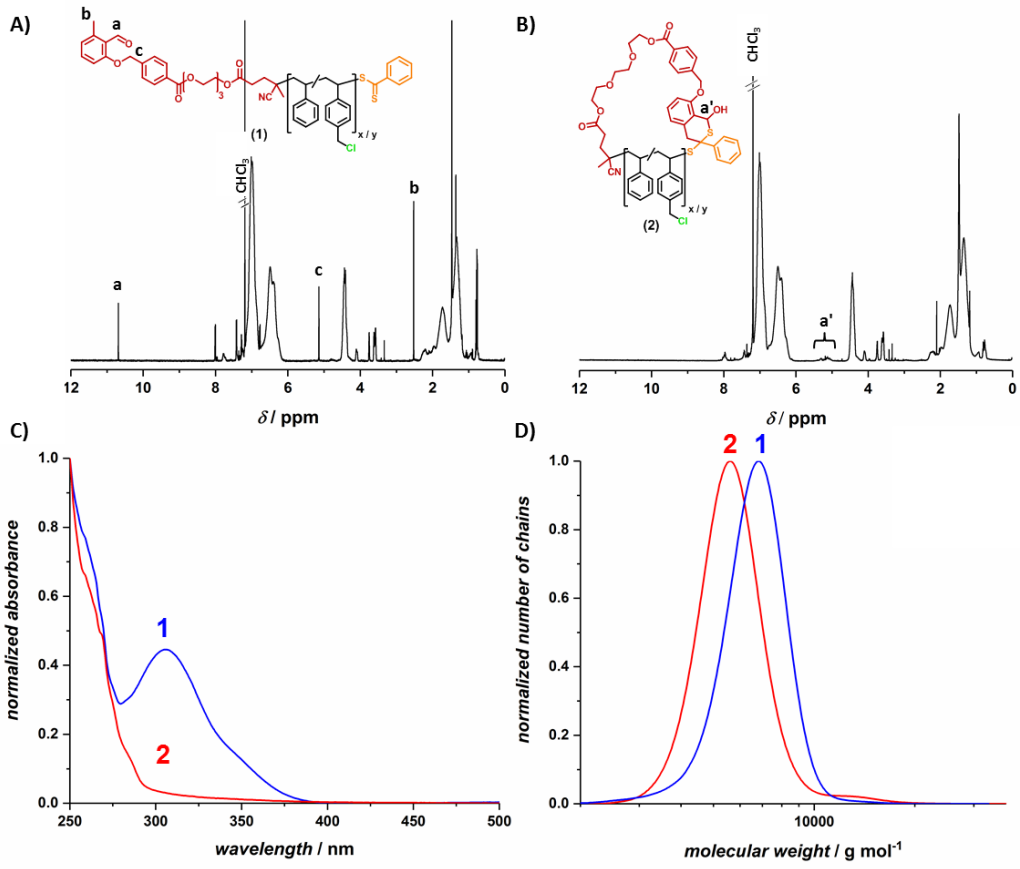

Figure 4.3. A) ^{1}H NMR resonances (**a**, **b**, **c**; δ = 10.7, 2.5 and 5.1 ppm) associated with the α-methylbenzaldehyde end-group of the linear precursor polymer **1**. **B)** ^{1}H NMR spectrum of **2** indicating the disappearance of the α-methylbenzaldehyde signals and the

appearance of a new resonance (**a´**, δ = 5.2 ppm) associated to the hetero Diels-Alder (HDA) cycloadduct. **C)** UV/Vis spectrum of **1** and **2** assessing the disappearance of the characteristic π-π* transition band of the thiocarbonyl moiety. **D)** Folding of **1** is accompanied by chain compaction as observed by a significant increase in SEC elution volume (number distribution shown). Note the presence of a very small amount of impurities at high molecular weight in the raw sample arising from secondary intermolecular coupling reactions.

As expected, folding of the linear synthetic precursor polymer via ring-closure was accompanied by significant chain compaction as observed by an increase in SEC elution volume decreasing the apparent peak molecular weight (M_P^{app}) 7.1 kDa to 5.8 kDa (refer to Figure 4.3D).

Functionalization of **2** (i.e. "activation" step II in Scheme 4.3) was carried out by nucleophilic substitution of the chloride groups in the CMS moieties with sodium azide, yielding **3**, which is active towards copper (I)-catalyzed azide-alkyne cycloaddition (CuAAC) reactions [47, 48]. The success of this reaction was confirmed by ^{1}H-NMR and infrared (IR) spectroscopy (see Figure 4.4). Upon azidation of **2**, the ^{1}H-NMR signal associated to the methylene protons **d** shifted from 4.4 ppm to 4.1 ppm (see Figure 4.4A,B), whereas a new intense vibration band centered at ν = 2095 cm^{-1} was observed in the IR spectrum of **3** (Figure 4.4C) corresponding to stretching vibrations of the azide moiety. In this case, a precise quantification of the reaction yield by ^{1}H-NMR spectroscopy was not possible due to a significant resonance overlap with methylene protons of –O–CH_2– moieties, although a visual comparison of Figure 4.4A and B suggests a high degree of azidation.

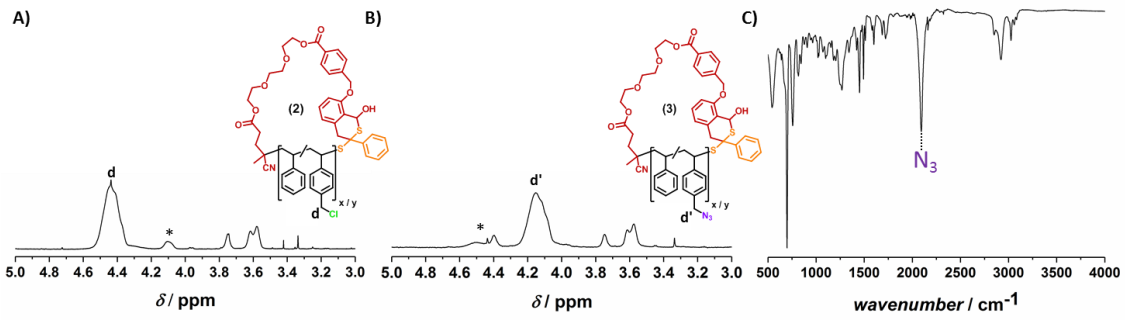

Figure 4.4. A) ^{1}H NMR signal **d** associated to methylene protons in the chloromethyl moieties of **2**. **B)** Upon azidation of **2** ("activation" step II), a shift of resonance **d** centered at 4.4 ppm to 4.1 ppm occurs. **C)** IR spectrum of **3** showing the characteristic band associated to stretching vibrations of the azide moiety.

The final compaction step III to afford SRNPs from **3** was driven by copper (I)-catalyzed azide-alkyne cycloaddition (CuAAC) [47, 48] in the presence of 2,2'-oxybis(N-(prop-2-yn-1-yl)acetamide) (BPAM) as external difunctional cross-linker. The success of the collapse reaction was assessed by ^{1}H-NMR spectroscopy and IR spectroscopy (Figure 4.5).

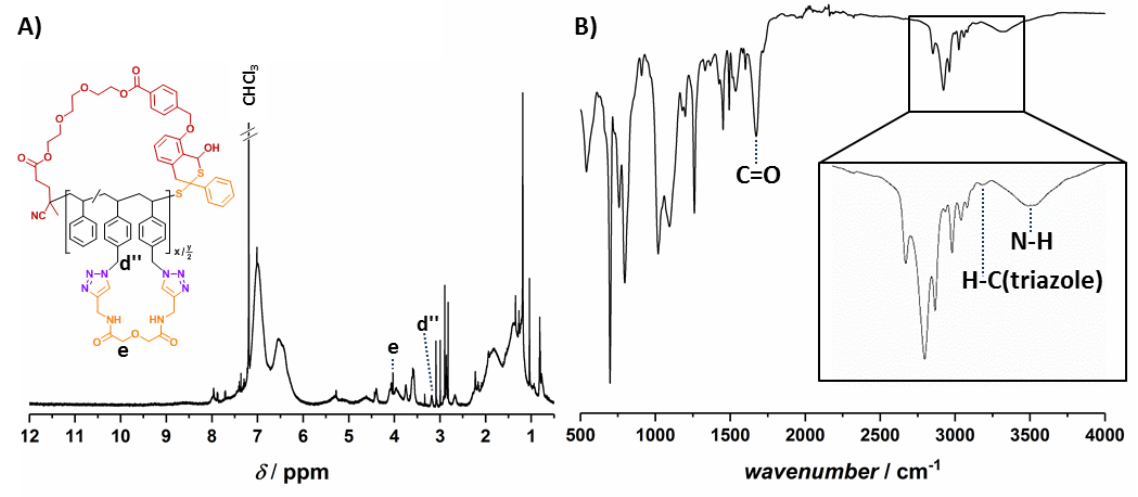

Figure 4.5. A) Characteristic ^{1}H NMR resonances (**d´´**, **e**) from single-ring nanoparticles, SRNPs **4**, prepared from **3**. **B)** IR spectrum of SRNPs 4 showing characteristic vibration bands corresponding to the carbonyl and amine groups (-C=O, =N-H) of the cross-linker moieties and C-H groups of the triazole rings formed upon intrachain CuAAC reaction (~3139 cm^{-1}).

Upon CuAAC reaction, a shift of the ^{1}H-NMR signal associated with the methylene protons **d´** was observed from 4.1 ppm to ≈ 3.9 ppm. In addition, a new resonance centered at 3.2 ppm appeared in the ^{1}H-NMR spectrum that we attribute to the methylene protons **e** protons within the cross-linker moiety. Complementary, the IR spectrum of SRNPs **4** (Figure 3B) shows characteristic vibrational bands from carbonyl and amine groups of the cross-linker moieties, the total absence of the characteristic azide band (~2095 cm^{-1}) and a new IR vibration band (~3139 cm^{-1}) arising from -C-H groups of the triazole rings formed upon intrachain CuAAC reaction [49].

4.4.2. Impact of the cyclic precursor structure on the single-chain collapse

SEC was employed to determine the compaction degree of the final SRNPs **4** as well as to quantify the selectivity of the intramolecular ring formation and single-chain collapse [50, 51]. As a measure of the compaction degree, we exploit the shrinking factor defined as $\langle G \rangle = M_P^{app}/M_P$, where M_P^{app} is the SEC peak molecular weight after compaction and M_P is the SEC peak molecular weight before compaction. The photochemical cyclization of **1** to **2** led to a shrinking factor of $\langle G \rangle_{\mathbf{1\text{-}2}}$ = 5.8 kDa / 7.1 kDa = 0.82 (Figure 4.3D) and a high selectivity for the intramolecular reaction, which is in excellent agreement with previously reported data [52, 53].

After the substitution of the chloride moieties with sodium azide, no significant change in the SEC chromatogram was observed between **2** and **3**. Conversely, collapse to SRNPs **4** gave $\langle G \rangle_{\mathbf{2\text{-}4}}$ = 4.3 kDa / 5.8 kDa = 0.74. The overall shrinking factor from **1** to SRNPs **4** was found to be $\langle G \rangle_{\mathbf{1\text{-}4}}$ = 0.61 (Figure 4.6B). For comparison, synthesis of conventional SCNPs **5** from **1** without involving the folding step, yet applying identical reaction conditions as for the collapse of the cyclic precursor **4** (Figure 4.6A), provided

with an overall shrinking factor $\langle G \rangle_{1\text{-}5}$ = 6.2 kDa / 7.1 kDa = 0.87 (Figure 4.6C). The rather different overall shrinking factor of SRNPs compared to SCNPs is thus an indication of the unique structure and compaction degree of SRNPs as cyclotide mimetics. While the collapse reaction occurs unselectively between the azide groups along the polymer chain, the initial cyclization is limited to the chain ends of the polymer.

Consequently, the CuAAC reaction can occur between groups which are prealigned within the polymer coil in solution, leading to a limited compaction, while the initial cyclization affords a distinct rearrangement of the chain, resulting in a larger degree of compaction upon cyclization and final collapse. As evident in Figure 4.6B and C, the final collapse leads to some limited intermolecular crosslinking for both SRNPs **4** and SCNPs **5** (approximately 15% of chains).

Whether the intermolecular impurities present were due to the use of the CuAAC reaction during the collapse step or due to the chain stiffness of the synthetic precursor polymer employed remains, however, to be elucidated with other combinations of precursor polymer and collapse chemistry.

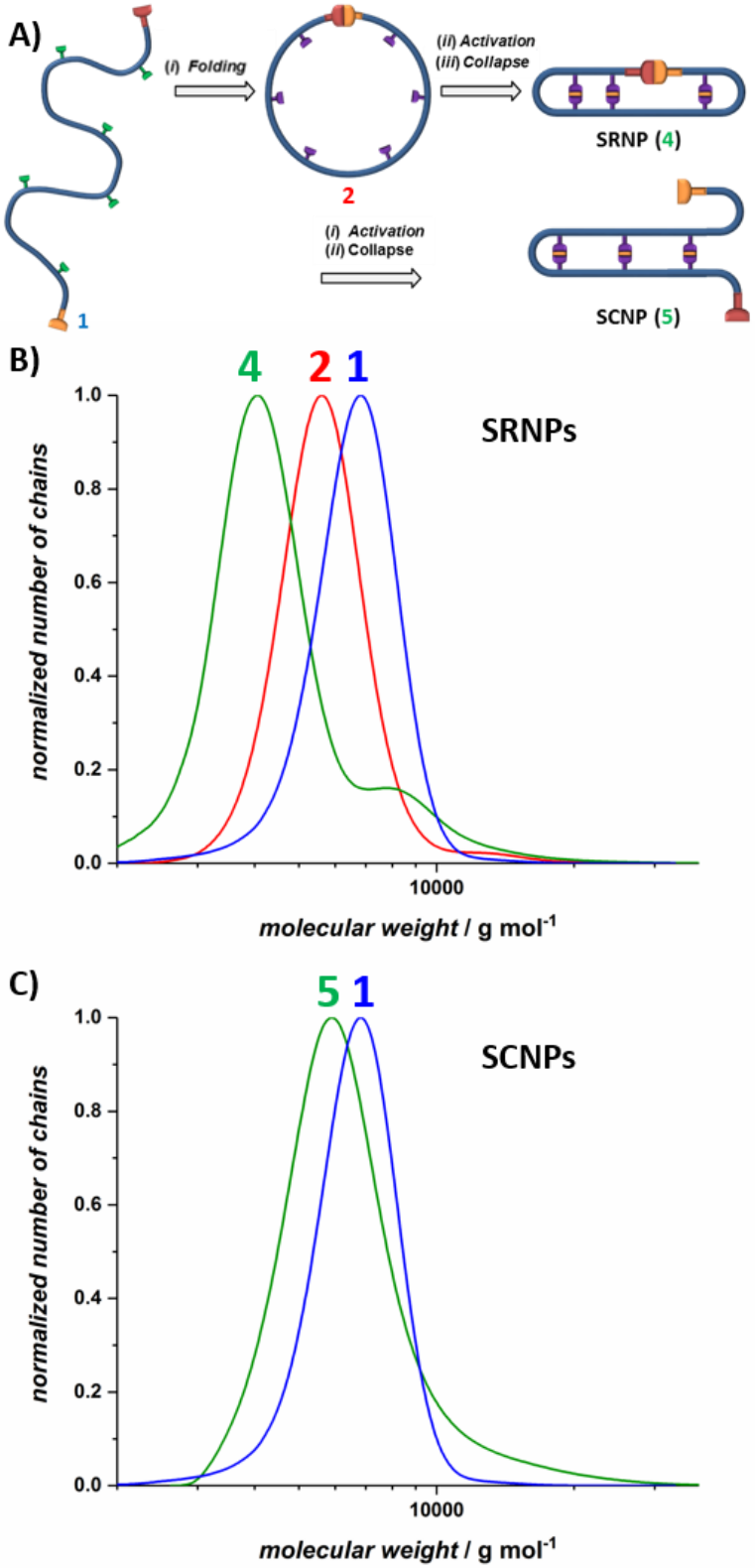

Figure 4.6. A) SEC chromatograms showing the number distribution corresponding to the formation of SRNPs **4** from **1** *via* the stepwise folding-activation-collapse process. B) SEC chromatograms of the synthesis of conventional SCNPs **5** from **1** without involving the folding step I in Scheme 1.

4.5. Conclusions

In this Chapter a class of natural cyclotide mimicking single-ring nanoparticle was introduced based on a stepwise folding-activation-collapse process at high dilution, starting from functional synthetic precursor polymers, prepared by RAFT polymerization in the presence of a difunctional photoreactive chain transfer agent.

The initial folding step was carried out by means of a photoactivated hetero Diels-Alder (HDA) ring-closing reaction with excellent selectivity towards the intramolecular pathway. As subsequent activation step, a simple but highly efficient azidation procedure was employed to render the precursor polymer active towards click chemistry procedures. The final collapse step leading to SRNP formation was driven by the CuAAC reaction in the presence of an external dialkyne cross-linker compound.

The unique structure and compaction degree of the SRNPs as cyclotide mimetics was revealed by their significantly higher shrinking factor, $\langle G \rangle = 0.61$, when compared to that of conventional SCNPs, $\langle G \rangle = 0.87$, synthesized from exactly the same precursor polymer but without involving the first folding step.

4.6. References

[1] Trabi, M.; Craik, D. J. Circular proteins – no end in sight. *Trends in Biochemical Science*, **2002**, *27*, 132-138.

[2] Zhang, R.-Y.; Thapa, P.; Espiritu, M. J.; Menon, V.; Bingham, J.-P. Constrained peptides and biological targets. *Bioorganic & Medicinal Chemistry*, **2018**, *26*, 1135-1150.

[3] Camarero, J. A. Cyclotides, a versatile ultrastable micro-protein scaffold for biotechnological applications. *Bioorganic & Medicinal Chemistry Letters*, **2017**, *27*, 5089-5099.

[4] Contreras, J.; Elnagar, A.Y.; Hamm-Alvarez, S.F.; Camarero, J.A. Celullar uptake of cyclotide MCoTI-I follows multiple endocytic pathways. *Journal of Controlled Release*, **2011**, *155*, 134-143.

[5] Cascales, L.; Henriques, S.T.; Kerr, M.C.; Huang, Y.H.; Sweet, M.J.; Daly, M.L.; Craik, D.J. Identification and characterization of a new family of cell-penetrating peptides. *Journal of Biological Chemistry*, **2011**, *286*, 36932-36943.

[6] Ji, Y.; Majumder, S.; Millard, M.; Borra, R.; Bi, T.; Elnagar, A.Y.; Neamati, N.; Shekhtman, A.; Camarero, J. A. In vivo activation of the p53 tumor suppressor pathway by an engineered cyclotide. *Journal of the American Chemical Society*, **2013**, *135*, 11623-11633.

[7] Garcia, A.E.; Camarero, J. A. Biological activities of natural and engineered cyclotides, a novel molecular scaffold for peptide-based therapeutics. *Current Molecular Pharmacology*, **2010**, *3*, 153-163.

[8] Li, Y.; Bi, T.; Camarero, J. A. Chemical and biological production of cyclotides. *Advances in Botanical Research*, **2015**, *76*, 271-303.

[9] Suzuki, T.; Yamamoto, T.; Tezuka, Y. Constructing a macromolecular $K_{3,3}$ graph through electrostatic self-assembly and covalent fixation with a dendritic polymer precursor. *Journal of the American Chemical Society*, **2014**, *136*, 10148-10155.

[10] Tezuka, Y. Topological polymer chemistry designing complex macromolecular graph constructions. *Accounts of Chemical Research*, **2017**, *50*, 2661-2672.

[11] Uehara, E.; Deguchi, T. Statistical and hydrodynamic properties of topological polymers for various graphs showing enhanced short-range correlation. *Journal of Chemical Physics*, **2016**, *145*, 164905.

[12] Hill, D. J.; Mio, M. J.; Prince, R. B.; Hughes, T. S.; Moore, J. S. A field guide to foldamers. *Chemical Reviews*, **2001**, *101*, 3893-4012.

[13] Liang, C.; Fréchet, J. M. J. Applying key concepts from nature: transition state stabilization, pre-concentration and cooperativity effects in dendritic biomimetics. *Progress in Polymer Science*, **2005**, *30*, 385-402.

[14] Gonzalez−Burgos, M.; Latorre−Sanchez, A.; Pomposo, J. A. Advances in single − chain technology. *Chemical Society Reviews*, **2015**, *44*, 6122−6142.

[15] Altintas, O.; Barner-Kowollik, C. Single-chain folding of synthetic polymers: a critical update. *Macromolecular Rapid Communications*, **2016**, *37*, 29-46.

[16] Pomposo, J. A. Single-Chain Polymer Nanoparticles: Synthesis, Characterization, Simulations and Applications, *Wiley*, **2017**.

[17] Mavila, S.; Eivgi, O.; Berkovich, I.; Lemcoff, N. G. Intramolecular cross-linking methodologies for the synthesis of polymer nanoparticles. *Chemical Reviews*, **2016**, *116*, 878-961.

[18] Hanlon, A. M.; Martin, I.; Bright, E. R.; Chouinard, J.; Rodriguez, K. J.; Patenottea, G. E.; Berda, E. B. Exploring structural effects in single-chain "folding" mediated by intramolecular thermal Diels-Alder chemistry. ***Polymer Chemistry,*** **2017**, ***8***, 5120-5128.

[19] Lyon, C. K.; Prasher, A.; Hanlon, A. M.; Tuten, B. T.; Tooley, C. A.; Frank, P. G.; Berda, E. B. A brief user's guide to single−chain nanoparticles. *Polymer Chemistry*, **2015**, *6*, 181−197.

[20] Sanchez−Sanchez, A.; Pomposo, J. A. Single−chain polymer nanoparticles via non−covalent and dynamic covalent bonds. *Particle & Particle Systems Characterization*, **2014**, *31*, 11−23.

[21] Artar, M.; Huerta, E.; Meijer, E. W.; Palmans, A. R. A. Sequence-Controlled Polymers: Synthesis, Self-Assembly, and Properties. *American Chemical Society*: *2014*, *1170*, 313−325.

[22] Sanchez−Sanchez, A.; Pérez−Baena, I.; Pomposo, J. A. Advances in click chemistry for single−chain nanoparticle construction. *Molecules*, **2013**, *18*, 3339−3355.

[23] Altintas, O.; Barner−Kowollik, C. Single−chain folding of synthetic polymers: a critical update. *Macromolecular Rapid Communications*, **2012**, *33*, 958−971.

[24] Aiertza, M.; Odriozola, I.; Cabañero, G.; Grande, H.−J.; Loinaz, I. Single−chain polymer nanoparticles. *Cellular and Molecular Life Sciences*, **2012**, *69*, 337−346.

[25] Cole, J. P.; Lessard, J. J.; Rodriguez, K. J.; Hanlon, A. M.; Reville, E. K.; Mancinelli, J. P.; Berda, E. B. Single-chain nanoparticles containing sequence-defined segments: using primary structure control to promote secondary and tertiary structures in synthetic protein mimics. ***Polymer Chemistry,*** **2017**, ***8***, 5829-5835.

[26] Gonzalez−Burgos, M.; Alegria, A.; Arbe, A.; Colmenero, J.; Pomposo, J. A. An unexpected way to aldehyde−decorated single−chain nanoparticles from azides. *Polymer Chemistry*, **2016**, *43*, 6570−6574.

[27] Blasco, E.; Tuten, B. T.; Frisch, H.; Lederer, A.; Barner-Kowollik, C. Characterizing single chain nanoparticles (SCNPs): a critical survey. *Polymer Chemistry*, **2017**, *8*, 5845-5851.

[28] Huo, M.; Wang, N.; Fang, T.; Sun, M.; Wei, Y.; Yuan, J. Single-chain polymer nanoparticles: mimic the proteins. *Polymer*, **2015**, *66*, A11-A21.

[29] Bai, Y.; Xing, H.; Vincil, G. A.; Lee, J.; Henderson, E. J.; Lu, Y.; Lemcoff, N. G.; Zimmerman, S. C. Practical synthesis of water-soluble organic nanoparticles with a

single reactive group and a functional carrier scaffold. *Chemical Science*, **2014**, *5*, 2862-2868.

[30] Sanchez−Sanchez, A.; Akbari, S.; Etxeberria, A.; Arbe, A.; Gasser, U.; Moreno, A. J.; Colmenero, J.; Pomposo, J. A. "Michael" nanocarriers mimicking transient−binding disordered proteins. *ACS Macro Letters*, **2013**, *2*, 491−495.

[31] Perez−Baena, I.; Loinaz, I.; Padro, D.; García, I.; Grande, H. J.; Odriozola, I. Single−chain polyacrylic nanoparticles with multiple Gd (III) centres as potential MRI contrast agents. *Journal of Materials Chemistry*, **2010**, *20*, 6916−6922.

[32] Hamilton, S. K.; Harth, E. Molecular dendritic transporter nanoparticle vectors provide efficient intracellular delivery of peptides. *ACS Nano*, **2009**, *3*, 402-410.

[33] Rothfuss, H.; Knöfel, N. D.; Roesky, P. W.; Barner-Kowollik, C. Single-chain nanoparticles as catalytic nanoreactors. *Journal of the American Chemical Soc*iety, **2018**, *140*, 5875−5881.

[34] Rubio-Cervilla, J.; González, E.; Pomposo, J. A. Advances in single-chain nanoparticles for catalysis applications. *Nanomaterials*, **2017**, *7*, 341.

[35] Knöfel, N. D.; Rothfuss, H.; Willenbacher, J.; Barner-Kowollik, C.; Roesky, P. W. Platinum(II)-crosslinked single-chain nanoparticles: an approach towards recyclable homogeneous catalysts. *Angewandte Chemie, International Edition*, **2017**, *56*, 4950-4954.

[36] Latorre-Sanchez, A.; Pomposo, J. A. Recent bioinspired applications of single-chain nanoparticles. *Polymer International*, **2016**, *65*, 855-860.

[37] Tooley, C. A.; Pazicni, S.; Berda, E. B. Toward tunable synthetic [FeFe] hydrogenase mimic: single-chain nanoparticles functionalized with a single diiron cluster. *Polymer Chemistry*, **2015**, *6*, 7646-7651.

[38] Perez−Baena, I.; Barroso−Bujans, F.; Gasser, U.; Arbe, A.; Moreno, A. J.; Colmenero, J.; Pomposo, J. A. Endowing single−chain polymer nanoparticles with enzyme−mimetic activity. *ACS Macro Letters*, **2013**, *2*, 775−779.

[39] Huerta, E.; Stals, P .J. M.; Meijer, E. W.; Palmans, A. R. A. Consequences of folding a water-soluble polymer around an organocatalyst. *Angewandte Chemie, International Edition*, **2013**, *52*, 2906-2910.

[40] Terashima, T.; Mes, T.; De Greef, T. F. A.; Gillissen, M. A. J.; Besenius, P.; Palmans, A. R. A.; Meijer, E. W. Single−chain folding of polymers for catalytic systems in water. *Journal of the American Chemical Society*, **2011**, *133*, 4742−4745.

[41] Freytag, K.; Safken, S.; Wolter, K.; Namyslo, J. C.; Hubner, E. G. Hybrid single-chain nanoparticles via the metal induced crosslinking of N-donor functionalized polymer chains. ***Polymer Chemistry,*** **2017**, ***8***, 7546-7558.

[42] Pomposo, J. A.; Perez−Baena, I.; Lo Verso, F.; Moreno, A. J.; Arbe, A.; Colmenero, J. How far are single−chain nanoparticles in solution from the globular state? *ACS Macro Letters*, **2014**, *3*, 767−772.

[43] Formanek, M.; Moreno, A. J. Effects of precursor topology and synthesis under crowding conditions on the structure of single-chain polymer nanoparticles. *Soft Matter,* **2017**, *13*, 6430-6438.

[44] Baeten, E.; Rubens, M.; Wuest, K.; Barner-Kowollik, C.; Junkers, T. Photo-induced ring-closure via a looped flow reactor. *Reaction Chemistry & Engineering*, **2017**, *2*, 826-829.

[45] Oehlenschlaeger, K. K.; Mueller, J. O.; Heine, N.B.; Glassner, M.; Guimard, N. K.; Delaittre, G.; Schmidt, F. G.; Barner-Kowollik, C. Light-induced modular ligation of conventional RAFT polymers. *Angewandte Chemie., International Edition*, **2013**, *52*, 762-766.

[46] Tang, Q.; Wu, Y.; Sun, P.; Chen, Y.; Zhang, K. Powerful ring-closure method for preparing varied cyclic polymers. *Macromolecules*, **2014**, *47*, 3775-3781.

[47] Tornoe, C.W.; Christensen, C.; Meldal, M. Peptidotriazoles on solid phase: [1,2,3]-triazoles by regiospecific copper(I)-catalyzed 1,3-dipolar cycloadditions of terminal alkynes to azides. *Journal of Organic Chemistry*, **2002**, *67*, 3057-3064.

[48] Rostovtsev, V. V.; Green, L. G.; Fokin, V. V.; Sharpless, K. B. A stepwise Huisgen cycloaddition process: copper (I)-catalyzed regioselective "ligation" of azides and terminal alkynes. *Angewandte Chemie, International Edition*, **2002**, *41*, 2596-2599.

[49] Sun, S.; Wu, P. Mechanistic insights into Cu(I)-catalyzed azide-alkyne "click" cycloaddition monitored by real time infrared spectroscopy. *Journal of Physical Chemistry A,* **2010**, *114*, 8331-8336.

[50] Pomposo, J. A.; Perez-Baena, I.; Buruaga, L.; Alegría, A.; Moreno, A. J,; Colmenero, J. On the apparent SEC molecular weight and polydispersity reduction upon intramolecular collapse of polydisperse chains to unimolecular nanoparticles. *Macromolecules,* **2011**, *44*, 8644-8649.

[51] Latorre-Sánchez, A.; Alegría, A.; Lo Verso, F.; Moreno, A. J.; Arbe, A.; Colmenero, J.; Pomposo, J. A. A useful methodology for determining the compaction degree of single-chain nanoparticles by conventional SEC. *Particle & Particle System Characterization*, **2016**, *33*, 373-381.

[52] Glassner, M.; Blinco, J. P.; Barner-Kowollik, C. Diels-Alder reactions as an efficient route to high purity cyclic polymers. *Macromolecular Rapid Communications,* **2011**, *32*, 724-728.

[53] Willenbacher, J.; Altintas, O.; Roesky, P. W.; Barner-Kowollik, C. Single-chain self-folding of synthetic polymers induced by metal-ligand complexation. *Macromolecular Rapid Communications,* **2014**, *35*, 45-51.

CHAPTER 5

Size reduction upon reversible SCNP formation

5.1. Introduction

As mentioned in the previous sections, single-chain nanoparticles (SCNPs) are versatile folded/collapsed soft nano-objects of ultra-small size (3-20 nm) synthesized from single-chain precursors [1-12]. Significant effort has been spent in last years to endow SCNPs with useful and bioinspired applications [13-25]. In recent years, in addition to the preparation of permanent, covalent-bonded SCNPs an increasing interest in the development of stimuli-responsive SCNPs constructed *via* reversible interactions has been generated [2-9, 11].

Non-covalent bonded SCNPs *via* hydrogen bonding interactions were synthesized in a pioneering work by Hawker, Kim and co-workers [26]. Significant advances in the field were carried out by Palmans, Meijer et al. by utilizing ureido-pyrimidinone (UPy) dimerization [27-30] and benzene-1,3,5-tricarboxamide (BTA) helical stacking [22, 31-37] as intra-chain reversible interactions. Recently, intramolecular quadruple hydrogen bonding interactions have been employed by Pu *et al*. [38] to obtain reversible SCNPs. Host-guest interactions involving a cucurbit[8]uril cage compound were exploited by Scherman and coworkers [39] to produce responsive SCNPs based on ternary complex formation between cucurbit[8]uril (host) and viologen and naphtyl moieties (guests). More recently, voltage-responsive SCNPs have been prepared by Pu et al. [40] via cyclodextrin-ferrocene host-guest interactions. Concerning reversible covalent bonds, dynamic covalent SCNPs were synthesized by Murray and Fulton [41] in a pioneering work utilizing hydrazone reversible bonds. SCNPs prepared via reversible disulfide bridges were reported by Berda and coworkers [42]. Recently, redox-responsive SCNPs have been constructed by Thayumanavan et al. [43] via intra-chain disulfide exchange

reactions. pH-responsive SCNPs were synthesized by Fulton, Pomposo and co-workers [44] by exploiting dynamic covalent enamine bonds. Recently, Barner-Kowollik and colleagues reported dynamic covalent single-chain nanoparticles based on hetero Diels-Alder chemistry [45]. Coumarin and anthracene photodimerization reactions were introduced by Zhao et al. [46] and Berda et al. [47], respectively, for the construction of UV-light responsive SCNPs. Concerning metal complexation, several strategies have been developed to synthesize Ru- [22], Rh- [48], Cu- [49-52], Pd- [53], Ir-/Ni- [54] and Fe- [55] containing SCNPs. All the above reversible SCNPs can be disassembled by means of one or several appropriate stimuli (e.g., temperature increase, addition of competitive host compounds, pH decrease/increase, redox potential changes).

More complex reversible SCNP systems have been constructed based on triblock and tetrablock copolymers. Hence, Weck and co-workers have prepared single-chain hairpins based on triblock ABC copolymers using multiple p-p stacking interactions between phenyl and pentafluorophenyl residues of the A and C blocks, respectively [56]. Reversible SCNPs that unfold in a stepwise manner by chemically triggered gates have been reported by Barner-Kowollik and co-workers based on tetrablock ABCD copolymers using the combination of host-guest complexation between benzo-21-crown-7 with secondary ammonium salts and Hamilton-wedge / cyanuric acid hydrogen bonding interactions [57].

For covalent-bonded (irreversible) SCNPs, a detailed analysis of the size reduction upon SCNP formation was previously carried out [58]. The analysis revealed that, in general, permanent SCNPs in solution adopt open, sparse morphologies resembling those typical of intrinsically disordered proteins, instead of compact globule morphologies [59]. A

similar in-depth analysis of size reduction for SCNPs constructed via reversible bonds has not yet been performed.

5.2. Objectives

In this work, we use a Flory-like argument to obtain a simple expression providing the expected size reduction upon folding single chains of size R_0 to SCNPs of size R via reversible interactions (Figure 5.1). Subsequently, we perform a comparison of the predicted size reduction to extensive experimental data (72 SCNPs, 22 reversible interactions) taken from the literature concerning SCNPs constructed via reversible bonds.

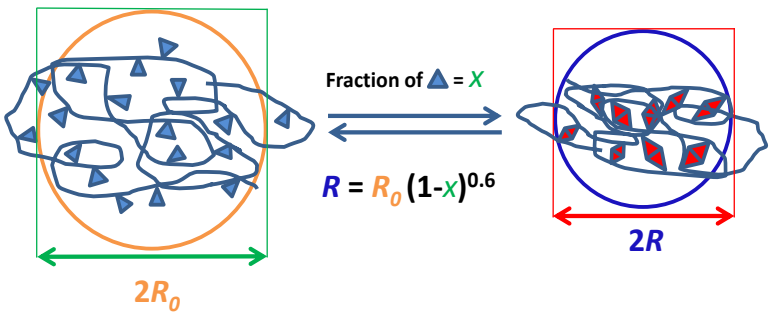

Figure 5.1. Scheme of the size reduction of a polymer chain of size $2R_0$ upon reversible SCNP formation.

The overall agreement between theoretical and experimental data is excellent, hence allowing a valuable a priori estimation of the size reduction upon folding single chains to single-chain nanoparticles via reversible interactions. In addition, a comparison of the level of chain compaction between reversible and irreversible SCNPs of the same nature, molar mass and amount of reactive groups is performed.

5.3. Results and discussion

Table 5.1 summarizes the relevant data for the different 72 responsive SCNPs (22 different types of reversible interactions) that we are considering in this work. As it is described in the corresponding references and compiled in Table 5.2, all these SCNPs were synthesized under the following conditions: (i) good solvent conditions; (ii) high dilution (≤ 1 mg/mL) far below the overlap concentration c*, where c* is typically in the range 30-100 mg/mL; (iii) reversible crosslinking interactions.

Under these conditions, the formation of intermolecular aggregates is statistically very infrequent because there is not driving force to form them. Unlike in the case of bad solvent conditions, in terms of energy there will be no preference for intermolecular aggregation that will compensate the associated entropic loss. Anyway, the single-chain nature of these nanoparticles was checked by means of different experimental techniques (see the corresponding references) as it is summarized in Table 5.2.

Table 5.1 includes the hydrodynamic size for the 72 SCNPs considered. The hydrodynamic size of the precursor (R_H^{SEC}) was calculated according to: $R_H^{SEC}(nm) = 1.44\times10^{-2}\ M_w^{0.561}$, which is the recommended expression for estimating the hydrodynamic radius based on M_w data from size exclusion chromatography (SEC) in tetrahydrofuran (THF) calibrated with PS standards [59]. From the reported apparent weight average molecular weight [60] from SEC measurements in THF (M_w^{app}), the hydrodynamic radius of the SCNP was obtained as $R_H^{SEC}(nm) = 1.44\times10^{-2}\ (M_w^{app})^{0.561}$. Hydrodynamic size data as determined from dynamic light scattering (DLS) measurements in THF (R_H^{DLS}) are also provided in Table 5.1, when available.

To derive an expression providing the expected size reduction upon folding single chains of size R_0 to conventional SCNPs of size R via reversible interactions we follow a Flory-like argument [61]. We consider a SCNP in good solvent with a number of segments N and segment length b having a fraction of groups x involved in reversible bonds (Figure 5.2A). Let us consider that the groups interacting through reversible bonds are placed statistically along the SCNP chain. We obtain the free energy of this system, F_T, by assuming that actually only the non-bonded segments, (1-x)N, contribute effectively to the excluded volume, F_{exc}, and entropic, F_{ent}, terms. Therefore, the Flory expression for the free energy [57] is modified as:

$$\frac{F_T}{k_BT} = \frac{F_{exc}}{k_BT} + \frac{F_{ent}}{k_BT} \approx \tag{5.1}$$

$$\approx \frac{\upsilon(1-x)^2N^2}{R^3} + \frac{R^2}{(1-x)Nb^2}$$

with υ the excluded volume parameter. By minimizing F_T with respect to R we obtain:

$$R = \left(\frac{3}{2}\right)^{\frac{1}{5}} \upsilon^{\frac{1}{5}} b^{\frac{2}{5}}(1-x)^{\frac{3}{5}}N^{\frac{3}{5}} \tag{5.2}$$

R_0 results by putting x = 0 in Equation 5.2:

$$R_0 = \left(\frac{3}{2}\right)^{\frac{1}{5}} \upsilon^{\frac{1}{5}} b^{\frac{2}{5}} N^{\frac{3}{5}} \tag{5.3}$$

Finally, from Equations 5.2 and 5.3 we have:

$$R = R_0(1-x)^{0.6} \tag{5.4}$$

Implicit in Equation 5.4 is the approximation that, concomitant to SCNP formation, all potential intra-chain reversible bonds are formed. This is a good approximation, since the fraction of formed bonds should be about $[1-\exp(-\Delta E/k_BT)]$, and the energy scale ΔE of the reversible bonds is several tenths the thermal energy k_BT. Also, Equation 5.4 is expected to apply only to SCNPs in which the solvent guarantees an appropriate balance between backbone solubility and self-assembly capability of the reversible bonds. Experimentally, it its well-known that for SCNP formation via reversible interactions, one has to consider the critical balance between backbone solubility and self-assembly capability of the reversible bonds (e.g., hydrogen bonding interactions) [30]. Consequently, an appropriate solvent polarity must be selected to promote single chain folding/collapse versus intermolecular aggregation [32].

Moreover, the assumption of an identical scaling exponent $\nu = 0.6$ for SCNPs (Equation 5.2) and precursors (Equation 5.3) is valid only if chain compaction takes place mostly at the local scale and the global conformation remains self-avoiding. Equation 5.4 is expected to suffer from the same type of shortcomings and error cancellations as in Flory´s original theory [61].

Table 5.1. Size data for different single-chain nanoparticles (SCNPs) constructed *via* reversible interactions compared to calculated size data from Equation 5.4.

Precursors							**SCNPs**						
#	**Type**[a]	x[b]	M_w **(kDa)**[c]	$Đ$[d]	R_H^{SEC} **(nm)**[e]	R_H^{DLS} **(nm)**[f]	**Reversible Interactions**[g]	**SCNP** M_w^{app} **(kDa)**[h]	R_H^{SEC} **(nm)**[e]	R_H^{CAL} **(SEC) (nm)**[i]	R_H^{DLS} **(nm)**[f]	R_H^{CAL} **(DLS) (nm)**[i]	**Ref**
1	PNOR	0.20	321	1.55	17.7	-	UPy dimerization	236	14.9	15.5	-	-	27
2	PMMA	0.10	18.5	1.39	3.6	-		14.9	3.2	3.4	-	-	28
3		0.10	87.9	1.54	8.6			71.8	7.6	8.0			
4		0.15	22.4	1.29	4.0			17.4	3.5	3.6			
5		0.20	82.0	1.40	8.2			62.0	7.0	7.2			
6		0.40	79.0	1.42	8.1			36.0	5.2	5.9			
7	PMMA	0.10	27.9	1.12	4.5	5.0		23.8	4.1	4.2	5.0	4.7	30
8		0.11	97.1	1.43	9.1	12.6		87.7	8.5	8.5	11.8	11.7	
9		0.08	28.0	1.16	4.5	-		25.6	4.3	4.3	-	-	
10	PnBA	0.09	89.6	1.84	8.6	9.3		64.5	7.2	8.1	9.9	8.8	
11	PS	0.12	27.6	1.17	4.5	4.8		22.5	4.0	4.2	4.4	4.4	
12		0.05	33.6	1.17	5.0	6.3		28.4	4.5	4.8	5.7	6.1	
13	PNOR	0.07	71.8	1.26	7.6	7.3		74.6	7.8	7.3	6.3	7.0	
14	PIBMA	0.04	32.6	1.16	4.9	-		30.7	4.7	4.8	-	-	32
15		0.04	66.3	1.26	7.3			58.4	6.8	7.1			
16		0.04	181.0	1.46	12.8			157.3	11.9	12.5			
17	POEGMA	0.10	81.9	1.37[j]	-	7.7[k]	BTA helical stacking	77.6	-	-	7.1	7.2	22
18		0.10	81.9	1.37[j]	-	7.4[l]		77.6	-	-	6.9	6.9	
19	PMMA	0.05	55.0	1.97	-	6.6[m]	Quadruple hydrogen bonding	-	-	-	6.6[m]	6.4	38
20		0.10	41.6	1.67		5.9[m]					5.7[m]	5.5	
21		0.15	45.0	1.86		5.8[m]					5.1[m]	5.3	
22		0.05	112.9	2.45		7.9[m]					7.9[m]	7.7	

23		0.10	132.0	2.87		7					6.6[m]	6.6	
24	PHEAm	0.10	166	1.15	-	6.8[n]	Cucurbit[*8*] uril complexation	-	-	-	6.0[n]	6.4	39
25		0.10	330	1.24		10.7[n]					9.4[n]	10.1	
26		0.10	593	1.23		12.3[n]					10.7[n]	11.5	
27		0.30	245	1.01		9.2[n]					5.4[n]	7.4	
28	PHEAm	0.04	71.1	1.21	-	6.5[n]	Cyclodextrin-ferrocene complexation	-	-	-	5.1[n]	6.3	40
29		0.04	54.7	1.30		5.9[n]					4.7[n]	5.7	
30		0.07	90.3	1.36		6.9[n]					4.4[n]	6.6	
31	PS	0.20	5.6	1.21	1.8	-	Hydrazone reversible bonds	4.4	1.6	1.6	-	-	41
32		0.05	6.8	1.18	2.0			6.7	2.0	1.9			
33		0.10			2.0			6.3	1.9	1.9			
34		0.20			2.0			5.6	1.8	1.8			
35		0.30			2.0			5.9	1.9	1.6			
36		0.20	8.5	1.22	2.3			7.4	2.1	2.0			
37		0.20	13.3	1.19	3.0			10.2	2.6	2.6			
38		0.40	16.0	1.17	3.3			12.4	2.8	2.4			
39		0.50	17.3	1.27	3.4			13.9	3.0	2.3			
40	PNOR	0.30	50.1	1.22	4.5[o]	-	Disulfide reversible bonds	-	3.9[o]	3.6	-	-	42
41	PHEMA	0.10	95.4	1.24	-	4.9[p]	Disulfide exchange	-	-	-	4.3[p]	4.6	43
42	PMMA	0.30	30.9	1.05	-	3.9	Enamine reversible bonds	-	-	-	2.7	3.1	44
43		0.30	53.5	1.05		5.3					3.4	4.3	
44		0.30	309.4	1.30		13.9					7.1	11.2	
45	PMMA	0.17	13.8[q]	1.3[q]	-	2.0	HDA reversible bonds	11.7	-	-	1.7	1.8	45
46	PDMAEMA	0.08	110.0	1.2	9.7	-	Coumarin dimerization	74.0	7.8	9.2	-	-	46
47		0.13	104.0	1.2	9.4	-		75.0	7.8	8.6	-	-	

48	PMMA	0.10	30.8	1.17	4.0[o]	-	Anthracene dimerization	-	3.4[o]	3.9	-	-	47
49		0.20	30.6	1.14	3.6[o]				2.9[o]	3.1			
50		0.46	42.9	1.16	3.5[o]				2.3[o]	2.4			
51	PCOD	0.01	33.5	1.34	-	9.3	Rh-complexation	-	-	-	8.9	9.2	48
52		0.02									8.5	9.1	
53		0.05									8.1	9.0	
54		0.10									7.4	8.6	
55	POEGMA	0.11	110.1	1.04	7.9[o]	-	Cu-complexation	-	7.0[o]	7.4	-	-	51
56		0.20	90.4	1.10	7.1[o]				6.6[o]	6.2			
57		0.35	175.0	1.08	9.8[o]				8.1[o]	7.6			
58		0.40	208.0	1.05	11.0[o]				8.4[o]	8.1			
59	PS	0.03	57.2	1.15	-	6.7	Cu-phthalocyanine formation	-	-	-	6.6	6.6	52
60		0.09									5.7	6.3	
61		0.17									5.3	5.9	
62	PS	0.12	14.3	1.16	3.1	4.4	Pd-complexation	10.5	2.6	2.9	2.7	4.0	53
63	PCOD	0.02	50.6	1.02	-	10.1	Ir-complexation	-	-	-	9.4	9.9	54
64		0.05									8.6	9.8	
65		0.10									7.9	9.5	
66		0.10	45.3	1.03	-	10.5	Ni-complexation	-	-	-	9.6	9.9	
67		0.20									9.1	9.2	
68		0.30									8.0	8.5	
69	PHEAm	0.05	43.4	-	-	4.5[n]	Fe-complexation	-	-	-	2.5[n]	4.3	55
70		0.10	48.9			4.7[n]					2.4[n]	4.4	
71	Triblock ABC copolymer	0.38	35.4[r]	1.7[r]	-	10.1[s]	π-π stacking (between A and C blocks)	-	-	-	4.3[t]	7.6	56
72	Tetrablock ABCD copolymer	0.08	77.8[u]	1.2[u]	-	5.0[v]	B21C7 / AS complexation (between B	-	-	-	3.0[v]	4.8	57

							and C blocks) + HW / CA hydrogen bonding (between A and D blocks)						

[a] PNOR = Polynorbornene; PMMA = Polymethyl methacrylate; PnBA = Poly(*n*-butyl methacrylate); PS = Polystyrene; PIBMA = Poly(isobornyl methacrylate); POEGMA = Polyoligoethylene glycol methyl ether methacrylate; PHEAm = Poly(*N*-2-hydroxyethyl acrylamide); PHEMA = Poly(hydroxyethyl methacrylate); PDMAEMA = Poly(N,N-dimethylaminoethyl methacrylate); PCOD = Polycyclooctadiene. [b] Relative amount of functional groups in the linear precursor, as determined by ^{1}H NMR spectroscopy. [c] Weight average molecular weight referred to PS standards (unless otherwise stated). [d] Dispersity of the molecular weight distribution referred to PS standards (unless otherwise stated). [e] For the precursors: R_H^{SEC} (nm) = 1.44×10^{-2} $M_w^{0.561}$ (see ref. 59); for the SCNPs: R_H^{SEC} (nm) = 1.44×10^{-2} $(M_w^{app})^{0.561}$. [f] Data from dynamic light scattering (DLS) measurements in THF (unless otherwise stated). [g] UPy = 2-Ureido-Pyrimidinone, HAD = Hetero Diels-Alder, BTA = Benzene-1,3,5-tricarboxamide, B21C7 = Benzo-21-crown-7, AS = Ammonium salt, HW = Hamilton wedge, CA = Cyanuric acid. [h] M_w^{app} is the *apparent* weight average molecular weight of the SCNP referred to PS standards (see ref. 60). [i] R_H^{CAL} (nm) = $R_H^{Precursor}$ (nm) × $(1\text{-}x)^{0.6}$ (see Eq. 4). [j] Data from SEC in DMF (10 mM LiBr) referred to PMMA standards. [k] Measurements in H_2O; concentration = 1.0 mg mL^{-1}; T = 40 ºC. [l] Measurements in H_2O; concentration = 5.0 mg mL^{-1}; T = 25 ºC. [m] Measurements in $CHCl_3$. [n] Measurements in H_2O. [o] Hydrodynamic radius determined by SEC with differential refractive index, multi-angle laser light scattering and viscosimetry detectors. [p] Measurements in MeOH. [q] Data from SEC in DMAc referred to PS standards. [r] Data from SEC in DMF referred to PS standards. [s] Measurements in toluene. [t] Measurements in DMF. [u] Referred to PMMA standards. [v] Measurements in a mixture of DCM / acetonitrile (9 : 1, v / v).

Table 5.2. Combination of experimental techniques used to validate the single-chain nature of reversible SCNPs reported in Table 5.1.

Reference	Precursor concentration	DLS / type	SEC / type	Other characterizations techniques used
22	1 mg /mL	Intensity distribution	Light scattering detector	Cryo-TEM, Circular dichroism
27	1 mg /mL	Only average size provided	Conventional	AFM
28	1 mg /mL	-	Conventional	AFM
30	1 mg /mL	Intensity distribution	Conventional	AFM
32	1 mg /mL	-	Conventional	AFM
38	< 0.005 mg /mL	Number distribution	-	TEM , AFM
39	< 0.1 mg /mL	Intensity distribution	-	AFM
40	1 mg /mL	Number distribution	-	AFM
41	0.1 mM	-	Conventional	-
42	1 mg /mL	-	Light scattering detector	TEM
43	0.5 mg /mL	Volume distribution	Conventional	AFM
44	1 mg /mL	Number distribution	Conventional	-
45	1 mg /mL	Number distribution	Conventional	^{1}H NMR
46	1 mg /mL	-	Conventional	^{1}H NMR (spin-spin relaxation times), TEM
47	0.1 mg /mL	-	Light scattering detector	Viscosimetry
48	0.01 mM	Relative distribution	Conventional	TEM
49	1 mg /mL	Number distribution	Light scattering detector	SAXS
52	1 mg /mL	Distribution not provided	Conventional	AFM
53	1 mg /mL	Number distribution	Conventional	^{1}H NMR (spin-spin relaxation times)
54	1 mg /mL	Distribution not provided	Light scattering detector	-
55	1 mg /mL	Number distribution	-	AFM
56	1 mg /mL	Number distribution	Conventional	2D ^{1}H-^{1}H NOESY
57	< 1 mg /mL	Intensity distribution	Conventional	DOSY

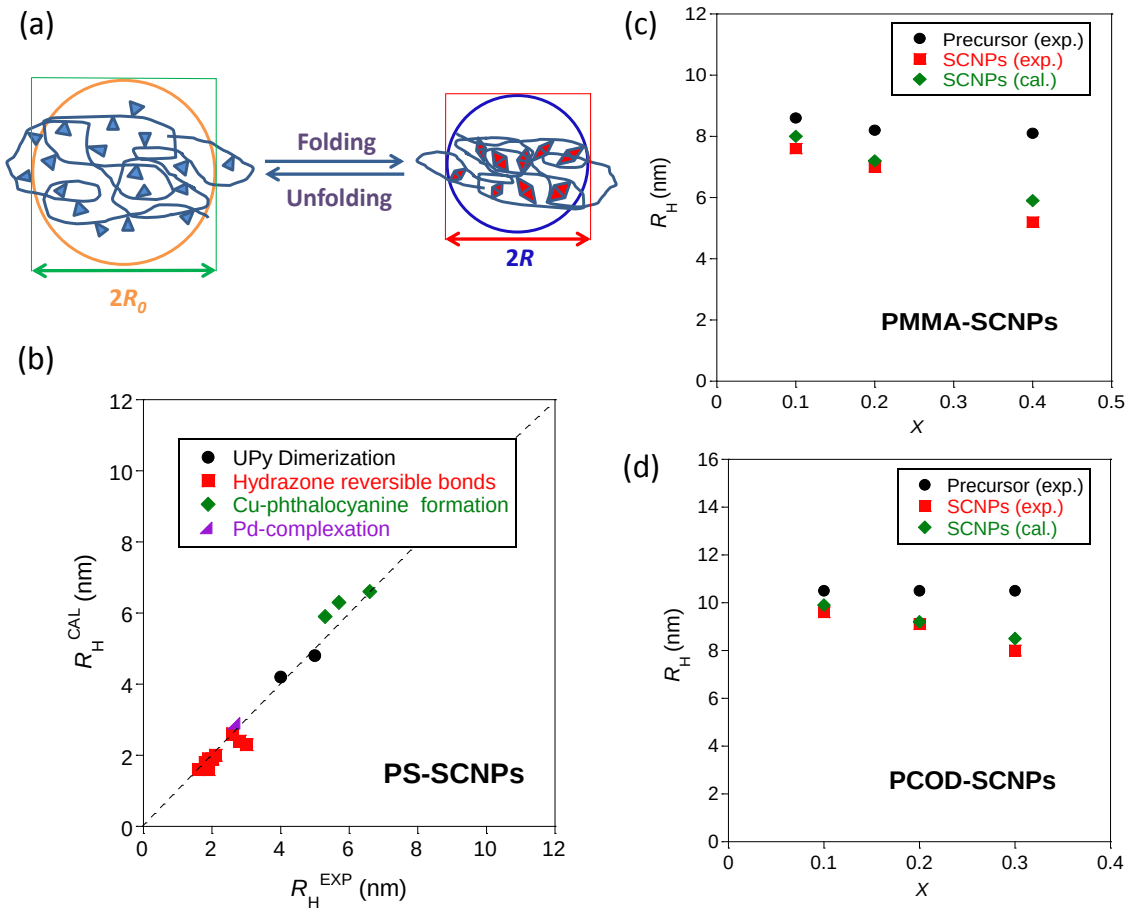

Figure 5.2. (a) Schematic illustration of the folding of a single chain of size R_0 (left) to a single-chain nanoparticle of size R (right) *via* reversible interactions. Folding and unfolding can be promoted by the use of an appropriate stimulus, e.g., change in solvent polarity. (b) Comparison of hydrodynamic radius calculated from Equation 5.4 (R_H^{CAL}) and experimental hydrodynamic radius (R_H^{EXP}) (SEC data unless otherwise stated) for reversible polystyrene (PS)-SCNPs prepared *via* ureido-pyrimidinone (UPy) dimerization [30], hydrazone reversible bonds [41], Cu-phthalocyanine formation (DLS data) [52] and Pd-complexation [53] (see Table 5.1). (c) Comparison of R_H^{CAL} (Equation 5.4) and R_H^{EXP} for polymethyl methacrylate (PMMA)-SCNPs synthesized *via* UPy dimerization [28] as a function of the fraction of groups x involved in reversible bonds. (d) Same as panel (c) but for polycyclooctadiene (PCOD)-SCNPs synthesized *via* Ni-complexation [54].

In spite of these limitations, we will show that this simple approach is in good agreement with literature results, providing a useful tool for predicting the size of conventional SCNPs involving reversible bonds placed statistically along the chain (Table 5.1, entries 1-70). As expected, Equation 5.4 fails to predict the size of complex

SCNP systems involving triblock ABC and tetrablock ABCD copolymers (Table 5.1, entries 71 and 72, respectively).

The expected hydrodynamic size reduction according to Equation 5.4 is reported in Table 5.1 for different SCNPs involving reversible interactions. The experimental techniques used to characterize these reversible SCNPs are summarized in Table 5.2. Inspection of data from Table 5.1 reveals that, in general, the agreement between hydrodynamic radii calculated from Equation 5.4 (R_H^{CAL}) and experimental hydrodynamic radii (R_H^{EXP}) is very good. As a representative example, Figure 5.2B shows a plot of R_H^{CAL} versus R_H^{EXP} for reversible polystyrene (PS)-SCNPs prepared via (i) ureido-pyrimidinone (UPy) dimerization [30], (Table 5.1, entries 11, 12) (ii) hydrazone reversible bonds [41], (Table 5.1, entries 31-39) (iii) Cu-phthalocyanine formation [52] (Table 5.1, entries 59-61) and (iv) Pd-complexation [53] (Table 5.1, entry 62). Even considering SCNPs constructed from very different reversible bonds, the average deviation of calculated data from experimental ones is only of 7 %.

Additionally, a comparison of calculated (Equation 5.4) and experimental hydrodynamic size data for polymethyl methacry-glycol methyl ether methacrylate (POEGMA) and poly(N,N-dimethylaminoethyl methacrylate) (PDMAEMA)-SCNPs (data from Table 5.1). The average deviation of calculated data from experimental ones is 6 %. Consequently, based on thelate (PMMA)-SCNPs synthesized via UPy dimerization [28] and polycyclooctadiene (PCOD)-SCNPs synthesized via Ni-complexation [54], as a function of x is illustrated in Figure 5.2C and 5.2D, respectively. The general trend of increased size reduction upon increasing x is well captured by Equation 5.4.

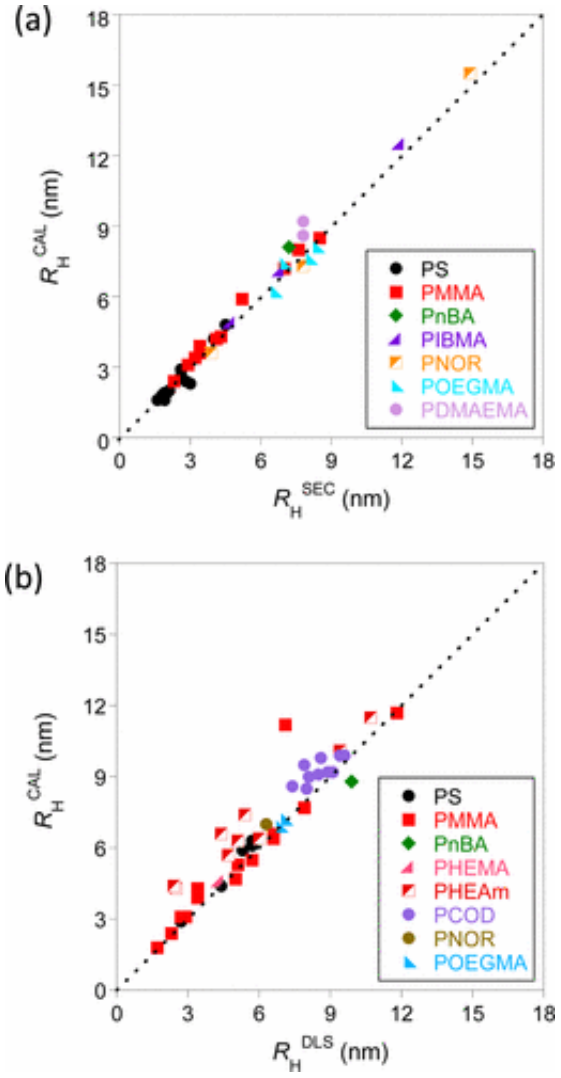

Figure 5.3. (a) Comparison of R_H^{CAL} (Equation 4) and experimental R_H^{SEC} for reversible PS-, PMMA-, PnBA-, PIBMA-, PNOR-, POEGMA-, and PDMAEMA-SCNPs. (b) Comparison of R_H^{CAL} (Equation 5.4) and experimental R_H^{DLS} for reversible PS-, PMMA-, PnBA-, PHEMA-, PHEAm-, PCOD-, PNOR-, and POEGMA-SCNPs. Data taken from Table 5.1.

Figure 5.3A shows a comparison of hydrodynamic radii calculated from Equation 5.4 (R_H^{CAL}) and experimental hydrodynamic radii determined by SEC (R_H^{SEC}) for reversible PS-, PMMA- , poly(n-butylacrylate) (PnBA)-, poly(isobornyl methacrylate) (PIBMA)-, polynorbornene (PNOR)-, polyoligoethylene hydrodynamic radius of the precursor as determined by SEC, a reliable estimation of the size reduction upon folding the precursor to a SCNP via reversible interactions can be obtained from Equation 5.4.

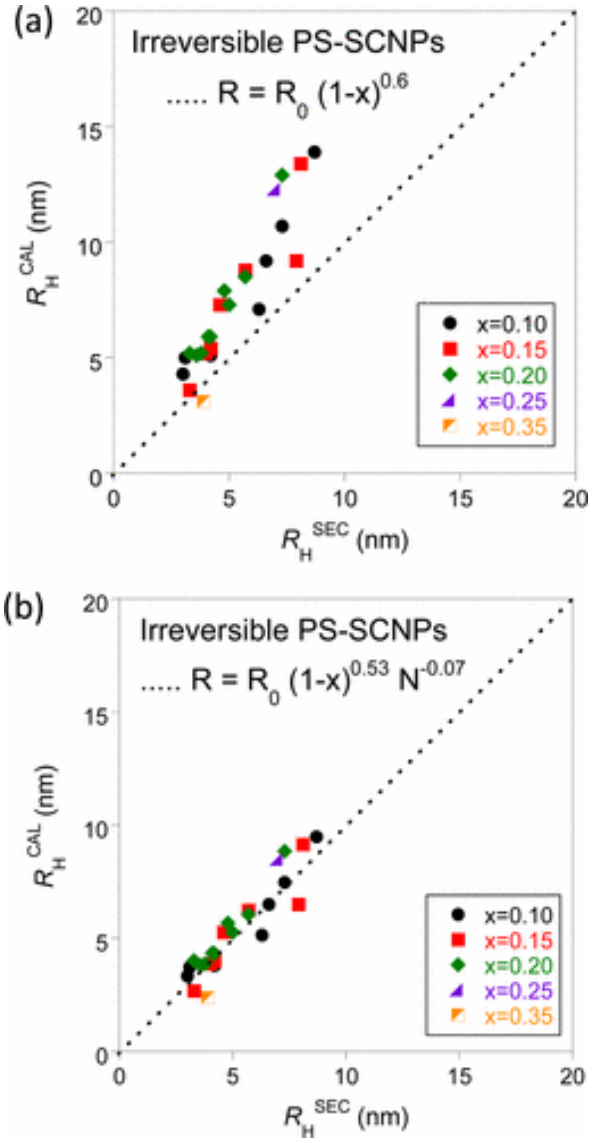

Figure 5.4. (a) Comparison of R_H^{CAL} (Equation 5.4) and experimental R_H^{SEC} for covalent-bonded (irreversible) PS-SCNPs (data taken from Reference 58). (b) Same as panel (a) but assuming a change in the scaling exponent (ν) in $R_H \propto N^{\nu}$ from ν = 0.6 (precursors) to ν = 0.53 (irreversible SCNPs) giving to [62] $R = R_0(1 - x)^{0.53}N^{-0.07}$.

However, significant data scatter is observed when experimental hydrodynamic radii from DLS (R_H^{DLS}) are compared to hydrodynamic radii calculated from Equation 5.4 (R_H^{CAL}) (see Figure 5.3B). It is worth mentioning that the DLS technique is more sensitive to the presence of impurities of large size in solution (*e.g.*, traces of SCNP aggregates) than the SEC technique [58], which could account for some of the scatter observed in Figure 5.3B when compared to Figure 5.3A. Also, SEC hydrodynamic data

are based on the use of highly diluted solutions, whereas DLS hydrodynamic results are often obtained from more concentrated solutions and sometimes involving the use of solvents different from THF.

Notably, Equation 4 does not reproduce the data of irreversible SCNPs (see Figure 5.4A, average deviation ≈ 44 %). This is a consequence of the change in scaling exponent (ν) in R_H α N^{ν} upon intra-chain covalent-bonded folding/collapse of the precursors to irreversible SCNPs, as reported previously in reference 58. Hence, a good agreement between theoretical and experimental data is found by assuming a change from ν = 0.6 (precursors) to ν = 0.53 (irreversible SCNPs) (see Figure 5.4B) [62]. The exponent ν = 0.53 is consistent with previous results from experiments and computer simulations of irreversible SCNPs [14, 23, 49, 58, 60, 63].

5.4. Conclusions

In this Chapter, SEC and DLS hydrodynamic size data for different responsive SCNPs, including 72 SCNPs and 22 reversible interactions, have been analyzed. An expression providing the expected size reduction upon folding single chains of size R_0 to SCNPs of size R via reversible interactions has been derived following a Flory-like argument. The overall agreement between theoretical and experimental data for conventional SCNPs involving reversible bonds placed statistically along the chain is excellent, hence allowing a valuable a priori estimation of size reduction upon folding single chains to single-chain nanoparticles via reversible interactions. When compared to covalent-bonded SCNPs with a non-globular, sparse conformation in solution, reversible SCNPs in solution with similar nature, molar mass and amount of reactive groups display, on

average, a lower level of chain compaction. This finding is of outmost importance for developing practical applications of responsive SCNPs based on structure – property relationships.

5.5. References

[1] Ouchi, M.; Badi, N.; Lutz, J.-F.; Sawamoto, M. Single-chain technology using discrete synthetic macromolecules. *Nature Chemistry*, **2011**, *3*, 917-924.

[2] Gonzalez-Burgos, M.; Latorre-Sanchez, A.; Pomposo, J. A. Advances in Single Chain Technology. *Chemical Society Reviews*, **2015**, *44*, 6122-6142.

[3] Mavila, S.; Eivgi, O.; Berkovich, I.; Lemcoff, N. G. Intramolecular Cross-Linking Methodologies for the Synthesis of Polymer Nanoparticles. *Chemical Reviews*, **2016**, *116*, 878-961.

[4] Hanlon, A. M.; Lyon, C. K.; Berda, E. B. What Is Next in Single-Chain Nanoparticles? *Macromolecules*, **2016**, *49*, 2-14.

[5] Altintas, O.; Barner-Kowollik, C. Single-Chain Folding of Synthetic Polymers: A Critical Update. *Macromolecular Rapid Communications*, **2016**, *37*, 29-46.

[6] Lyon, C. K.; Prasher, A.; Hanlon, A. M.; Tuten, B. T.; Tooley, C. A.; Frank, P. G.; Berda, E. B. A Brief User's Guide to Single-Chain Nanoparticles. *Polymer Chemistry*, **2015**, *6*, 181-197.

[7] Pomposo, J. A. Polymers: Single-Chain Polymer Nanoparticles. In CRC Concise Encyclopedia of Nanotechnology; Kharisov, B. I.; Kharissova, O. V.; Ortiz-Mendez, U., *CRC Press: Boca Raton, FL*, **2015**.

[8] Sanchez-Sanchez, A.; Pomposo, J. A. Single-Chain Polymer Nanoparticles via Non-Covalent and Dynamic Covalent Bonds. *Particle & Particle Systems Characterization*, **2014**, *31*, 11-23.

[9] Müge, A.; Elisa, H.; Meijer, E. W.; Anja, R. A. P. Dynamic Single Chain Polymeric Nanoparticles: From Structure to Function. In Sequence-Controlled Polymers: Synthesis, Self-Assembly, and Properties. *American Chemical Society,* **2014**, *1170*, 313-325.

[10] Sanchez-Sanchez, A.; Perez-Baena, I.; Pomposo, J. A. Advances in Click Chemistry for Single-Chain Nanoparticle Construction. *Molecules*, **2013**, *18*, 3339-3355.

[11] Altintas, O.; Barner-Kowollik, C. Single Chain Folding of Synthetic Polymers by Covalent and Non-Covalent Interactions: Current Status and Future Perspectives. *Macromolecular Rapid Communications*, **2012**, *33*, 958-971.

[12] Aiertza, M.; Odriozola, I.; Cabañero, G.; Grande, H.-J.; Loinaz, I. Single-chain polymer nanoparticles. *Cellular and Molecular Life Sciences*, **2012**, *69*, 337-346.

[13] Hamilton, S. K.; Harth, E. Molecular Dendritic Transporter Nanoparticle Vectors Provide Efficient Intracellular Delivery of Peptides. *ACS Nano*, **2009**, *3*, 402-410.
[14] Sanchez-Sanchez, A.; Akbari, S.; Moreno, A. J.; Lo Verso, F.; Arbe, A.; Colmenero, J.; Pomposo, J. A. Design and Preparation of Single-Chain Nanocarriers Mimicking Disordered Proteins for Combined Delivery of Dermal Bioactive Cargos. *Macromolecular Rapid Communications*, **2013**, *34*, 1681-1686.

[15] Perez-Baena, I.; Loinaz, I.; Padro, D.; Garcia, I.; Grande, H. J.; Odriozola, I. Single-chain Polyacrylic Nanoparticles with Multiple Gd(III) Centres as Potential MRI Contrast Agents. *Journal of Materials Chemistry*, **2010**, *20*, 6916-6922.

[16] Bai, Y.; Xing, H.; Vincil, G. A.; Lee, J.; Henderson, E. J.; Lu, Y.; Lemcoff, N. G.; Zimmerman, S. C. Practical Synthesis of Water-Soluble Organic Nanoparticles with a Single Reactive Group and a Functional Carrier Scaffold. *Chemical Science*, **2014**, *5*, 2862-2868.

[17] Gillissen, M. A. J.; Voets, I. K.; Meijer, E. W.; Palmans, A. R. A. Single Chain Polymeric Nanoparticles as Compartmentalised Sensors for Metal Ions. *Polymer Chemistry*, **2012**, *3*, 3166-3174.

[18] Latorre-Sanchez, A.; Pomposo, J. A. A simple, fast and highly sensitive colorimetric detection of zein in aqueous ethanol via zein–pyridine–gold interactions. *Chemical Communications*, **2015**, *51*, 15736-15738.

[19] Pomposo, J. A. Bioinspired single-chain polymer nanoparticles. *Polymer International*, **2014**, *63*, 589-592.

[20] Huo, M.; Wang, N.; Fang, T.; Sun, M.; Wei, Y.; Yuan, J. Single-chain polymer nanoparticles: Mimic the proteins. *Polymer*, **2015**, *66*, 11– 21.

[21] Latorre-Sanchez, A.; Pomposo, J. A. Recent bioinspired applications of single-chain nanoparticles. *Polymer International*, **2016**, *65*, 855-860.

[22] Terashima, T.; Mes, T.; De Greef, T. F. A.; Gillissen, M. A. J.; Besenius, P.; Palmans, A. R. A.; Meijer, E. W. Single-Chain Folding of Polymers for Catalytic Systems in Water. *Journal of the American Chemical Society*, **2011**, *133*, 4742-4745.

[23] Perez-Baena, I.; Barroso-Bujans, F.; Gasser, U.; Arbe, A.; Moreno, A. J.; Colmenero, J.; Pomposo, J. A. Endowing Single-Chain Polymer Nanoparticles with Enzyme-Mimetic Activity. *ACS Macro Letters*, **2013**, *2*, 775-779.

[24] Huerta, E.; Stals, P. J. M.; Meijer, E. W.; Palmans, A. R. A. Consequences of Folding a Water-Soluble Polymer around an Organocatalyst. *Angewandte Chemie, International Edition*, **2013**, *52*, 2906-2910.

[25] Tooley, C. A.; Pazicni, S.; Berda, E. B. Toward a Tunable Synthetic [FeFe] Hydrogenase Mimic: Single-Chain Nanoparticles Functionalized with a Single Diiron Cluster. *Polymer Chemistry*, **2015**, *6*, 7646-7651.

[26] Seo, M.; Beck, B. J.; Paulusse, J. M. J.; Hawker, C. J.; Kim, S. Y. Polymeric Nanoparticles via Noncovalent Cross-Linking of Linear Chains. *Macromolecules*, **2008**, *41*, 6413-6418.

[27] Foster, E. J.; Berda, E. B.; Meijer, E. W. Metastable Supramolecular Polymer Nanoparticles via Intramolecular Collapse of Single Polymer Chains. *Journal of the American Chemical Society,* **2009**, *131*, 6964-6966.

[28] Berda, E. B.; Foster, E. J.; Meijer, E. W. Toward Controlling Folding in Synthetic Polymers: Fabricating and Characterizing Supramolecular Single-Chain Nanoparticles. *Macromolecules*, **2010**, *43*, 1430-1437.

[29] Foster, E. J.; Berda, E. B.; Meijer, E. W. Tuning the size of supramolecular single-chain polymer nanoparticles. *Journal of Polymer Science, Part A: Polymer Chemistry*, **2011**, *49*, 118-126.

[30] Stals, P. J. M.; Gillissen, M. A. J.; Nicolay, R.; Palmans A. R. A.; Meijer, E. W. The balance between intramolecular hydrogen bonding, polymer solubility and rigidity in single-chain polymeric nanoparticles. *Polymer Chemistry*, **2013**, *4*, 2584-2597.

[31] Mes, T.; van der Weegen, R.; Palmans A. R. A.; Meijer, E. W. Single-Chain Polymeric Nanoparticles by Stepwise Folding. *Angewandte Chemie, International Edition*, **2011**, *50*, 5085-5089.

[32] Hosono, N.; Gillisen, M. A.; Li, Y.; Sheiko, S. S.; Palmans, A. R. A.; Meijer, E. W. Orthogonal Self-Assembly in Folding Block Copolymers. *Journal of the American Chemical Society,* **2012**, *135*, 501-510.

[33] Gillissen, M. A. J.; Terashima, T.; Meijer, E. W.; Palmans, A. R. A.; Voets, I. K. Sticky Supramolecular Grafts Stretch Single Polymer Chains. *Macromolecules*, **2013**, *46*, 4120-4125.

[34] Hosono, N.; Stals, P. J. M.; Palmans A. R. A.; Meijer, E. W. Consequences of Block Sequence on the Orthogonal Folding of Triblock Copolymers. *Chemistry - an Asian Journal*, **2014**, *9*, 1099-1107.

[35] Stals, P. J. M.; Gillissen, M. A. J.; Paffen, T. F. E.; de Greef, T. F. A.; Lindner, P.; Meijer, E. W.; Palmans, A. R. A.; Voets, I. K. Folding Polymers with Pendant Hydrogen Bonding Motifs in Water: The Effect of Polymer Length and Concentration on the Shape and Size of Single-Chain Polymeric Nanoparticles. *Macromolecules*, **2014**, *47*, 2947-2954.

[36] Hosono, N.; Palmans A. R. A.; Meijer, E. W. "Soldier–Sergeant–Soldier" triblock copolymers: revealing the folded structure of single-chain polymeric nanoparticles. *Chemical Communications*, **2014**, *50*, 7990-7993.

[37] Huerta, E.; van Genabeek, B.; Stals, P. J. M.; Meijer, E. W.; Palmans, A. R. A. A modular approach to introduce function into single-chain polymeric nanoparticles. *Macromolecular Rapid Communications*, **2014**, *35*, 1320-1325.

[38] Wang, F.; Pu, H.; Jin, M.; Pan, H.; Chang, Z.; Wan, D.; Du, J. From single-chain folding to polymer nanoparticles via intramolecular quadruple hydrogen-bonding interaction. *Journal of Polymer Science, Part A: Polymer Chemistry*, **2015**, *53*, 1832-1840.

[39] Appel, E. A.; Dyson, J.; del Barrio, J.; Walsh, Z.; Scherman, O. A. Formation of Single-Chain Polymer Nanoparticles in Water through Host-Guest Interactions. *Angewandte Chemie, International Edition*, **2012**, *51*, 4185-4189.

[40] Wang, F.; Pu, H.; Che, X. Voltage-responsive single-chain polymer nanoparticles via host–guest interaction. *Chemical Communications*, **2016**, *52*, 3516-3519.

[41] Murray, B. S.; Fulton, D. A. Dynamic Covalent Single-Chain Polymer Nanoparticles. *Macromolecules*, **2011**, *44*, 7242-7252.

[42] Tuten, B. T.; Chao, D.; Lyon, C. K.; Berda, E. B. Single-chain polymer nanoparticles via reversible disulfide bridges. *Polymer Chemistry*, **2012**, *3*, 3068-3071.

[43] Song, C.; Li, L.; Dai, L.; Thayumanavan, S. Responsive single-chain polymer nanoparticles with host–guest features. *Polymer Chemistry*, **2015**, *6*, 4828-4834.

[44] Sanchez-Sanchez, A.; Fulton, D. A.; Pomposo, J. A. pH-responsive single-chain polymer nanoparticles utilising dynamic covalent enamine bonds. *Chemical Communications*, **2014**, *50*, 1871-1874.

[45] Wedler-Jasinski, N.; Lueckerath, T.; Mutlu, H.; Goldmann, A. S.; Walther, A.; Stenzel, M. H.; Barner-Kowollik, C. Dynamic covalent single chain nanoparticles based on hetero Diels-Alder chemistry. *Chemical Communications*, **2017**, *53*, 157-160.

[46] He, J.; Tremblay, L.; Lacelle, S.; Zhao, Y. Preparation of polymer single chain nanoparticles using intramolecular photodimerization of coumarin. *Soft Matter*, **2011**, *7*, 2380-2386.

[47] Frank, P. G.; Tuten, B. T.; Prasher, A.; Chao, D.; Berda, E. B. Intra-Chain Photodimerization of Pendant Anthracene Units as an Efficient Route to Single-Chain Nanoparticle Fabrication. *Macromolecular Rapid Communications*, **2014**, *35*, 249-253.

[48] Mavila, S.; Diesendruck, C. E.; Linde, S.; Amir, S.; Shikler, R.; Lemcoff, N. G. Polycyclooctadiene Complexes of Rhodium (I): Direct Access to Organometallic Nanoparticles. *Angewandte Chemie International Edition*, **2013**, *52*, 5767-5770.

[49] Sanchez-Sanchez, A.; Arbe, A.; Colmenero, J.; Pomposo, J. A. Metallo-Folded Single-Chain Nanoparticles with Catalytic Selectivity. *ACS Macro Letters*, **2014**, *3*, 439-443.

[50] Sanchez-Sanchez, A.; Arbe, A.; Kohlbrecher, J.; Colmenero, J.; Pomposo, J. A. Efficient Synthesis of Single-Chain Globules Mimicking the Morphology and Polymerase Activity of Metalloenzymes. *Macromolecular Rapid Communications*, **2015**, *36*, 1592-1597.

[51] Basasoro, S.; Gonzalez-Burgos, M.; Moreno, A. J.; Lo Verso, F.; Arbe, A.; Colmenero, J.; Pomposo, J. A. A Solvent-Based Strategy for Tuning the Internal Structure of Metallo-Folded Single-Chain Nanoparticles. *Macromolecular Rapid Communications*, **2016**, *37*, 1060-1065.

[53] Jeong, J.; Lee, Y.-J.; Kim, B.; Kim, B.; Jung, K.-S.; Paik, H.-J. Colored single-chain polymeric nanoparticles via intramolecular copper phthalocyanine formation. *Polymer Chemistry*, **2015**, *6*, 3392-3397.

[54] Willenbacher, J.; Altintas, O.; Trouillet, V.; Knöfel, N.; Monteiro, M. J.; Roesky, P. W.; Barner-Kowollik, C. Pd-complex driven formation of single-chain nanoparticles. *Polymer Chemistry*, **2015**, *6*, 4358-4365.

[55] Mavila, S.; Rozenberg, I.; Lemcoff, N. G. A general approach to mono- and bimetallic organometallic nanoparticles. *Chemical Science*, **2014**, *5*, 4196-4203

[56] Wang, F.; Pu, H.; Jin, M.; Wan, D. Supramolecular Nanoparticles via Single-Chain Folding Driven by Ferrous Ions. *Macromolecular Rapid Communications*, **2016**, *37*, 330-336.

[57] Lu, J.; ten Brummelhuis, N.; Weck, M. Intramolecular folding of triblock copolymers via quadrupole interactions between poly(styrene) and poly(pentafluorostyrene) blocks. *Chemical Communications*, **2014**, *50*, 6225-6227.

[58] Fisher, T. S.; Schulze-Sünninghausen, D.; Luy, B.; Altintas, O.; Barner-Kowollik, C. Stepwise Unfolding of Single-Chain Nanoparticles by Chemically Triggered Gates. *Angewandte Chemie International Edition*, **2016**, *55*, 11276-11280.

[59] Pomposo, J. A.; Perez-Baena, I.; Lo Verso, F.; Moreno, A. J.; Arbe, A.; Colmenero, J. How Far Are Single-Chain Polymer Nanoparticles in Solution from the Globular State? *ACS Macro Letters*, **2014**, *3*, 767-772.

[60] Fetters, L. J.; Hadjichristidis, N.; Lindner, J. S.; Mays, J. W. Molecular Weight Dependence of Hydrodynamic and Thermodynamic Properties for Well-Defined Linear Polymers in Solution. *The Journal of Physical Chemistry*, **1994**, *23*, 619-640.

[61] Pomposo, J. A.; Perez-Baena, I.; Buruaga, L.; Alegría, A.; Moreno, A. J.; Colmenero, J. On the Apparent SEC Molecular Weight and Polydispersity Reduction upon Intramolecular Collapse of Polydisperse Chains to Unimolecular Nanoparticles. *Macromolecules*, **2011**, *44*, 8644-8649.

[62] Rubinstein, M.; Colby, R. H. Polymer Physics. *Oxford University Press*, **2003**.

[63] Moreno, A. J.; Lo Verso, F.; Sanchez-Sanchez, A.; Arbe, A.; Colmenero, J.; Pomposo, J. A. Advantages of Orthogonal Folding of Single Polymer Chains to Soft Nanoparticles. *Macromolecules*, **2013**, *46*, 9748-9759.

CHAPTER 6

Completely deuterated SCNPs: synthesis and impact of intramolecular cross-linking

6.1. Introduction

As we discussed in Chapter 1, soft matter is characterized by complexity in structure and dynamics. In this regard, scattering techniques constitute powerful tools to unravel the structural and dynamic properties of soft matter systems, including SCNPs [1]. The momentum transfer dependence of the measured magnitudes can provide spatial and time resolution, which can be tuned by choosing the proper probe and/or experimental conditions. In particular, neutron scattering (NS) techniques provide two additional advantages for soft matter investigations: i) the possibility to match –simultaneously– the right length and time scales, and ii) the possibility to label selectively the components of a complex material *via* deuterium labeling [2-8]. An illustrative example of the importance of deuterium labeling in polymeric systems were the pioneering experiments on labeled polymer melts performed in the 1970s [9,10] -as soon as the first small angle neutron scattering (SANS) instruments were developed- providing experimental evidence for the random coil conformation of linear macromolecules in bulk, as originally proposed by Flory [11].

Polymers also show interesting features that make them good candidates for numerous industrial applications. In this respect, the chance discovery of vulcanization by Goodyear in 1839 probably constituted the most revolutionary event in the history of polymer industry. In the vulcanization process, the creation of a relatively small amount of cross-links between different entangled macromolecular chains leads to a permanent 3-D network with an associated spectacular transformation of the macroscopic properties of the material, from a (peculiar) liquid to a solid-like behaviour. Though this accomplishment was merely originated by chance, it is clear that the basic

understanding of the structural and dynamical features of materials at different length scales and their interrelation is the only rational way to design materials with tailored properties. With respect to SCNP-based materials, one fundamental question is: What is the impact of the chain topology on the properties and, in particular, how does it behave when cross-links are of purely intra-molecular character, as in the case of SCNPs?

Although the suitability of NS techniques to address these intriguing questions is beyond doubt, access to full perdeuterated functional polymer precursors to produce completely-deuterated single-chain nanoparticles (dSCNPs) for NS has been limited by the fact that most of the functional monomers as well as reactive cross-linkers currently in use are not commercially available in their deuterated version. Even with this severe limitation, NS studies with partially-deuterated SCNPs have proven: i) the "crumple-globule"-like conformation of SCNPs when embedded in a linear polymeric matrix [12,13], ii) the SCNP induced matrix entanglement dilution in a polymer nanocomposite [14], and iii) the confined dynamics of a low-*T*g polymer in the matrix of a nanocomposite rich in SCNPs, even at temperatures where the latter are above their *T*g [15]. However, deploying the full possibilities of the NS techniques for investigating the structure and dynamic features of SCNPs -as model macromolecules to address the effect of chain topology on materials properties- has been constrained by the absence of completely-deuterated single-chain nanoparticle samples.

6.2. Objectives

The aim of this work is to carry out an in-depth study on the impact of intramolecular cross-links on the properties of SCNP melts, which will be performed by combining a battery of experimental techniques including "macroscopic" (calorimetry, dielectric and

mechanical spectroscopy) and "microscopic" (quasielastic neutron scattering and small-angle neutron scattering) ones.

Prior to that, a novel synthetic route to produce completely-deuterated single-chain polymer nanoparticles (dSCNPs) needed for neutron scattering experiments was designed (Figure 6.1). It comprises: i) the use of commercially available perdeuterated cyclic ether monomers as starting reagents, ii) a ring-opening copolymerization process performed in bulk to produce a neat dSCNP precursor, iii) a standard azidation reaction to decorate this precursor with azide moieties, and iv) a facile intramolecular azide photodecomposition step carried out under UV irradiation at high dilution providing with highly-valuable, completely-deuterated soft nano-objects from the precursor.

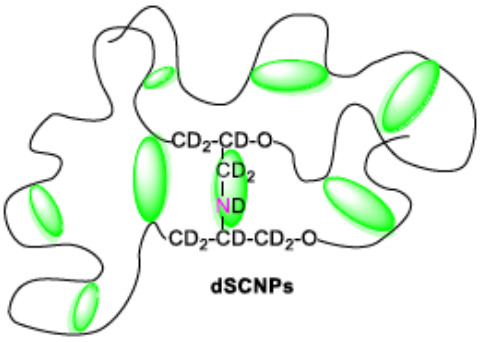

Figure 6.1. Illustration of the completely-deuterated SCNPs synthesized for this work.

6.3. Experimental part

6.3.1. Materials

Tetrahydrofuran (THF) (≥ 99.9 %, Scharlab) and epichlorohydrin (ECH) (99 %, Aldrich) were dried over CaH_2, degassed and distilled in a vacuum line prior to use. Tris(pentafluorophenyl)borane ($B(C_6F_5)_3$) (95 %, Aldrich) was sublimed at 60ºC in a

cold finger condenser. Tetrahydrofuran-d8 (THF-d8) (99.5 atom % D, Acros), epichlorohydrin-d5 (ECH-d5) (≥ 98 atom % D, Aldrich), dichloromethane (CH_2Cl_2) (reagent grade, Aldrich), *N*,*N*-dimethylformamide (DMF) (≥ 99.8 %, Scharlab), sodium azide (NaN_3) (≥ 99.5 %, Aldrich) and methanol (MeOH) (≥ 99.9 %, Scharlab) were used as received.

6.3.2. Synthesis of protonated and deuterated neat copolymers

All reactions were performed in bulk conditions under an argon atmosphere using Schlenk flasks. For the synthesis of the protonated copolymer (hCop), $B(C_6F_5)_3$ (20 mg, 0.04 mmol), THF (2.50 mL, 30.8 mmol) and ECH (0.63 mL, 8.1 mmol) were mixed in a 25 mL Schlenk flask and stirred at room temperature for 48 h. The resulting crude product was precipitated in cold MeOH, yielding a sticky transparent copolymer (hCop: 1.75 g, 59 % yield, Mw = 33.2 kDa, $Đ$ = Mw/Mn = 1.55). The ECH content in hCop was estimated to be 30 mol % (see Table 6.1). A similar procedure was followed for the synthesis of the deuterated sample (dCop). Hence, $B(C_6F_5)_3$ (72 mg, 0.14 mmol), THF-d8 (8.4 mL, 103 mmol) and ECH-d5 (1.8 mL, 23 mmol) were used to obtain the completely-deuterated copolymer (dCop: 5.61 g, 53 % yield, Mw = 36.8 kg/mol, $Đ$ = 1.23).

6.3.3. Azidation of the protonated and deuterated copolymers to obtain the precursors

In a typical azidation procedure, 1.0 g of hCop was dissolved in DMF (40 mL) in a round bottom flask. NaN_3 (330 mg, 2 eq.) was added and the mixture was left stirring for 24 h at 60ºC. Elemental analysis revealed an azidation degree of 17 % (see Table 6.1). The crude product was precipitated in a 1:1 H_2O/MeOH mixture and dried at 50 ºC

under reduced pressure in a vacuum oven to yield the azide-containing protonated precursor (hPrec: 0.85 g, 85 % yield). The same procedure was followed to obtain the azide-decorated deuterated precursor (dPrec: 0.82 g, 82 % yield).

6.3.4. Synthesis of protonated and completely-deuterated single-chain nanoparticles

Single-chain nanoparticles were synthesized *via* intramolecular azide photodecomposition. In a typical procedure, 100 mg of precursor (hPrec or dPrec) were dissolved in distilled THF (100 mL, 1 mg/mL) in a vial covered with aluminium foil, and exposed to UV irradiation (λ = 300-400 nm) for 3 h at room temperature. The solvent was evaporated at reduced pressure and the resulting product was redissolved with CH_2Cl_2 (≈ 0.5 mL) and precipitated in cold MeOH. SCNPs (hSCNP or dSCNP) were obtained as yellowish viscous liquids (≈ 90 % yield in both cases). Elemental analysis of hSCNP revealed an azide decomposition degree of ≈ 50 % (see Table 6.1).

Table 6.1. EA results of hCop, hPrec and hSCNPs.

Sample	C(%) exp.	C(%) calc.	H(%) exp.	H(%) calc.	N(%) exp.	N(%) calc.
hCop	56.5	56.8	9.0	9.1	-	-
hPrec	57.7	56.6	8.9	9.0	2.80	2.7
hSCNPs	55.8	57.1	8.7	9.1	1.84	1.8

According to the EA data of Table 6.1 the molecular compositions of hCop and hPrec are, respectively, as follow:

Poly[$(C_4H_8O)_{0.7}$-*co*-$(C_3H_5OCl)_{0.3}$]

$$Poly[(C_4H_8O)_{0.7}\text{-}co\text{-}(C_3H_5OCl)_{0.25}\text{-}co\text{-}(C_3H_5ON_3)_{0.05}]$$

And the molecular compositions of SCNPs:

Units not involved in cross-linking

$$Poly[(C_4H_8O)_{0.7}\text{-}co\text{-}(C_3H_5OCl)_{0.25}\text{-}co\text{-}(C_3H_5ON_3)_{0.025}]$$

Units not involved in cross-linking

$$(C_3H_5ON)_{0.025}$$

According to the EA data, the azidation degree of hPrec is 0.05/(0.25+0.05) ≈ 0.17 (17 %) and the degree of azide functional groups involved in intrachain cross-linking is 0.025/(0.025+0.025) = 0.5 (50 %).

6.4. Results and discussion

6.4.1. Synthesis of completely-deuterated SCNPs

Scheme 6.1 illustrates the new synthetic route towards completely-deuterated single-chain nanoparticles (dSCNPs) *via* intramolecular azide photodecomposition.

As an initial validation experiment, we first confirmed the successful formation of protonated single-chain nanoparticles (hSCNPs) following the synthetic pathway displayed in Scheme 6.1. Hence, we prepared a neat polyether copolymer by ring-opening copolymerization in bulk at room temperature of tetrahydrofuran and epichlorohydrin initiated by $B(C_6F_5)_3$ [16], which was subsequently azidated with NaN_3 in DMF to produce the protonated functionalized precursor (hPrec: *M*w = 33.2 kDa, *Đ* = 1.55, azidation degree = 17%).

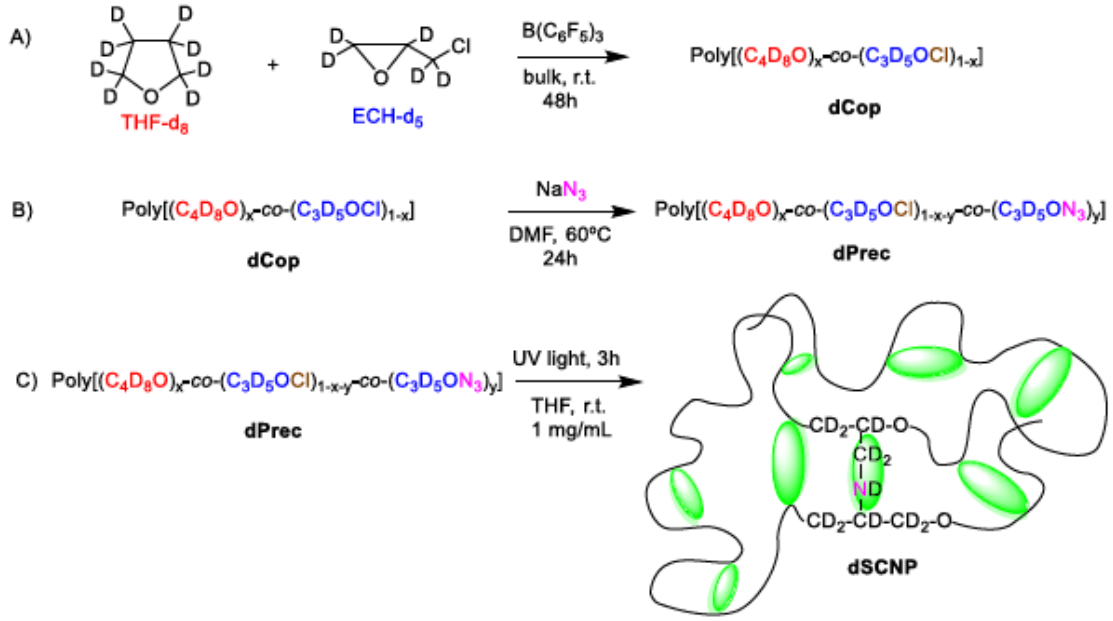

Scheme 6.1. Route towards completely-deuterated single-chain polymer nanoparticles (dSCNPs) *via* intramolecular azide photodecomposition: A) Ring-opening copolymerization in bulk at room temperature of perdeuterated tetrahydrofuran (THF-d_8) and perdeuterated epichlorohydrin (ECH-d_5) initiated by $B(C_6F_5)_3$ to give a neat deuterated copolymer (dCop). B) Azidation of dCop in DMF to produce a deuterated, azide-decorated precursor (dPrec). C) UV irradiation (λ = 300-400 nm) of dPrec at high dilution to promote intra-chain cross-linking *via* insertion reactions upon azide photodecomposition.

UV irradiation of hPrec at high dilution in THF (1 mg/mL) for 3 h produced hSCNPs, as revealed by size exclusion chromatography (SEC) experiments. As illustrated in Figure 6.2A, hSCNPs showed a smaller average hydrodynamic size (longer retention time at the SEC peak maximum) when compared to that of hPrec. The size reduction observed is a consequence of chain compaction *via* intra-chain cross-linking [17]. The disappearance of the azide functionality from hPrec upon UV irradiation -presumably *via* nitrene formation accompanied by evolution of N_2- [18] was investigated through infrared (IR) (see Figure 6.2B) and elemental analysis (EA) measurements. On average, 50% of the azide functional groups were involved in the intra-chain cross-linking process as determined by EA (see Table 6.1). We attribute the chain compaction observed by SEC to intra-chain cross-linking reactions –*via* N-H insertion reactions–

involving highly reactive nitrene species having high tendency to react through many different pathways [18].

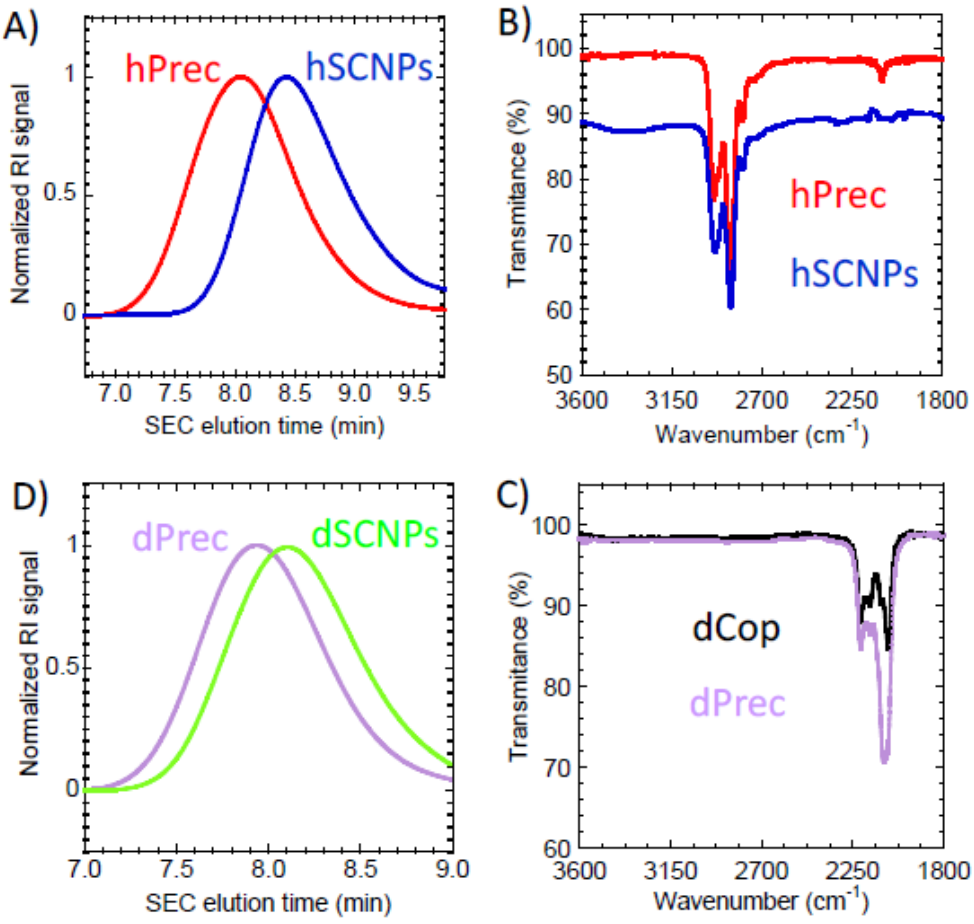

Figure 6.2. A) SEC chromatograms of hPrec and hSCNPs showing the shift of the SEC retention peak of hPrec upon chain compaction *via* intramolecular azide photodecomposition to produce hSCNPs. B) IR spectra of hPrec and hSCNPs illustrating the reduction of the intensity of the azide vibration band of hPrec (*ca.* 2100 cm^{-1}) upon UV irradiation. C) FTIR spectra of dCop and dPrec showing the absence of C-H vibration bands in the 2650-2950 cm^{-1} region, which confirms the high content of deuterium in both dCop and dPrec. D) SEC chromatograms of dPrec and dSCNPs, supporting the reduction in hydrodynamic size (increase in SEC retention time) upon dSCNP formation *via* intramolecular azide photodecomposition.

Having confirmed the successful formation of polyether hSCNPs *via* intramolecular azide photodecomposition, we attempted the synthesis of completely-deuterated single-chain nanoparticles (dSCNPs) following Scheme 6.1 by starting with commercially

available deuterated cyclic ether monomers (THF-d8 and ECH-d5). A batch of neat completely-deuterated polyether copolymer (dCop: Mw = 36.8 kDa, $Đ$ = 1.23) was successfully obtained in a gram-scale synthesis (> 5 g). Confirmation of the high content of deuterium in dCop was obtained from Fourier transform infrared spectroscopy (FTIR) as illustrated in Figure 6.2C, where the absence of intense C-H vibration bands in the 2650-2950 cm^{-1} region is observed in the FTIR spectrum of dCop. Instead, intense C-D vibration bands in the 2240-2040 cm^{-1} range are clearly visible in Figure 6.2C, as expected for a completely-deuterated polyether copolymer [19]. After azidation of dCop to give a completely-deuterated azide-decorated precursor (dPrec), the successful formation of dSCNPs from dPrec *via* intramolecular azide photodecomposition was confirmed through SEC measurements, as illustrated in Figure 6.2D. It is worth of mention that for dPrec, the relatively weak azide IR vibration band located at ≈ 2100 cm^{-1} overlaps with the strong C-D vibration bands placed in the 2240-2040 cm^{-1} region (see Figure 6.2C) so this fact prevents to follow the disappearance of the azide functionality by FTIR spectroscopy during the dSCNPs formation process. In this case, ^{13}C nuclear magnetic resonance (NMR) spectroscopy results allowed us to confirm that azide decomposition takes place upon UV irradiation of dPrec (see Fig. 6.3). More importantly, dSCNPs were found to display a high deuterium purity by FTIR spectroscopy (absence of C-H and N-H vibration peaks, see Fig. 6.4) as well as by neutron scattering experiments (see Fig. 6.5) suggesting that the intra-chain cross-linking process was not affected by the presence of the protonated solvent used during the synthesis. The resulting dSCNPs were found to be non-crystalline materials with a value of glass transition temperature of -75 ºC, as determined by differential scanning calorimetry (DSC) (see Fig. 6.6).

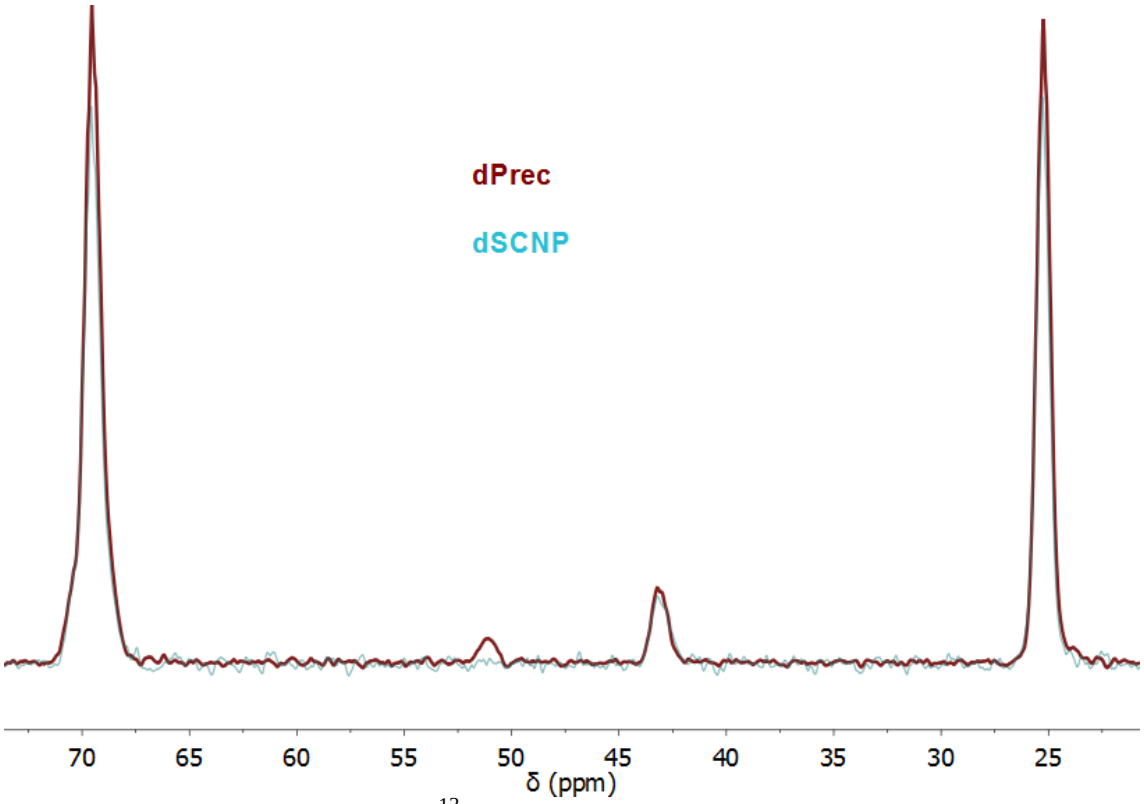

Figure 6.3. Comparison of the ^{13}C NMR spectra of dPrec and dSCNPs showing a significant reduction in intensity of the peak associated to the carbon atom next to the azide functionality of dPrec (–**C**D_2–N_3, 51 ppm) upon formation of dSCNPs *via* UV irradiation.

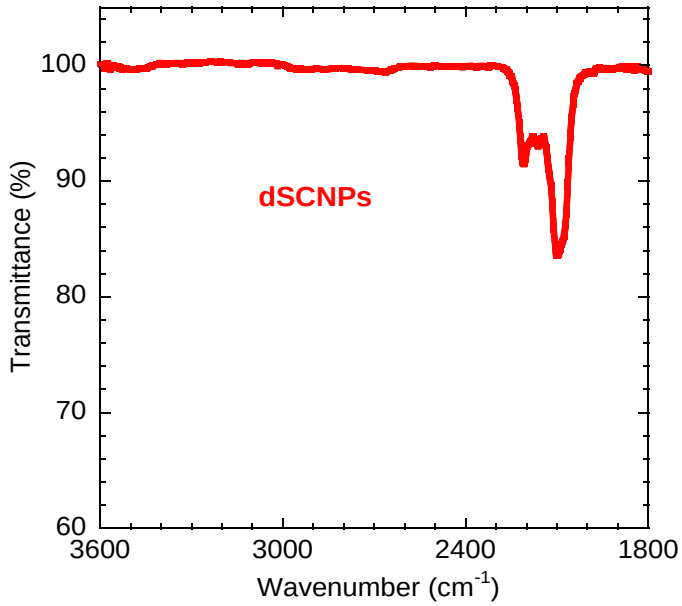

Figure 6.4. FTIR spectrum of dSCNPs showing the absence of intense vibration bands above 2240 cm^{-1}.

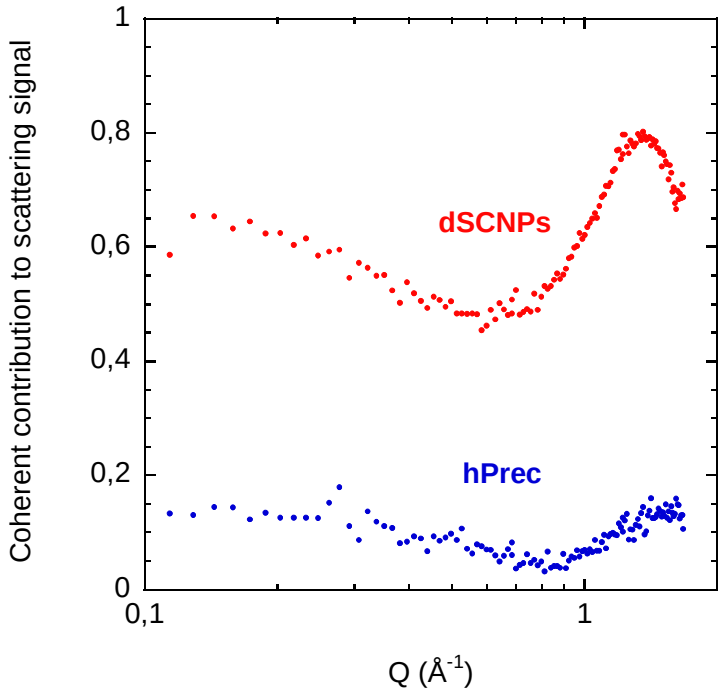

Figure 6.5. Fraction of the coherent scattering signal for dSCNPs as determined by polarization NSE measurements. dSCNPs show a large coherent contribution characteristic of deuterated samples, whereas scattering of protonated samples (*e.g.*, hPrec) was found to be mostly incoherent.

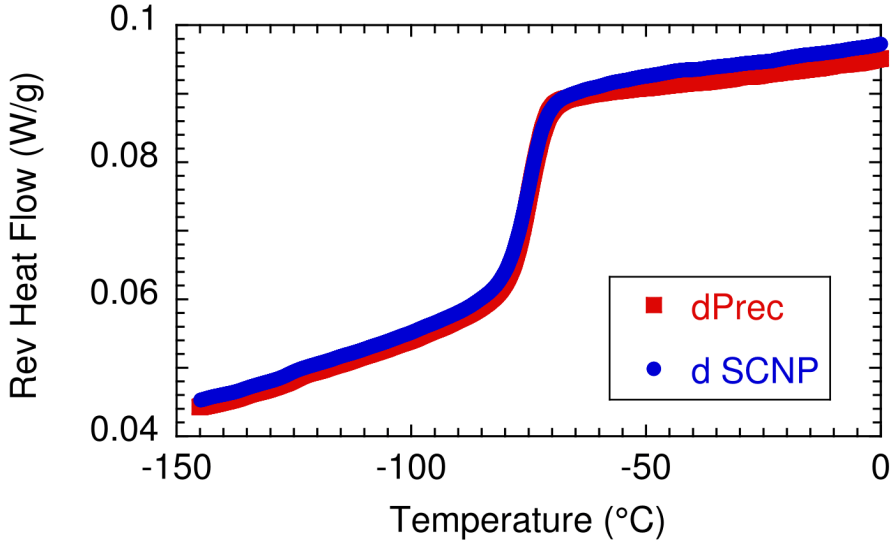

Figure 6.6. Reversible heat flow as a function of temperature measured with DSC by cooling for dPrec and dSCNPs. The value of the mid-point glass transition temperature, T_g, is found to be -75 ºC.

6.4.2. Impact of intra-molecular cross-linking

We first present the reference results on the bulk of linear precursor chains. QENS on the protonated sample reveals the usual dispersive features found for the hydrogen motions in glass-forming polymers in the supercooled liquid state, which can be well described assuming an anomalous jump diffusion mechanism (AJD). Figure 6.7 shows QENS results after Fourier transformation into the time domain and deconvolution from instrumental resolution.

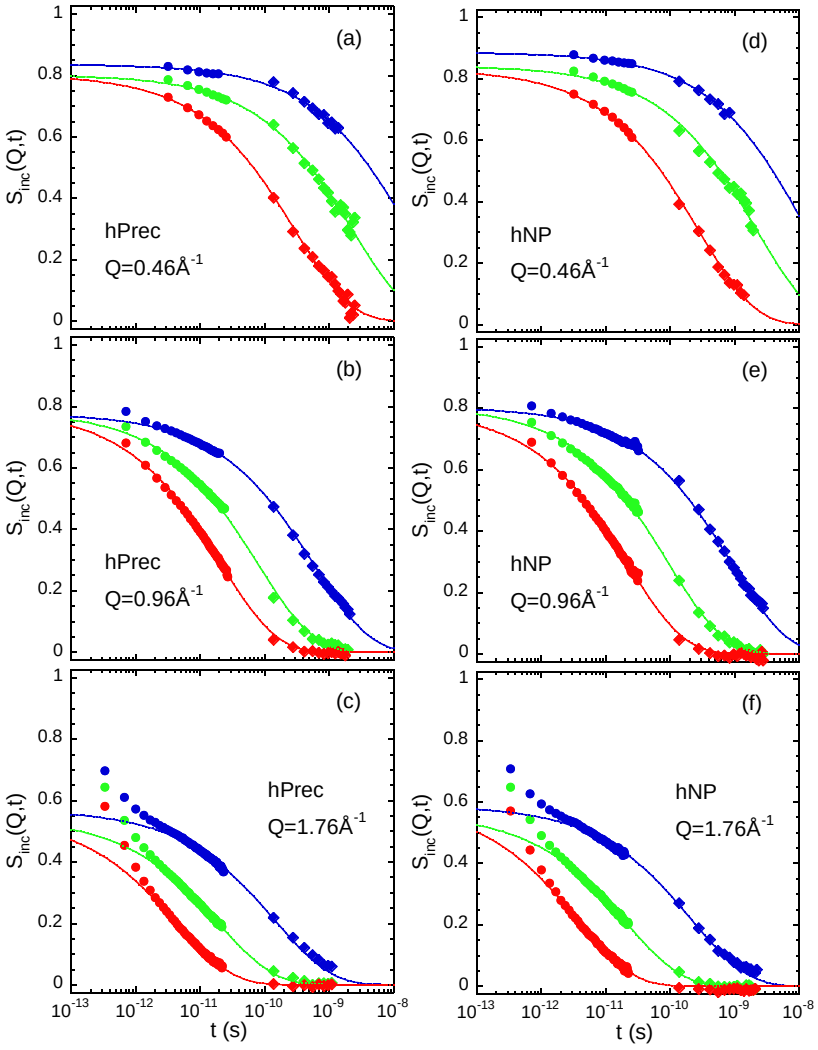

Figure 6.7. Fourier transform and deconvoluted QENS spectra obtained from FOCUS (circles) and SPHERES (diamonds) results on the hPrec (a,b,c) and hNP (d,e,f) samples, and the three temperatures investigated: 285 K (blue), 320 K (green) and 360 K (red). The Q-values correspond to 0.46 $Å^{-1}$ (a,d), 0.96 $Å^{-1}$ (b,e) and 1.76 $Å^{-1}$ (c,f). Solid lines are KWW fits with $\beta \equiv 0.5$ to the results above 2 ps.

The panels on the left correspond to the hPrec sample, and on the right to the hNP sample. FOCUS (circles) and SPHERES (diamonds) data are combined. As it is commonly found in glass-forming polymers above Tg [20], the results on protonated samples –corresponding to the intermediate incoherent scattering functions of the hydrogens- can be well described above ≈ 2 ps by means of a Kohlrausch-Williams-Watts (KWW) or stretched exponential functional form

$$S_{inc}(Q,t) \propto \exp\left[-\left(\frac{t}{\tau_s}\right)^{\beta}\right] \quad (6.1)$$

with a stretching exponent β close to 0.5. This is the parameter imposed in the fits of the results shown in Figure 6.7. The average characteristic time for H self-motions $\langle\tau\rangle = \tau_s^H \Gamma(1/\beta)/\beta$, represented in Figure 6.8, shows a strong dispersion in Q, being well approximated by a power law $\langle\tau\rangle \propto Q^{-\left(\frac{2}{\beta}\right)}$ in the approximate Q-range Q ≤ 1 Å^{-1}.

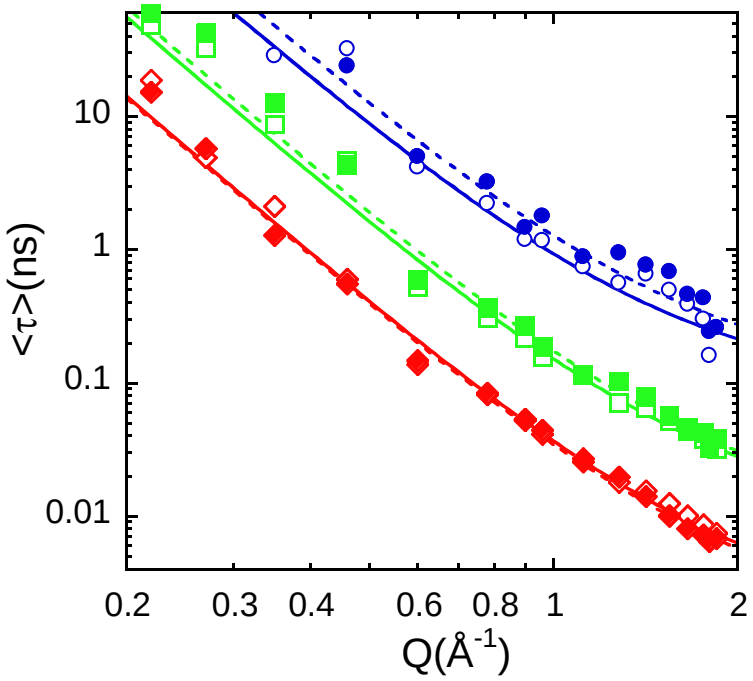

Figure 6.8. Scattering vector dependence of the average characteristic time $\langle\tau\rangle = \tau_s^H \Gamma(1/\beta)/\beta$ for H-self motions obtained for hPrec (empty symbols) and hNP (filled symbols) at 285 K (blue circles), 320 K (green squares) and 360 K (red diamonds), imposing β = 0.5 (fits shown in Figure 6.7). Lines are fits of Equation 6.1 to the hPrec (solid lines) and hNP (dotted lines) results.

This relation between dispersion and stretching is indicative for Gaussian diffusive behavior with an associated sublinear increase of the mean squared atomic displacement [21]. Deviations from this asymptotic law at higher Q-values can usually well be accounted for by assuming a distribution of local jumps as the underlying microscopic mechanism for such an anomalous diffusion, which can be resolved by the QENS experiments when exploring small enough length scales [22, 23]. In the framework of the anomaouls jump diffusion (AJD) model, based on these ideas, the characteristic time for the self-correlation function can be expressed as:

$$\tau_s(Q) = \tau_s \left[1 + \frac{1}{Q^2 \ell_0^2}\right]^{\frac{1}{\beta}} \quad (6.2)$$

Here, ℓ_o is the preferred jump length. The resulting values of the parameters involved in the description by this model are collected in Table 6.2. Note that in this case, the hydrogen dynamics is what it is followed by the experiments and consequently the obtained parameters correspond to these particular nuclei.

Table 6.2. Values of the parameters involved in the AJD fitting the hPrec results described with KWW functions with β = 0.5.

T(K)	$\langle \tau_{s,o}^{H} \rangle (ps)$	ℓ_o(Å)
285	82	0.64
320	9.4	0.58
360	1.7	0.53

The Fourier transformed QENS results on the hNPs sample are nearly indistinguishable from those on hPrec, as can be appreciated from Figures 6.7 and 6.8, and the values of the AJD parameters used to fit the characteristic times, shown in Table 6.3.

Table 6.3. Values of the parameters involved in the AJD fitting the hNP results described with KWW functions with β = 0.5.

T(K)	$\langle \tau_{s,o}^{H} \rangle (ps)$	ℓ_o(Å)
285	103	0.63
320	9.8	0.56
360	1.5	0.51

Moving to the neutron results on the deuterated sample, as can be seen in Figure 6.9A, the structure factor S(Q) -static limit of the dynamic structure factor S(Q, t)- presents a well-defined amorphous halo centered at around Q_{max} = 1.4 $Å^{-1}$. In main-chain polymers, this peak can usually be attributed to correlations between atoms belonging to nearest neighbor chains [24], separated by an average inter-chain distance of about d ≈ $2\pi/Q_{max}$. Here, d ≈ 4.5 Å. The squares in Figure 6.10 show the NSE results on the normalized S(Q, t) at Q_{max}, i. e., revealing the temporal evolution of such inter-chain correlations. The curves can be well described by Kohlrausch-Williams-Watts (KWW) functions with a value of the stretching exponent β ≈ 0.5. Applying Equation 6.1 to all NSE results the characteristic times shown in Figure 6.9B were obtained. At high Qs, they show a kind of maximum reminiscent of the deGennes narrowing proposed for simple diffusion [25].

Approaches merely based on diffusive mechanisms predict a continuous slowing down with decreasing scattering vector in the Q → 0 limit. Therefore, they obviously fail in reproducing the experimentally observed acceleration of the collective dynamics at intermediate length scales (ILS). The ILS region corresponds to length scales larger than the typical intermolecular distances but not yet in the hydrodynamic regime. Around a given Q_c-value located in the ILS region, the collective response of glass-

forming systems crosses over from being dominated by diffusion to a region where it is dominated by the viscoelastic coupling of stress and density fluctuations.

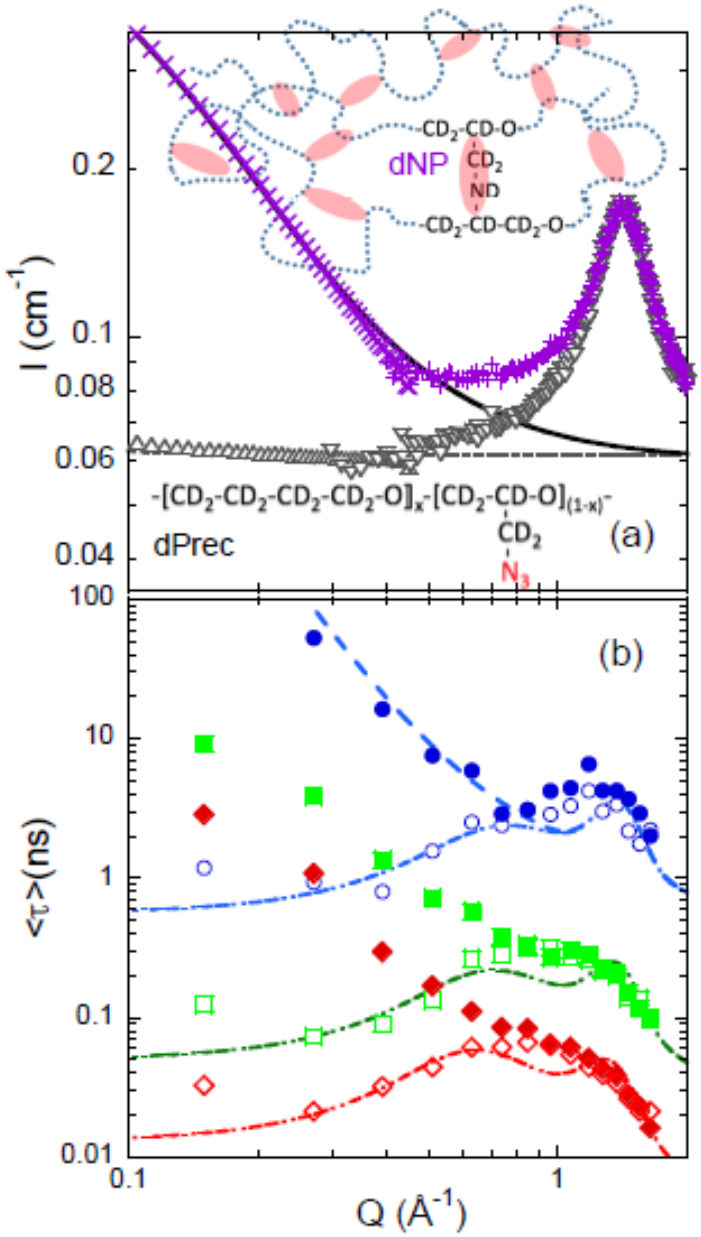

Figure 6.9. (a) Differential cross section of dPrec (up-triangles: D11; down-triangles: FOCUS) and dNP (crosses: D11; pluses: FOCUS). Dotted line marks its value for dPrec at ILS, and the solid line includes an Ornstein-Zernike contribution accounting for the scattering excess observed in dNP. (b) Q-dependence of the average collective characteristic times $\langle\tau\rangle = \Gamma\left(\frac{1}{\beta}\right)\tau_w/\beta$ determined from the NSE experiments (empty symbols: dPrec; filled symbols: dNP) at 280 K (circles, β = 0.43), 320 K (squares, β = 0.47) and 360 K (diamonds, β = 0.55). The dashed-dotted lines are descriptions of the collective times for the precursor in terms of an (anomalous jump) diffusive component (shown as the dashed line for the 280 K case) and a Q → 0 component affected by a cutoff factor.

Only beyond a certain length scale -somehow related with Q_c- the system would appear as viscoelastically homogeneous. This crossover is captured by a recently proposed model [26], which application provides the lines shown in Figure 6.9B. For the precursor melt, $Q_c \approx 0.6$ Å^{-1}.

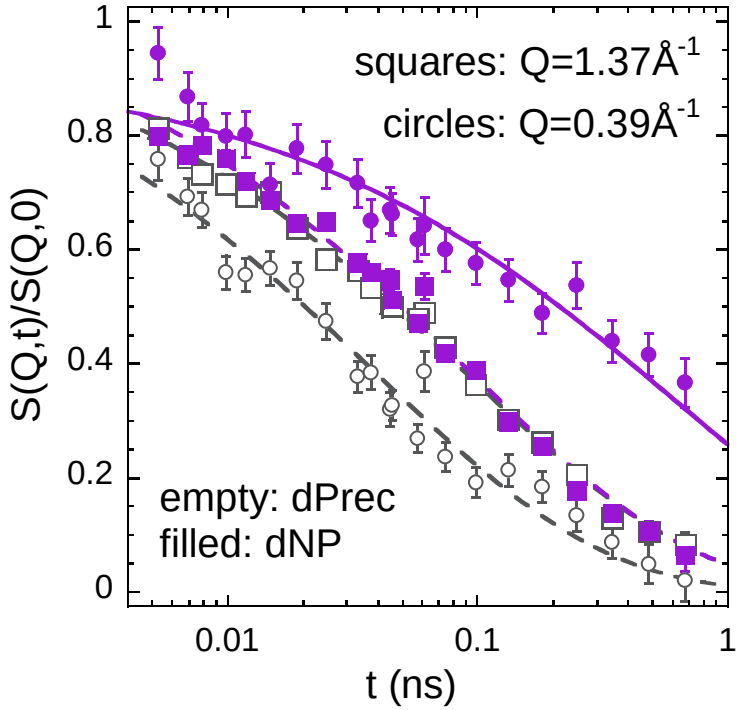

Figure 6.10. Normalized dynamic structure factor measured by IN11c at $Q \approx Q_{max}$ (squares) and at $Q = 0.39$ Å^{-1} (circles) -i. e., in the ILS region- on dPrec (empty symbols) and on dNP (filled symbols) at 320 K. Lines are fits of stretched exponentials to the precursor (dashed lines) and the dSCNPs sample (solid lines) with $\beta = 0.47$.

Given the adscription of the correlations at Q_{max} as those between atoms located in adjacent chains, it is clear that NSE experiments at Q_{max} reveal the genuine structural α-relaxation. To monitor this process in a wider range, dielectric spectroscopy measurements were employed. Figure 6.11A shows the decomposition of the dielectric loss of the precursor bulk at approx. T_g + 20 K into an α- and a β-contribution. Their corresponding characteristic times are represented in Figure 6.12. The values of the α-relaxation times obtained from DS are higher than those observed by NSE at Q_{max}, suggesting large dipolar correlations in this sample.

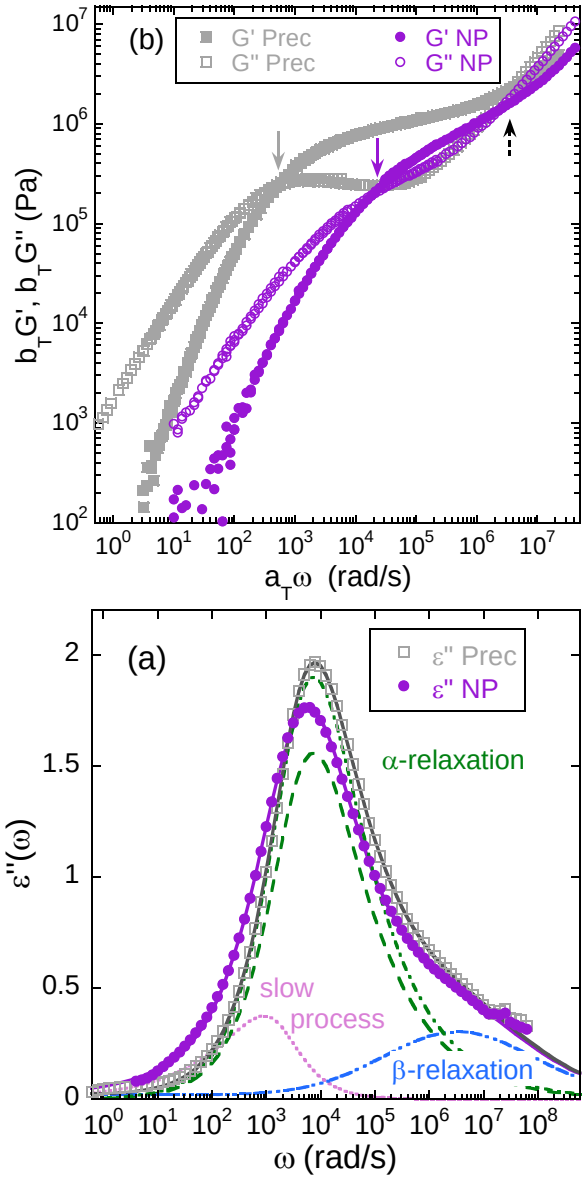

Figure 6.11. (a) Dielectric losses at 220 K. The conductivity contribution has been subtracted. Solid lines are fitting curves obtained by the addition of a β-relaxation (blue dashed-dotted line), an α-relaxation (green lines), and an additional slow contribution (pink dotted line) in the case of the SCNPs. (b) Master curves obtained from rheological experiments using the shift factors and amplitudes shown in the inset with a reference temperature of 293 K. The lines correspond to VF-fits. The dashed arrow indicates the common entanglement and the solid arrows the disentanglement reduced frequencies.

Last, the master curves obtained for the real and imaginary parts of the shear modulus of the precursor melt are presented in Figure 6.11B, as results from rheological measurements performed by Dr. Paula Malo de Molina. As it is typical for long linear macromolecules, they cross at two points: that at high frequencies reflects the onset of

entanglement effects on the mechanical response and that at low frequencies is the signature of the disentanglement of the chains. The separation of these two points increases with the length of the macromolecules. In between, the reptation mechanism associated to the topological constraints imposed by neighboring chains (‘entanglements’) prevails, leading to a ‘soft-solid like’ behavior.

We now move to the bulk made of SCNPs, commencing with the macroscopic studies. The impact on the rheological properties is striking, as can be realized from Figure 6.11B. Intramolecular crosslinks produce a strong shift of the disentanglement point to higher frequencies -accordingly, a huge decrease of the disentanglement time. The plateau in the shear modulus practically dissapears in the SCNPs bulk. This system does not show a ‘solid-like’ behavior anymore, but readily flows. The difference with respect to the intermolecular cross-linking impact on the rheological properties {persistent low-frequency plateaus reflecting the permanent 3D-network structure [27] is dramatic.

The influence of the induced topology on the DS results consists of a broadening of the main loss dielectric peak, mainly affecting its low-frequency flank, and a slight apparent shift of this maximum (see Figure 6.11A). To describe these results -that, a priori, are not obvious to reconcile with the rheological observation- we first consider the microscopic insight provided by neutron scattering.

The direct comparison of the original incoherent QENS spectra of both samples suggests a subtle retardation of the hydrogen motions in the SCNPs' bulk with respect to the precursors at low Q-values (large length scales); however, the usual analysis of the Fourier transformed and deconvoluted results, within the uncertainties, reveals hardly

distinguishable features for the self-dynamics in both melts. Moving to coherent scattering, Figure 6.9A shows that the amorphous halo of the SCNPs' bulk is exactly at the same position as that of the precursor chains. The average inter-molecular distances are thus not appreciable disturbed by internal cross-links. The collective motions involved in the structural relaxation as revealed by NSE in the neighborhood of Q_{max} take also place in a very similar way in the two melts. On the contrary, the decay of the S(Q,t) at ILS is dramatically slowed down in the presence of intra-molecular cross-links. These features are directly evidenced in Figure 6.10 and by the resulting characteristic times in Figure 6.9B. The latter tend to continuously increase toward larger length scales, reminding a diffusion dominated-like dynamics. In the above commented framework for collective dynamics at ILS, for the melt of SCNPs the crossover to a non-diffusive characteristic time at Q_c would be strongly shifted to low Q-values (even below those accessed by the IN11c window), implying that the SCNPs bulk would behave viscoelastically homogeneous only at extremely large length scales.

Is there any structural evidence for the existence of heterogeneities responsible for such dynamical behavior at ILS? SANS experiments provide the answer, showing indeed a pronounced increase of the forward scattering with respect to that in the precursor (see Figure 6.9A). Such an excess can be well accounted for by an Ornstein-Zernike expression, $I_{OZ} \propto 1/[1 + (Q\xi)^2]$, with a value of about 9 Å for the characteristic length ξ. The internal cross-links thus induce scattering length density fluctuations in the nanometric length scale, which relaxation takes place much more slowly than that driving the decay of density fluctuations at similar length scales in a melt of chemically identical chains with simple linear topology.

Since structural and dynamic properties at local and intermolecular length scales are practically insensitive to internal cross-linking, the functional forms and characteristic times of the dielectric β and α-processes of the SCNPs can be fixed to those determined from the precursor study. However, to describe the DS results in this way we have to assume that the amplitude of the α-peak is smaller in the SCNPs, i. e., that not all the polarization relaxes through this process, but only a fraction. Introducing this single free parameter, the relaxational contribution of the remaining fraction was deduced. Figure 6.11A illustrates the decomposition obtained for an intermediate temperature. The additional process has a maximum at lower frequencies than the α-peak, and is highly asymmetric. It accounts for the relaxation of about 15% of the polarization. The characteristic time of this slow process is also included in Figure 6.12. Interestingly enough, its temperature dependence can be perfectly described by that of the shift factors used in the construction of the rheological master curves of the SCNPs shown in Figure 6.11B.

Coarse-grained molecular dynamic simulations have revealed that intramolecular bonding produces an internal compartmentation of the macromolecule into loops (‘domains’) of diverse sizes [12, 28, 29]. The internal loops topology imprinted in the SCNPs would be at the origin of the acceleration of the terminal relaxation with respect to the precursor bulk -it is well known that macromolecular rings do not entangle with other rings [30]. The ability of the chains to flow at shorter times than in the entangled linear melt reflects the disability of entanglement formation provoked by the induced internal ring-like topology. On the other hand, close to the cross-links, chain conformation and packing could be expected to be slightly different than in the rest of the bulk material.

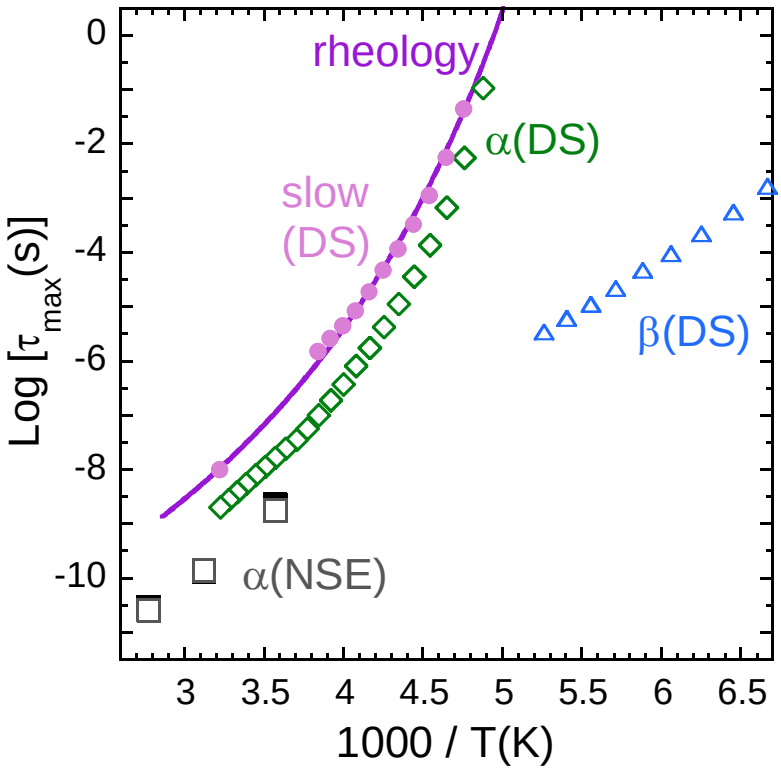

Figure 6.12. Inverse temperature dependence of the characteristic times obtained for the precursor (empty symbols) and the SCNPs (filled symbols) for the following processes: α- relaxation by NSE at Q_{max} (squares) and DS (diamonds), β-relaxation (triangles) and the slow DS-process (circles). The solid line represents the dependence obtained from the rheological experiments on the SCNPs (Figure 6.11B). The times correspond to the maxima of the imaginary part of the corresponding susceptibility function.

The resulting heterogeneities are reflected in the structure factor with nanometric characteristic length scale. Thus, topology introduces an additional relevant length scale in the problem. From a dynamic point of view, internal bonds are expected to impose an extra friction for relaxation of the neighboring segments. Such hindrance would provoke the retardation of the decay of density fluctuations at intermediate length scales with respect to the linear counterparts and would also be reflected through a slowly relaxing fraction of the polarization -the additional dielectric process observed would involve the relaxation of dipoles that are strongly influenced by the intramolecular cross-links and cannot fully participate in the α-relaxation. Only when the relaxation of such newly appeared correlations associated to rigid ‘domains’ are lost, the complete

chain relaxation leading to the viscous flow can take place. Thus, in the melt of SCNPs, the role played by the entanglements in melts of linear chains preventing the flow is overtaken by the internal domain structure imprinted by intramolecular cross-linking. Taking into account the tiny fraction of cross-links present along the chain, this system nicely illustrates the essence of soft materials: 'small cause, large effects' [31].

6.5. Conclusions

The first part of this work comprised an efficient procedure to produce completely-deuterated single-chain polymer nanoparticles (dSCNPs) based on the use of: i) commercially available perdeuterated cyclic ether monomers, ii) a simple bulk ring-opening copolymerization process, iii) a facile azidation post-polymerization functionalization reaction, and iv) an efficient UV-induced azide decomposition reaction at high dilution promoting intra-chain crosslinking reactions. By means of this new procedure, low-T_g, non-crystalline, polyether-based dSCNPs were prepared as highly-valuable, completely-deuterated soft nano-objects.

In the second part, an in-depth study of the effect of internal cross-linking was performed by combining a set of advanced experimental techniques. Neutron scattering demonstrated that the structural and dynamical properties at local length scales including the intermolecular distances (in particular, the structural relaxation) are hardly sensitive to chain topology. Its impact, as revealed by this microscropic technique, consists of a slowing down of collective dynamics occurring at larger length scales, associated to emerging structural heterogeneities with a characteristic length of about 1 nm. Macroscopically, a striking practically complete disappearance of the rubbery plateau was witnessed in the internally cross-linked melt -just the opposite effect to the

generation of a permanent solid-like structure provoked by ‘standard’ vulcanization. The dielectric spectra revealed an enhanced intensity in the frequency region below the α-relaxation loss peak. The combination of the results from all these experimental techniques has been crucial to elaborate a consistent picture of the effect of internal cross-links on the chain properties in a polymer melt. We suggest that the internal structure imprinted by intramolecular bonding consisting of intrachain loops prevents the formation of entanglements among macromolecules, accelerating the complete relaxation of the chains which leads to the viscous flow. However, the local globulation and internal compartmentation into domains induced by the cross-links introduce a new relevant mechanism for chain relaxation at intermediate length scales. This new emerging dynamics takes over the role of disentantanglement for full chain relaxation; therefore, the terminal regime and this slow relaxation at nanometric scale are intimately connected.

6.6. References

[1] Lindner, P.; Zemb, T. Neutrons, x-rays and light: scattering methods applied to soft condensed matter, *North Holland Delta Series*, **2002**.

[2] Springer, T. Quasielastic neutron scattering for the investigation of diffusive motions in solids and liquids. *Springer*, **1972**.

[3] Lovesey, S. W. Theory of neutron scattering from condensed matter. *Clarendon Press*, **1984**.

[4] Bée, M. Quasielastic neutron scattering. *Adam Hilger*, **1988**.

[5] Squires, G. L. Introduction to the theory of thermal neutron scattering. *Dover Publication Inc*, **1996**.

[6] Higgins, J. S.; Benoit, H. C. Polymers and neutron scattering, *Oxford University Press*, **1997**.

[7] Roe, R. J. Methods of X-Ray and neutron scattering in polymer science, *Oxford University Press*, **2000**.

[8] Gabrys, B. Applications of neutron scattering to soft condensed matter. *Gordon and Breach Science Publishers*, **2000**.

[9] Kirste, R. G.; Kruse, W. A.; Schelten, J. Die bestimmung des trägheitsradius von polymethyl-methacrylat im glaszustand durch neutronenbeugung. *Macromolecular Chemistry and Physics*, **1972**, *162*, 299-303.

[10] Benoit, H.; Cotton, J.; Decker, D.; Farnoux, B.; Higgins, J.; Jannink, G.; Ober, R.; Picot, C. Dimensions of a flexible polymer chain in the bulk and in solution. *Nature Physical Science*, **1973**, *245*, 13.

[11] Flory, P. Principles of Polymer Chemistry, *Cornell University Press*, **1953**.

[12] Moreno, A. J.; Lo Verso, F.; Arbe, A.; Pomposo, J. A.; Colmenero J. Concentrated solutions of single-chain nanoparticles: a simple model for intrinsically disordered proteins under crowding conditions. *The Journal of Physical Chemistry Letters*, **2016**, *7*, 838-844.

[13] González-Burgos, M.; Arbe, A.; Moreno, A. J.; Pomposo, J. A.; Radulescu, A.; Colmenero, J. Crowding the environment of single-chain nanoparticles: a combined study by SANS and simulations. *Macromolecules*, **2018**, *51*, 1573-1585.

[14] Arbe, A.; Pomposo, J. A.; Asenjo-Sanz, I.; Bhowmik, D.; Ivanova, O.; Kohlbrecher, J.; Colmenero, J. Single-chain dynamic structure factor of linear polymers in all-polymer nanocomposite. *Macromolecules*, **2016**, *49*, 2354-2364.

[15] D. Bhowmik, J. A. Pomposo, F. Juranyi, V. García Sakai, M. Zamponi, A. Arbe, J. Colmenero, Investigation of a nanocomposite of 75 wt % poly(methylmethacrylate) nanoparticles with 25 wt % poly(ethyleneoxide) linear chains: a quasielastic neutron scattering, calorimetric and WAXS study. *Macromolecules* **2014**, *47*, 3005.

[16] Rubio-Cervilla, J.; Barroso-Bujans, F.; Pomposo, J. A. Merging of zwitterionic ROP and photoactivated thiol-yne coupling for the synthesis of polyether single-chain nanoparticles. *Macromolecules*, **2016**, *49*, 90-97.

[17] Pomposo, J. A. Single-chain polymer nanoparticles: synthesis, characterization, simulations and applications. *Wiley*, **2017**.

[18] De La Cuesta, J.; Pomposo, J. A. Photoactivation of Aggregation-Induced Emission Molecules for Fast and Efficient Synthesis of Highly Fluorescent Single-Chain Nanoparticles. *Macromolecules*, **2018**, *3*, 15193-15199.

[19] Wiberg, K. B. The deuterium isotope effect. *Chemical reviews*, **1955**, *55*, 713-743.

[20] Richter, D.; Monkenbusch, M.; Arbe, A.; Colmenero, J. Neutron spin echo in polymer systems, *Springer*, **2005**.

[21] Colmenero, J.; Alegría, A.; Arbe, A.; Frick, B. Correlation between non-Debye behavior and Q behavior of the α-relaxation in glass-forming polymeric systems. *Physical Review Letters*, **1992**, *69*, 478.

[22] Arbe, A.; Colmenero, J.; Alvarez, A.; Monkenbusch, M.: Richter, D.; Farago, B.; Frick, B. Non-gaussian nature of the α-relaxation of glass forming polystyrene. *Physical Review Letters*, **2002**, *89*, 245701.

[23] Arbe, A.; Colmenero, J.; Alvarez, A.; Monkenbusch, M.: Richter, D.; Farago, B.; Frick, B. Experimental evidence by neutron scattering of a crossover from Gaussian to non-Gaussian behavior in the α-relaxation of polyisoprene. *Physical Review E*, **2003**, *67*, 051802.

[24] Frick, B.; Richter, D.; Ritter, C. Structural changes near the glass-transition neutron diffraction on a simple polymer. Europhysics Letters, 1989, 9, 557.

[25] Gennes, P. D. Liquid dynamics and inelastic scattering of neutrons. Physica, 1959, 25, 825.

[26] Colmenero, J.; Alvarez, A.; Khairy, Y.; Arbe, A. Modelling the collective relaxation time of glass-forming polymers at intermediate length scales: application to polyisobutylene. *The Journal of Chemical Physics*, **2013**, *139*, 044906.

[27] Rubinstein, M.; Colby, R. H. Polymer physics, *Oxford*, **2003**.

[28] Moreno, A. J.; Lo Verso, F.; Sanchez-Sanchez, A.; Arbe, A.; Colmenero, J.; Pomposo, J. A. Advantages of Orthogonal Folding of Single Polymer Chains to Soft Nanoparticles. *Macromolecules*, **2013**, *46*, 9748-9759.

[29] Pomposo, J. A.; Moreno, A. J.; Arbe, A.; Colmenero, J.; Local domain size in single-chain polymer nanoparticles. *ACS Omega*, **2018**, *3*, 8648-8654.

[30] Vlassopoulos, D. Macromolecular topology and rheology: beyond the tube model. *Rheologica Acta*, **2016**, *55*, 613-632.

[31] deGennes, P. G.; Badoz, J. Fragile objects, *Springer*, **1996**.

CHAPTER 7

Final conclusions and remarks

7.1. Conclusions

Single-chain nanoparticles synthesized by applying single-chain technology to individual polymer chains are promising elements in nanotechnology and materials science. Their potential applications for emerging fields such as nanomedicine, nanocatalysis or nanoelectronics make developing new synthetic routes and unravelling their internal structure and dynamics appealing challenges to any researcher interested in polymers and soft matter. With these ideas in mind, we performed an exhaustive work by combining state-of-the art polymer chemistry and advanced characterization techniques, aiming to open up new synthetic ways towards SCNPs and to shed some light on their intriguing physical properties.

In the first work, we targeted polyether SCNPs starting from cyclic monomers (tetrahydrofuran, glycidyl phenyl ether and glycidyl propargyl ether). They were finally obtained by a combination of zwitterionic ring-opening polymerization (ZROP) with $B(C_6F_5)_3$ as initiator and photoactivated thiol-yne coupling. Interestingly, although we attempted SCNP synthesis starting from poly(THF−GPgE−GPE) terpolymers and poly(THF−GPgE) copolymers, polyether SCNPs were only obtained from the terpolymer precursor. We attributed this to differences in the monomer sequence distribution, which were elucidated by kinetic experiments *via* real−time ^{13}C NMR spectroscopy. The resulting SCNPs were characterized by SEC with triple detection, FTIR spectroscopy, ^{1}H NMR spectroscopy, TEM, and DSC.

Secondly, we present a collaborative work with Prof. Christopher Barner-Kowollik and Dr. Hendrik Frisch carried out at Queensland's University of Technology. Here, we aimed for the synthesis of single-ring nanoparticles (mimicking natural cyclotides)

obtained from cyclic precursors. SRNPs were obtained by a stepwise folding-activation-collapse process. The initial ring closing reaction was carried out by means of a photoactivated hetero Diels-Alder reaction starting from a poly(styrene-co-chloromethylstyrene) precursor endowed with a difunctional photoreactive chain transfer agent. A subsequent azidation reaction made the cyclic polymer reactive towards the final collapse step, which was achived by CuAAC reaction in the presence of an external dialkyne cross-linker. SRNPs showed a significantly higher shrinking factor, $\langle G \rangle = 0.61$, than that of conventional SCNPs $\langle G \rangle = 0.87$, which were synthesized by skipping the initial ring-closing reaction.

In the next work, we delved into the size reduction caused by reversible SCNP formation. For that purpose, we collected extensive literature data (72 SCNPs and 22 reversible interactions) and proposed a simple expression providing the expected size reduction following a Flory-like argument. The agreement between predicted and experimental data is excellent, hence allowing a valuable *a priori* predictive method. Comparison between covalent-bonded SCNPs and reversible SCNPs revealed a lower level of compaction for the latter ones.

Finally, we performed an in-depth analysis of the physical properties of SCNP melts. Prior to that, we had to design an efficient synthetic route to obtain completely-deuterated low-Tg SCNPs, as having deuterated samples is of outmost importance for performing neutron scattering experiments. Polyether-based deuterated single-chain nanoparticles were obtained in gram-scale by a combination of a simple bulk ring-opening copolymerization process, an azidation functionalization reaction and an UV-induced azide decomposition reaction that lead to intra-chain crosslinking.

A comparison between SCNPs and linear precursors was made by employing a set of advanced experimental techniques, aiming for understanding the impact of internal cross-linking on the physical properties. Neutron scattering measurements revealed that the structural relaxation is barely affected upon SCNP formation. A significant slow down of the dynamics is observed, however, at larger length scales, associated to emerging structural heterogeneities with a characteristic length of about 1 nm. Rheological measurements revealed a striking disappearance of the rubbery plateau. Dielectric spectroscopy measurements revealed an enhanced intensity in the frequency region below the α-relaxation loss peak. We attributed these results to the internal structure imprinted by intramolecular cross-linking, which consists of intrachain loops preventing the formation of entanglements among macromolecules, and consequently accelerating the complete relaxation of the chains which leads to the viscous flow

7.2. Publications

This thesis has contributed to the following publications:

- Rubio-Cervilla, J.; Barroso-Bujans, F.; Pomposo, J. A. Merging of zwitterionic ROP and photoactivated thiol-yne coupling for the synthesis of polyether single-chain nanoparticles. *Macromolecules*, **2016**, *49*, 90.

- Pomposo, J. A.; Rubio-Cervilla, J.; Moreno, A. J.; Lo Verso, F.; Bacova, P.; Arbe, A.; Colmenero, J. Folding single chains to single chain nanoparticles via reversible interactions: what size reduction can one expect? *Macromolecules*, **2017**, *50*, 1732.

- Rubio-Cervilla, J.; González, E.; Pomposo, J. A. Advances in single-chain nanoparticles for catalysis applications. *Nanomaterials*, **2017**, *7*, 341.

- Rubio-Cervilla, J.; Frisch, H.; Barner-Kowollik, C.; Pomposo, J. A. Synthesis of single-ring nanoparticles mimicking natural cyclotides by a stepwise folding-activation-collapse process. *Macromolecular Rapid Communications*, **2018**.

- Rubio-Cervilla, J.; Malo de Molina, P.; Robles-Hernandez, B.; Arbe, A.; Moreno, A. J.; Alegria, A.; Colmenero, J.; Pomposo, J. A. Synthesis of completely-deuterated single-chain nanoparticles enabled by intramolecular azide photodecomposition. *Macromolecular Rapid Communications*, Accepted.

- Arbe, A.; Rubio-Cervilla, J.; Alegria, A.; Moreno, A. J.; Pomposo, J. A.; Robles, B.; Malo de Molina, P.; Fouquet, P.; Juranyi, F.; Khaneft, M.; Colmenero, J.; Melts of single-chain polymeric nano-particles: exploring the impact of intra-molecular cross-linking by neutron scattering, dielectric spectroscopy and rheology. *Physical Review Letters*, Submitted.

Resumen

Esta tesis presenta un trabajo exhaustivo en torno a las nanopartículas poliméricas unimoleculares (SCNPs, por sus siglas en inglés). La combinación de técnicas de síntesis de polímeros de vanguardia y técnicas de caracterización avanzadas nos ha permitido:

1. Establecer nuevas rutas sintéticas para obtener SCNPs.
2. Sintetizar SCNPs con nuevas topologías.
3. Estudiar con profundidad las propiedades físicas de las SCNPs.

Los Capítulos 1 y 2 introducen este emergente campo y proporcionan una revisión de los conceptos fundamentales, los métodos de síntesis actuales, las aplicaciones potenciales y algunas de las técnicas de caracterización más utilizadas. Los tipos de instrumentos y las configuraciones utilizadas en el presente trabajo se recogen en el Capítulo 2.

El Capítulo 3 presenta una novedosa fusión de la polimerización por apertura de anillo zwitteriónica y la reacción de acoplamiento tiol-ino fotoactivada, que supone una interesante nueva ruta de obtención de SCNPs. Las SCNPs se obtuvieron a partir del terpolímero poly(THF-GPgE-GPE) con distintas proporciones de monómeros, y presentaron un mayor grado de compactación en el polímero con más unidades entrecruzantes.

Para comprender mejor los procesos de polimerización y de formación de nanopartículas se emplearon técnicas avanzadas de caracterización que incluyen la cromatografía por permeación de gel con triple detección, resonancia magnética nuclear

de protón y carbono, espectroscopía infrarroja, microscopía electrónica y calorimetría diferencial de barrido.

El trabajo detallado en el Capítulo 4 tiene como objetivo la síntesis de SCNPs con una topología nueva: las nanopartículas poliméricas unimoleculares cíclicas, formadas a partir de anillos poliméricos. Esta arquitectura es reminiscente de los ciclótidos: péptidos cíclicos estabilizados por puentes disulfuro intramoleculares.

Las nanopartículas cíclicas son finalmente obtenidas mediante la combinación de reacciones de polimerización controlada, reacciones hetero Diels-Alder fotoactivadas y química "click" catalizada por cobre. Las nanopartículas resultantes son caracterizadas detalladamente mediante técnicas de cromatografía de exclusión por tamaño, resonancia magnética nuclear, espectroscopía de infrarrojo y espectroscopía UV-Visible.

El Capítulo 5 incluye un estudio cuantitativo de la compactación que tiene lugar tras la formación de SCNPs reversibles.

Mediante un argumento de tipo Flory, proponemos una expresión que permite una estimación *a priori* de la reducción de tamaño que se da tras compactar cadenas unimoleculares. Se incluye también una comparación de los resultados obtenidos con dicha expresión con una extensa recopilación de datos bibliográficos (72 SCNPs, 22 tipos de interacciones reversibles).

Finalmente, el Capítulo 6 presenta un método para obtener SCNPs totalmente deuteradas partiendo de monómeros e iniciadores disponibles comercialmente.

La ruta sintética incluye una sencilla polimerización de apertura de anillo en "bulk", una reacción de azidación para funcionalizar el polímero y una reacción de descomposición

del grupo azida asistida mediante luz ultravioleta que promueve las reacciones de entrecruzamiento intramoleculares necesarias para la obtención de SCNPs.

También se realiza un estudio exhaustivo de las propiedades estructurales y dinámicas de fundidos de estas nanopartículas, combinando técnicas de caracterización tales como dispersión de neutrones elástica y cuasielástica, espectroscopía dieléctrica, medidas de reología y calorimetrías.

El estudio muestra, a nivel microscópico, una ralentización de las dinámicas colectivas asociada a heterogeneidades estructurales con una distancia característica de alrededor de 1 nm. A nivel macroscópico, se observa na desaparición prácticamente completa del "techo elástico", que contrasta con el fenómeno opuesto observado en la vulcanización, en el que se genera una estructura de tipo sólido permanente.

Acknowledgements

En primer lugar, me gustaría agradecer la confianza y el apoyo que el Prof. José A. Pomposo ha depositado en mí desde el momento en que llegué a este grupo. Su profesionalidad, optimismo, tranquilidad y excelente trato personal han hecho este trabajo mucho más fácil y llevadero. Muchas gracias por todo, Josetxo.

También quiero agradecer la labor del resto de Profesores del grupo, a quienes pertenece buena parte del mérito de esta tesis. Ha sido un privilegio trabajar con tantos grandes profesionales.

Thank you Prof. Christopher Barner-Kowollik for giving me the chance to work with the Macroarc group in Brisbane. Special thanks to Dr. Eva Blasco and Dr. Hendrik Frisch for helping me so much and for guiding me through a wonderful country.

Por supuesto, muchísimas gracias a toda la gente del grupo "Polymers and Soft Matter". Gracias Thomas, parece que fue ayer cuando llegamos a Donosti y no podías juntar dos palabras en español… Al grupo del máster, cuando todo era nuevo para nosotros… Gracias Isa, por tu paciencia y por hacer que todo funcione, no sé qué sería de los laboratorios sin ti… Gracias a los que seguís ahí (Julen, Amaia, Bea, Paula, los Danis, Guido, Jordan, Xavi…) y los que no (Izas, Natalia, Marina, Alex, Lucía, Gerardo, Edurne…). Sé que me dejo a muchos. Gracias por los cafés, comidas, cenas, risas…

Gracias a la cuadrilla y a mi familia por permitirme llegar hasta aquí. Gracias Nerea, esta tesis va por ti.

Y por último, y más importante, gracias Patri, por estar a mi lado y por hacerme mejor persona. Nothing to add.